University of Alberta

HYBRID MAGNETOHYDRODYNAMIC-KINETIC MODELING OF A GEOMAGNETIC FIELD
LINE RESONANCE

by

Peter Damiano ©

A thesis submitted to the Faculty of Graduate Studies and Research in partial fulfillment
of the requirements for the degree of **Doctor of Philosophy.**

Department of Physics

Edmonton, Alberta
Fall 2002

0-612-81175-1

Canada

University of Alberta

Library Release Form

Name of Author: Peter Damiano

Title of Thesis: Hybrid Magnetohydrodynamic-Kinetic Modeling of a Geomagnetic Field Line Resonance

Degree: Doctor of Philosophy

Year this Degree Granted: 2002

Permission is hereby granted to the University of Alberta Library to reproduce single copies of this thesis and to lend or sell such copies for private, scholarly or scientific research purposes only.

The author reserves all other publication and other rights in association with the copyright in the thesis, and except as hereinbefore provided, neither the thesis nor any substantial portion thereof may be printed or otherwise reproduced in any material form whatever without the author's prior written permission.

Peter Damiano
University of Alberta
Edmonton, AB
Canada, T6G 2J1

Date: Sept. 30/2002

University of Alberta

Faculty of Graduate Studies and Research

The undersigned certify that they have read, and recommend to the Faculty of Graduate Studies and Research for acceptance, a thesis entitled **Hybrid Magnetohydrodynamic-Kinetic Modeling of a Geomagnetic Field Line Resonance** submitted by Peter Damiano in partial fulfillment of the requirements for the degree of **Doctor of Philosophy**.

Dr. R.D. Sydora (Supervisor)

Dr. J.C. Samson (Supervisor)

Dr. F. Marsiglio

Dr. W. Rozmus

Dr. C. Capjack

Dr. R. Lysak

Date: Sept. 6, 2002

for
Nonna
(1913-2000)
Thanks for everything.

Abstract

Geomagnetic Field Line Resonances (FLRs), which are standing Shear Alfvén wave (SAW) structures, have been linked to the formation of auroral arcs, but the exact mechanism for the acceleration of electrons to the necessary keV velocities is not well understood. Magnetohydrodynamic (MHD) simulations have failed to reproduce the observed parallel electric fields needed to accelerate electrons and so attention has focused on including kinetic effects within the standard MHD formalism. In this thesis, we present a hybrid MHD-kinetic model for standing SAWs to help study the potential for wave-particle interactions involving electrons to lead to enhanced parallel electric fields. The model incorporates the cold plasma MHD equations and kinetic electrons. The guiding center equations are used for the electron motion and the system is closed via an expression for the parallel electric field. This expression incorporates electron inertial effects along with the current and pressure moments of the electron distribution function and a mechanism to enforce quasineutrality. The model has been developed in both a box and dipolar geometry. The latter case incorporates the natural topology of the FLR system and allows for the inclusion of magnetic mirror trapping effects within the model.

In the box model, we show that the hybrid model is consistent with cold plasma MHD results for cold electron distributions and Landau damping effects are evident when the average electron thermal velocity is on the order of the local Alfvén speed. The damping rate is shown to be in good agreement with analytical results illustrating the validity of the approach.

In the dipolar case, we validate the model by illustrating the consistency of the approach with MHD for cold electron temperatures as well as the divergence in the thermal plasma limit. Mirror force effects are shown to be negligible for ionospheres above 3 R_E altitude which is generally consistent with other approaches. It is found that the pressure and magnetic moment effects increase with curvature and temperature. Therefore, it is expected that including lower altitude ionospheres, these effects will further increase the parallel electric field strength.

Acknowledgements

First, I would like to thank my supervisors, Dr. Rick Sydora and Dr. John Samson, for their support and encouragement during my tenure in the Ph.D. program. Dr. Samson gave me the original idea for this challenging project and I am grateful for the many discussions and instruction that sharpened my insight into the physics of Field Line Resonances and space plasmas in general. Dr Sydora gave me the background in kinetic simulations of plasmas, wave-particle interactions and computational physics without which this project would not have been possible. I am grateful for his knowledge and patience during the many lengthy discussions on the physics and detailed numerics of this thesis. It has been an interesting ride and I walk away with a wealth of knowledge and experience.

I am also grateful to my other committee members, Dr. Clarence Capjack, Dr. Frank Marsiglio, Dr Wojciech Rozmus and my external examiner Dr Robert Lysak for careful examination of the thesis and many useful comments. Special thanks also goes to Lynn Chandler, the graduate secretary, for all her help through the years. Her assistance has been invaluable.

I extend my thanks to Dr Robert Rankin for many useful discussions on the MHD modeling of Field Line Resonances and to Dr Vladimir Tikhonchuk for much analytical advice (especially with regards the derivation in Appendix A) and discussions which greatly aided my understanding of the underlying physics.

I am grateful to my fellow graduate students and post doctoral fellows in the Space Physics lab for friendship and many useful discussions over the years. Many thanks go to Sarah Derr, Peter Dobias, Frances Frenrich, Erena Friedrich, Barry Harrold, Konstantin Kabin, Ian Mann, Jonathan Rae, James Wanliss, Igor Voronkov and Clare Watt. I would like to give special thanks to Peter Dobias for help relating to the dipolar metrics and other things analytical; to Erena Friedrich, for many discussions, amusing and otherwise over the cubicle divider and for dragging me into a planetarium presentation that turned into a lot of fun; to Barry Harold, who left this world too soon, for much help at the start and to Ian Mann for many enlightening discussions on FLRs and cold plasma MHD theory.

Contents

List of Figures

List of Tables

List of Symbols

α - pitch angle

α_o - equatorial pitch angle

$\vec{B}$ - total magnetic field

$\vec{B}_o$ - ambient magnetic field

$\vec{b}$ - perturbed magnetic field

B_N - magnetic field normalization constant

c - speed of light

e - electron charge magnitude

$\vec{E}$ - electric field

ϵ_o - permittivity of free space

$\vec{\xi}$ - plasma displacement

$\vec{E}_c$ - correction field to enforce quasineutrality

E_N - electric field normalization constant

$f = f_o + f_1$ - electron distribution function

f_o - equilibrium distribution function

f_1 - perturbed distribution function

h_i - scale factor or Lamé coefficient where subscript denotes direction

$\vec{j}$ - current density

k - wavenumber

k_B - Boltzman constant

K_μ - normalization constant for magnetic moment term in the equation for the dipolar parallel electric field

K_p - normalization constant for the pressure term in the equation for the dipolar parallel electric field

$\vec{j}_p$ - polarization current density

λ - angle subtended from the equator

λ_m - mirroring angle of an electron subtended from the equator

λ_e - electron inertial length

λ_D - Debye length

L - normalization constant for length

μ_o - permeability of free space

μ_M - electron magnetic moment

m_e - electron mass

m_p - proton mass

n_e - electron number density

n - single fluid number density

ω_{ge} - electron cyclotron frequency

p - pressure

q - electric charge

ρ - fluid mass density

ρ_N - fluid density normalization constant

$\vec{r}_g$ - gyroradius

R_E - earth radius

σ - electric conductivity

$S(\vec{x}, \vec{x_i})$ - particle shape function

T_b - electron bounce time in a dipolar magnetic field

T_E - average energy of electron distribution function

θ - angle subtended from the northern pole axis

$\vec{u}$ - fluid velocity

$\vec{v}$ - electron velocity

$\vec{v}_E$ - $\vec{E} \times \vec{B}$ drift velocity

v_{th} - thermal velocity of electron distribution function

v_p - polarization drift velocity

x_1 - curvilinear coordinate along ambient magnetic field (also denoted by μ)

x_2 - curvilinear coordinate perpendicular (in the radial direction) to the ambient magnetic field (also denoted by ν)

x_3 - curvilinear coordinate in azimuthal direction (also denoted by ϕ)

x_r - resonance position in the box model

x_t - turning point of the fast mode in the box model

V_A - Alfvén speed

W_C - curvature drift

$W_{\nabla B}$ - gradient drift

Z - plasma dispersion function

Chapter 1

Introduction

1.1   Preamble

Space plasma physics is generally defined as the study of plasmas in the earth's near space environment. Such a simple statement belies a complex series of processes which commence with the outflow of plasma from the sun, called the solar wind, and end with the deposition of energy in the earth's ionosphere and upper atmosphere which manifests itself in the visible aurora. It is a prime example of the transfer of energy to smaller and smaller scales. The initial transfer of energy between the solar wind and the earth's magnetosphere can be accomplished through several mechanisms, one being the excitation of Alfvén waves by the interaction of the solar wind with the magnetospheric boundaries. These waves can propagate toward the Earth and have been observed to form Standing Shear Alfvén waves (SAW) structures along the earth's dipolar magnetic field called Field Line Resonances (FLR). Satellite observations have linked these structures with the formation of the small scale discrete auroral arcs. Simulations of the FLR system using the magnetohydrodynamic equations (MHD) have reproduced the observed scale structures, but have consistently failed to reproduce the electric field magnitudes needed to accelerate electrons to sufficient velocity to allow them to reach the earth's atmosphere. This illustrates that the wave-particle interactions, which are not included in the MHD description, may be vital in understanding the FLR system.

In this work, we concentrate on the development of a hybrid MHD-kinetic model which combines the use of the cold plasma MHD equations with a kinetic description for the electrons to study how wave-particle interactions can effect the evolution of a SAW system as compared the to MHD description alone. We will conduct this study in cartesian and dipolar coordinate systems: the first to facilitate code development and testing and the latter to more accurately model the physics of a FLR system.

1

1.2 Basic structure of the magnetosphere

As already stated, the ultimate driving force of the Earth's magnetospheric structure (as seen in Fig. (1.1)) is the solar wind. Its flow is both supersonic and super Alfvénic and it generates a standing collisionless shock front called the Bow Shock where the earth's magnetic field becomes an obstacle to the supersonic flow of the solar wind. It slows the solar wind to subsonic speeds. It is analogous to shocks in a regular fluid except that this entire phenomenon is collisionless. The nose of the bow shock (the most sunward portion) is typically 12-15 R_E (1 R_E=6371 km). Since the flow speeds outside of the Bow Shock are supersonic, any waves incident on the Bow Shock from inside the magnetosphere will be reflected back inwards. After the bow shock, the subsonic solar wind propagates on until another boundary (called the magnetopause) is reached, defined by the balance of forces between the solar wind pressure and the magnetic pressure exerted by the earth's magnetic field. The position of the magnetopause is described mathematically by the following (Parks, 1991),

$$2mnU_{SW}^2 cos^2\phi = \frac{B_p^2}{2\mu_o} \tag{1.1}$$

where the right hand side is the magnetic energy density, U_{SW} is the solar wind velocity, m is the mass of solar wind particles and n is the particle number density. The angle ϕ is the angle between the solar wind velocity vector and the normal to the magnetopause boundary. The region of laminar flow in between the magnetopause and bow shock is called the magnetosheath. This is contrasted by a turbulent layer on the inner side of the magnetopause boundary called the Low Level Boundary Layer (LLBL). In this region, Kelvin-Helmoltz instabilities as well as other factors can produce fluctuations that lead to wave propagation into surrounding regions of the magnetosphere. The lobe is a region of reduced plasma density adjacent to the higher density plasma sheet which contains particles of both solar wind and ionospheric origin. The plasmapause is a sharp boundary separating the colder plasma regions of the near earth environment (plasmasphere), where the plasma dynamics are controlled by the earth's magnetic field, from the hotter surrounding plasma. The boundary is typically found at an altitude of 3-5 R_E.

FLRs typically form along the dipolar magnetic field lines between about 8 and 10 R_E in the equatorial plane. The average plasma densities in this region are on the order 0.1 -1 cm^{-3} with average particle thermal energies of 10s of eV for electrons. The typical magnetic field strength is on the order of a few nT. The tenuous nature of this plasma means that it is essentially collisionless. However, the presence of the magnetic field (even one this tenuous) means that particles can interact with each other via the electromagnetic forces between them.

There are several current systems in the magnetosphere and any current that moves along the magnetic field lines is called a field aligned current (FAC). Typically this current

2
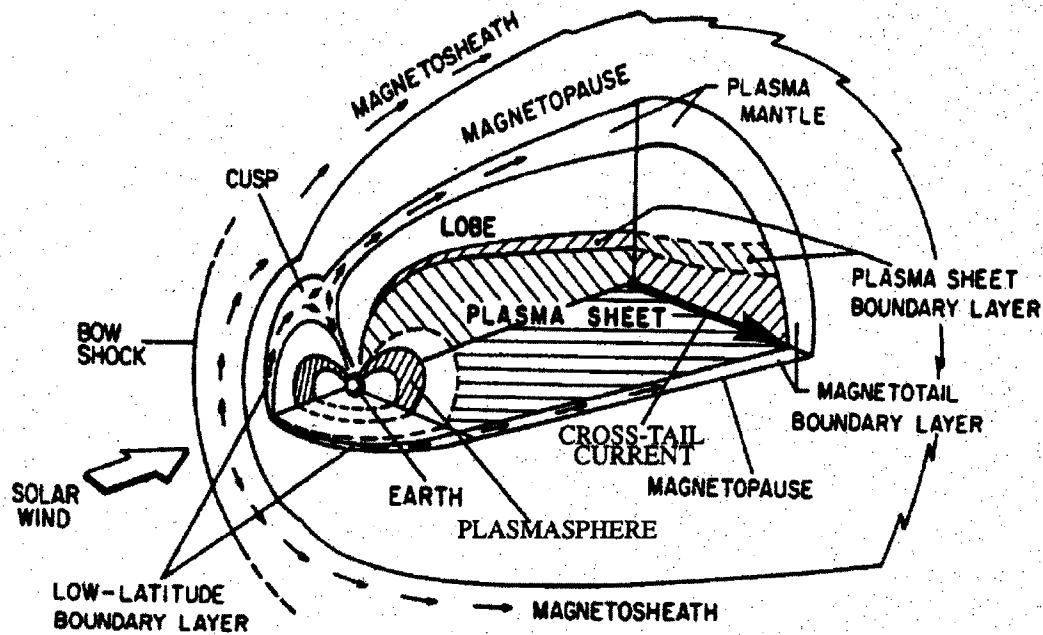
Figure 1.1: Three dimensional view of the Earth's magnetosphere from Eastman et al. (1985).

is carried by electrons as they can move very rapidly along the field lines, while much of the perpendicular current is carried by ions since they are massive enough to cross field lines. In field line resonances, the parallel electron current is the response of the plasma to perpendicular ion polarization currents, in order to maintain the quasineutrality of the plasma.

1.3 The Ionosphere

The ionosphere is the ultimate dumping ground for all the magnetospheric energy and is a very different plasma region than the magnetosphere. It commences about 60 km in altitude from the surface of the earth and it owes its ionized state to incoming solar radiation and the precipitation of high energy particles along the earth's magnetic field lines. A slow recombination rate maintains the plasma state. There are three distinct regions in the ionosphere defined by their relative plasma characteristics and density variations which go from approximately 10^3 cm^{-3} at the lower edge to 10^6 cm^{-3} at the upper edge (about 300 km in altitude). These high densities make the ionospheric plasma collisional. Some field aligned current systems from the magnetosphere are closed via perpendicular currents in the ionosphere and the interaction of high energy electrons moving along the field lines with the ionospheric plasma lead to the visible aurora. High energy protons also interact with

3

the ionospheric plasma to produce the proton aurora, but these are not generally visible to the naked eye.

1.4 Plasmas

Plasmas are differentiated from ionized gases by two fundamental concepts: quasineutrality and the fact that a plasma can exhibit collective behaviour. The idea of collective behavior arises from the fact that if a sufficiently large number of particles are ionized in the plasma, the attractive and repulsive forces between opposite and similarly charged particles respectively can give rise to regions of positive and negative charge. These relative regions of charge separation give rise to electric fields and consequently current and the plasma can be seen to have a "collective behavior" on the larger scale.

This idea also relates to the ability of a plasma to shield out external potentials applied to it. If an external potential difference is applied across a region of the plasma, the electrons will move to the positive pole and the ions to the negative pole. In a cold plasma, the shielding will be perfect and no electric field will result. However if the plasma has a finite temperature, some of the electrons at the edge of the shielding cloud will escape from the potential. Short range electric fields can then exist beyond this point. This "edge" is where the average kinetic energy of the electrons is approximately equal to the electrostatic potential and the radius of the shielding volume is given by

$$\lambda_D = (\frac{\epsilon_o k_B T}{n e^2})^{1/2} \tag{1.2}$$

where λ_D is called the Debye Length and the shielding phenomena is known as Debye Shielding. Therefore, for any charge concentration or external potentials in the plasma, they will be shielded out for large scale lengths L, where $L \gg \lambda_D$. This implies that most of the plasma is free of electric fields and potentials. Therefore, if we define electric and ion number densities of n_e and n_i, then the plasma can be said to be quasinuetral in that $n_i \approx n_e \approx n$ where, n is the plasma density. The term "quasi" is introduced, since the plasma is predominantly neutral on the larger scale, but smaller scale inconsistencies in densities can still introduce electromagnetic forces. The condition $L \gg \lambda_D$ and quasinuetrality are the first two conditions to define a plasma. The third comes from the fact that the idea of Debye Shielding only has meaning if there are enough particles in the charge cloud to be statistically valid. Therefore, defining the number of particles in a Debye Sphere as

$$N_D = \frac{4}{3}\pi\lambda_D^3 n \tag{1.3}$$

it is necessary that $N_D \gg 1$.

4

1.5 Kinetic and Fluid descriptions of plasmas

One of the most basic equations to describe a collisionless magnetized plasma system is the Vlasov equation, derived by the Russian physicist A.A. Vlasov in 1945

$$\frac{\partial f_s}{\partial t} + \vec{v} \cdot \frac{\partial f_s}{\partial \vec{r}} + \frac{q_s}{m_s}(\vec{E} + \vec{v} \times \vec{B}) \cdot \frac{\partial f_s}{\partial \vec{v}} = 0 \tag{1.4}$$

where f_s is the particle velocity distribution function of species s, and $\vec{r}$ and $\vec{v}$ are the position and velocity vectors respectively. Integrating the moments of the velocity distribution function over velocity space, yields the bulk plasma parameters. For example, the 0th moment yields the particle number density for species s, n_s

$$n_s(\vec{r}, t) = \int f_s(\vec{r}, \vec{v}, t) d^3 v \tag{1.5}$$

while the first moment, yields the average velocity of the plasma species, $\vec{u}_s$

$$\vec{u}_s = \frac{1}{n_s(\vec{r}, t)} \int \vec{v} f_s(\vec{r}, \vec{v}, t) d^3 v. \tag{1.6}$$

Now, it is possible to work with the Vlasov equation directly, but also, it can be used as a starting point to derive a fluid description for the plasma. First of all, directly integrating (1.4), over velocity space, yields (see Parks, (1991) for details)

$$\frac{\partial n_s}{\partial t} + \nabla \cdot (n\vec{u}_s) = 0 \tag{1.7}$$

This is an equation of continuity since it states that the number of particles must be conserved.

Now, multiplying (1.4) by $\vec{v}$ and again integrating over velocity space yields the momentum equation for species s

$$m_s n_s \frac{d\vec{u}_s}{dt} = q_s n_s(\vec{E} + \vec{u} \times \vec{B}) - \nabla p_s \tag{1.8}$$

where it has also been assumed that the plasma pressure is isotropic. This process can be continued to produce an infinite set of equations, but for the purposes of this work, it is necessary to consider only the first two equations in the hierarchy.

For a plasma in thermal equilibrium, the distribution function is a Maxwellian, given by the expression,

$$f(\vec{r}, \vec{v}) = n(\frac{m}{2\pi kT})^{3/2} exp(\frac{-m(\vec{v} - <\vec{v}>)^2}{2kT}) \tag{1.9}$$

where $<\vec{v}> = \vec{u}_s$ is the average particle velocity.

5

1.6 One Fluid Magnetohydrodynamic Equations

A plasma generally contains electrons and at least one species of ions (most commonly H^+) resulting in the need for at least two sets of fluid equations to describe the dynamics. Unfortunately the solution of the the two-fluid system can be quite involved, but it is possible to reduce this two-fluid set into a single fluid description. Although this system is less complete, it captures much of the physics of the relevant wave motions of interest in magnetospheric physics and so is a convenient starting point for the investigation of some phenomena.

The set of single fluid MHD equations begins with Maxwell's equations which, in MKS units, are given by

$$\nabla \times \vec{B} = \mu_o \vec{j} + \frac{1}{c^2} \frac{\partial \vec{E}}{\partial t} \tag{1.10}$$

$$\nabla \cdot \vec{B} = 0 \tag{1.11}$$

$$\nabla \times \vec{E} = -\frac{\partial \vec{B}}{\partial t} \tag{1.12}$$

$$\nabla \cdot \vec{E} = \frac{\rho^*}{\epsilon_o} \tag{1.13}$$

where $\vec{B}$ is the magnetic field, $\vec{E}$ is the electric field, $\vec{j}$ is the current density, ρ^* is the the electric charge density, μ_o is the electric permeability, ϵ_o is the permitivity of free space and $c = \frac{1}{\sqrt{\mu_o \epsilon_o}}$ is the speed of light in a vacuum. Most processes in the magnetosphere are of a low frequency and non-relativistic nature and the displacement current portion is negligible, so that

$$\nabla \times \vec{B} = \mu_o \vec{j}. \tag{1.14}$$

Next, the fluid equations for the electrons and ions are combined as follows. Multiplying equation (1.7) by the particle mass, m_s, and writing the continuity equations for both electrons and ions

$$\frac{\partial \rho_i}{\partial t} + \nabla \cdot (\rho_i \vec{v}_i) = 0 \tag{1.15}$$

$$\frac{\partial \rho_e}{\partial t} + \nabla \cdot (\rho_e \vec{v}_e) = 0 \tag{1.16}$$

where ρ_i and ρ_e are the ion and electron number densities respectively and v_i and v_e are their respective velocities. Adding these two equations then yields

$$\frac{\partial}{\partial t}(\rho_i + \rho_e) + \nabla \cdot (\rho_i \vec{u}_i + \rho_e \vec{u}_e) = 0. \tag{1.17}$$

For a two component plasma of electrons and ions, the total mass density is

6

$$\rho = \rho_e + \rho_i = n_i m_i + n_e m_e. \tag{1.18}$$

and using the center of mass fluid velocity $\vec{u}$ defined by

$$\vec{u} = \frac{n_i m_i \vec{u}_i + n_e m_e \vec{u}_e}{n_i m_i + n_e m_e}, \tag{1.19}$$

equation (1.17) becomes

$$\frac{d\rho}{dt} + \nabla \cdot (\rho \vec{u}) = 0. \tag{1.20}$$

This is the single fluid continuity equation.

Now, writing the momentum equation for the two species

$$m_i n_i \frac{d\vec{u}_i}{dt} = q_i n_i (\vec{E} + \vec{u}_i \times \vec{B}) - \nabla p_i \tag{1.21}$$

$$m_e n_e \frac{d\vec{u}_e}{dt} = q_e n_e (\vec{E} + \vec{u}_e \times \vec{B}) - \nabla p_e \tag{1.22}$$

adding them together assuming $n_i = n_e = n$, $q_i = -q_e$ and defining total pressure, $p = p_i + p_e$, yields

$$n \frac{d}{dt}(m_i \vec{u}_i + m_e \vec{u}_e) = qn(\vec{u}_i - \vec{u}_e) \times \vec{B} - \nabla p. \tag{1.23}$$

Defining the current density $\vec{j}$

$$\vec{j} = n_i q_i \vec{u}_i + n_e q_e \vec{u}_e = qn(u_i - u_e) \tag{1.24}$$

and using the definition of $\vec{u}$ from equation (1.19), the single fluid momentum equation becomes

$$\rho \frac{d\vec{u}}{dt} = \vec{j} \times \vec{B} - \nabla p. \tag{1.25}$$

In order to close the single fluid MHD system of equations, an equation of state is needed to relate the pressure and density. For an isothermal fluid and an adiabatic fluid respectively, the equation of states are given by

$$\frac{d}{dt}\left(\frac{p}{\rho}\right) = 0 \tag{1.26}$$

and

$$\frac{d}{dt}(p\rho^{-\gamma}) \tag{1.27}$$

where γ is the ratio of the specific heats C_p/C_V. For an isotropic Maxwellian distribution function, $\gamma = \frac{5}{3}$.

7

The final point in deriving the system of single fluid MHD equations is to relate the current density and the electric field via the Ohm's law

$$\vec{J} = \sigma \vec{E}_T \tag{1.28}$$

where $\vec{E}_T$ is the total electric field and σ is the conductivity. Generally, the Ohm's law involves a convolution integral where σ is given by a matrix, but for the moment it is being assumed that long range forces are minimal and the electric field and current are only related by the local conductivity. The idea of nonlocal conductivity will be returned to later in the chapter.

Now, in a plasma there is the ambient electric field $\vec{E}$, but also that induced by the fluid motion across the magnetic field lines $\vec{u} \times \vec{B}$. Therefore, the Ohm's law becomes

$$\vec{J} = \sigma(\vec{E} + \vec{u} \times \vec{B}). \tag{1.29}$$

In the earth's magnetosphere, the plasma is essentially collisionless making the conductivity very high and so it is common as a first approximation to assume $\sigma = \infty$. This is known as the ideal MHD approximation, and the only way to have a finite current in such a case is to have, $E + \vec{u} \times \vec{B} = 0$ and therefore

$$E = -\vec{u} \times \vec{B} \tag{1.30}$$

As a more general formulation, there is the Generalized Ohm's law given by the following (Nicholson, 1983),

$$\vec{E} + \vec{u} \times \vec{B} = \frac{m_i m_e}{e^2 \rho} \frac{\partial \vec{J}}{\partial t} + \frac{m_i}{e\rho} \vec{J} \times \vec{B} + \frac{\vec{J}}{\sigma} - \frac{m_i}{2e\rho} \nabla p \tag{1.31}$$

which can be derived from the momentum equations for ions and electrons (including the collision terms). It is called the Generalized Law in that if all terms on the right hand side can be neglected except the second last one, the equation reduces to the basic Ohm's Law (1.29). Generally, for magnetospheric plasmas, we can ignore the second term on the right (also known as the Hall term), and assuming the ideal MHD approximation, the Generalized Ohm's law becomes

$$\vec{E} + \vec{u} \times \vec{B} = \mu_o \lambda_e^2 \frac{\partial \vec{J}}{\partial t} \tag{1.32}$$

where $\lambda_e^2 = \frac{m_i m_e}{e^2 \rho}$ is the electron inertial length squared and the assumption of a cold plasma has been used as well. Noting $\rho \approx n m_i$, then the electron inertial length can be rewritten as $\lambda_e^2 = \frac{m_e}{\mu_o n e^2}$.

Now, in order to further justify neglecting the displacement current, the following scaling argument (Voronkov, 1998) can be used. Comparing the magnitude of the displacement

8

current term and the $\nabla \times \vec{B}$ term (using the ideal MHD approximation for the electric field) yields,

$$\frac{|\partial \vec{E}/\partial t|}{c^2 |\nabla \times \vec{B}|} \approx \frac{E_n/t_n}{c^2 B_n/L_n} \approx \frac{v_n B_n/t_n}{c^2 B_n/L_n} \approx \frac{v_n^2}{c^2} \tag{1.33}$$

where E_n, B_n and v_n are characteristic values of $\vec{E}$, $\vec{B}$ and $\vec{v}$ respectively. Therefore as long as $v_n \ll c$, the displacement current can be neglected. It should be noted however, that in a dipolar magnetic field $\nabla \times \vec{B}_o = 0$ (where B_o is the ambient magnetic field) and ratio becomes

$$\frac{|\partial \vec{E}/\partial t|}{c^2 |\nabla \times \vec{B}|} \approx \frac{V_A^2}{c^2}$$

(R. Lysak, private communication). In this case, the Alfvén velocity close to the ionospheres can start to become a significant fraction of the speed of light and displacement current effects may need to be considered.

1.6.1   Cold Plasma Approximation

In the limit $T \rightarrow 0$, thermal effects within the plasma can be ignored. This is known as the cold plasma approximation. In this limit the momentum equation becomes

$$\rho \frac{d\vec{u}}{dt} = \vec{j} \times \vec{B} \tag{1.34}$$

and the equation of state is not needed to relate density and pressure. Therefore, the single fluid MHD system of equations can be reduced to the following

$$\nabla \times \vec{B} = \mu_o \vec{j} \tag{1.35}$$

$$\nabla \times \vec{E} = -\frac{\partial \vec{B}}{\partial t} \tag{1.36}$$

$$\frac{d\rho}{dt} + \nabla \cdot (\rho \vec{u}) = 0 \tag{1.37}$$

$$\rho \frac{d\vec{u}}{dt} = \vec{j} \times \vec{B} \tag{1.38}$$

$$\vec{E} + \vec{u} \times \vec{B} = \mu_o \lambda_e^2 \frac{\partial \vec{J}}{\partial t}. \tag{1.39}$$

As a further examination of the meaning of the cold plasma approximation, the $\vec{J} \times \vec{B}$ term in the momentum equation can be rewritten using Ampere's law and a vector identity as

$$\vec{j} \times \vec{B} = \frac{(\nabla \times \vec{B}) \times \vec{B}}{\mu_o} = \frac{\vec{B} \cdot \nabla \vec{B}}{\mu_o} - \frac{\nabla B^2}{2\mu_o} \tag{1.40}$$

9

where the first term is due to magnetic curvature and the second term is due to magnetic pressure. Noting the ratio of thermal pressure to magnetic pressure

$$\beta = \frac{p}{B^2/(2\mu_o)}, \tag{1.41}$$

the cold plasma approximation can be defined as the limit where $\beta \to 0$ and magnetic pressure dominates over thermal pressure. For a low beta plasma, where magnetic curvature is negligible, the only term of importance is magnetic pressure.

1.6.2 Linearization

For this present work we will only be considering linear theory with the assumptions $\vec{B}(\vec{r}, t) = B_o(\vec{r}) + \vec{b}(\vec{r}, t)$, $\rho(\vec{r}, t) = \rho_o(\vec{r}) + \rho_1(\vec{r}, t)$ and $\vec{u} = \frac{d\xi}{dt}$ where ξ is the plasma displacement. With these assumptions, the cold plasma equations are reduced to the following,

$$\nabla \times \vec{B} = \mu_o \vec{j} \tag{1.42}$$

$$\nabla \times \vec{E} = -\frac{\partial \vec{b}}{\partial t} \tag{1.43}$$

$$\frac{d\rho_1}{dt} + \nabla \cdot (\rho_o \vec{u}) = 0 \tag{1.44}$$

$$\rho \frac{d\vec{u}}{dt} = \frac{1}{\mu_o} (\nabla \times \vec{b}) \times \vec{B} \tag{1.45}$$

$$\vec{E} + \vec{u} \times \vec{B} = \mu_o \lambda_e^2 \frac{\partial \vec{J}}{\partial t} \tag{1.46}$$

With the definition of the ambient magnetic field B_o, the terms field aligned direction (or parallel direction) and perpendicular direction are introduced with reference to the directions parallel and perpendicular to B_o.

One consequence of the linearization is that there is no field aligned component for the plasma velocity. This, along with the fact that the inertial term has negligible contribution to the perpendicular components of the electric field, allows the equation for the electric field to be written as two equations, one each for the parallel and perpendicular components, as

$$E_{\parallel} = \mu_o \lambda_e^2 \frac{\partial \vec{J}_{\parallel}}{\partial t} \tag{1.47}$$

$$\vec{E}_{\perp} = -\vec{u}_{\perp} \times \vec{B}_o. \tag{1.48}$$

10

1.7 Alfvén Waves

Although there are many different wave types which can exist in a plasma, only three modes can exist in the MHD limit, the shear Alfvén wave (SAW), the fast magnetoacoustic mode and the slow magnetoacoustic mode. The first of these, the shear Alfvén wave, is a purely transverse wave in which the perturbed part of the magnetic field is perpendicular to the ambient magnetic field and the wave propagates along the ambient magnetic field line (see figure 1.2 (a)). For an ideal homogeneous incompressible plasma ($\sigma = \infty$, $\nabla p = 0$, $\nabla \cdot \vec{u} = 0$) the cold plasma MHD equations can be simplified to

$$\frac{\partial}{\partial t}\vec{B} = \nabla \times (\vec{u} \times \vec{B}) \tag{1.49}$$

$$\rho\frac{\partial \vec{u}}{\partial t} = \frac{1}{\mu_o}(\nabla \times \vec{B}) \times \vec{B}. \tag{1.50}$$

Assuming the linear approximation for the magnetic field perturbation and choosing the ambient magnetic field direction so that $\vec{B}_o = B_o\hat{z}$, it is possible to show that these MHD equations can be reduced to the following wave equations

$$\frac{\partial^2 \vec{b}}{\partial t^2} = V_A^2 \frac{\partial^2 \vec{b}}{\partial z^2} \tag{1.51}$$

$$\frac{\partial^2 \vec{u}}{\partial t^2} = V_A^2 \frac{\partial^2 \vec{u}}{\partial z^2} \tag{1.52}$$

where V_A is the Alfvén speed given by

$$V_A = \pm\frac{B_o}{(\mu_o\rho_m)^{1/2}}. \tag{1.53}$$

Assuming $\vec{v}$ and $\vec{b}$ vary as $\exp(i(\vec{k} \cdot \vec{r} - \omega t))$, it is straightforward to derive the dispersion relation for the shear Alfvén wave

$$\frac{\omega^2}{k_z^2} = V_A^2 cos^2(\theta) \tag{1.54}$$

where θ is the angle between the wave vector, $\vec{k}$, and the ambient magnetic field $\vec{B}_o$. For the case of the linear cold plasma equations, there is no velocity component parallel to the magnetic field and the dispersion relation reduces to

$$\frac{\omega^2}{k_z^2} = V_A^2. \tag{1.55}$$

For the case of a compressible plasma, a more involved derivation (see Parks, 1991), yields the following dispersion relation

$$\frac{\omega^2}{k^2} = \frac{1}{2}(V_A^2 + C_s^2 \pm [(V_A^2 + C_s^2)^2 - 4V_A^2 C_S^2 cos^2(\theta)]^{1/2}) \tag{1.56}$$

11
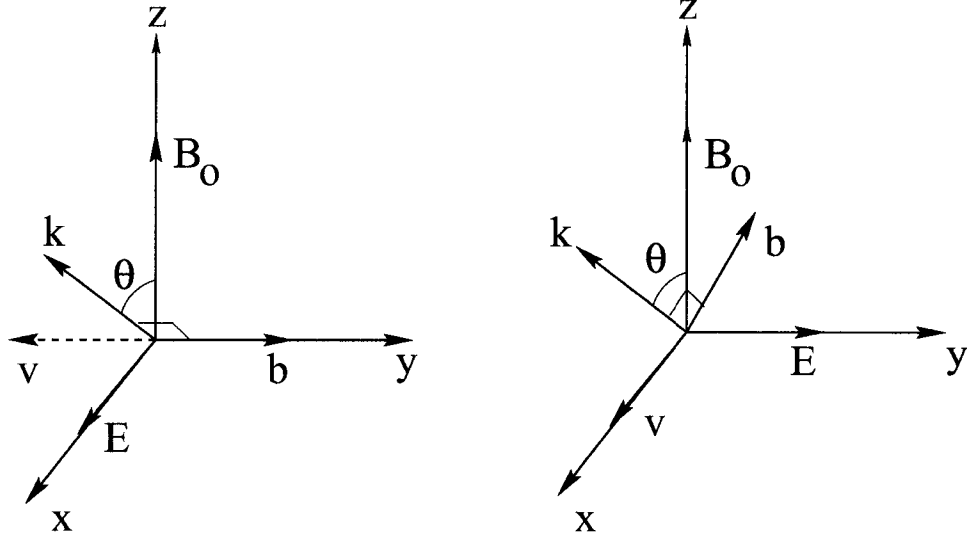
Figure 1.2: a) Schematic of Shear Alfvén wave. b) Fast compressional mode.

where $C_s^2 = \frac{\gamma p_o}{\rho_o}$ is the speed of sound in the plasma. The positive and negative solutions correspond respectively to the fast and slow magnetosonic modes. The latter is known as a slow mode because the phase velocity is slower than either V_A or C_s. Both modes are driven by magnetic tension and thermal pressure forces and have both transverse and compressional components. The difference between the two modes is that in the fast mode, the magnetic field and plasma oscillations are in phase and in the slow mode, they are out of phase. For $\theta = 0$, the slow mode vanishes and the dispersion relation for the fast mode reduces to

$$\frac{\omega^2}{k^2} = V_A^2 + C_s^2. \tag{1.57}$$

In a cold plasma $C_s = 0$ and $\frac{\omega^2}{k^2} = V_A^2$.

The nature of these modes are further illustrated in figure (1.2). In panel (a) the Shear Mode is illustrated with $\vec{v}$ and $\vec{b}$ perpendicular to the ambient magnetic field and $\vec{k}$ is perpendicular to $\vec{v}$ showing that the wave is incompressible. For the case of the compressional mode (b), it is evident that the wave is compressible since $\vec{b}$ has a component along B_o and $\vec{k} \cdot \vec{v} \neq 0$.

In figure (1.3), plots of phase and group velocity for all three wave modes are plotted as a function of θ for the case of $C_S < V_A$ which is usually the case in magnetospheric plasmas. From this it is evident that the maximum velocity for the fast mode propagates perpendicular to the ambient magnetic field while the slow mode and Shear Alfvén wave modes have a maximum velocity parallel to the ambient magnetic field.

1.7.1 Dispersive Alfvén waves

With the inclusion of the Generalized Ohm's Law in the cold plasma limit ($\beta < \frac{m_e}{m_i}$),

12
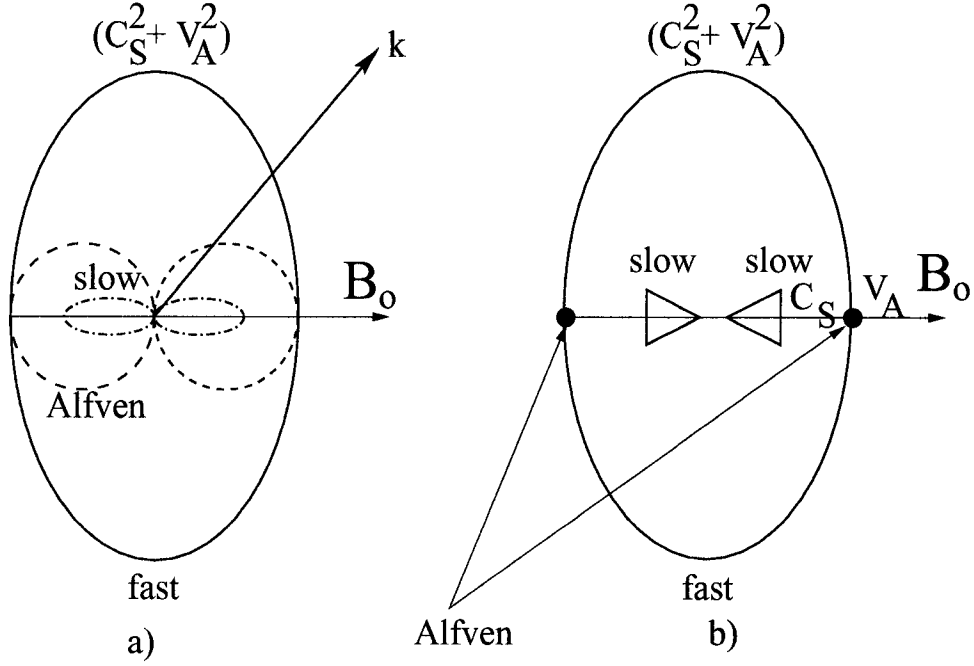
Figure 1.3: a) The phase speed of the fast, slow and Alfvén waves as a function of θ. b) The group velocity as a function of θ

$$\vec{E} + \vec{u} \times \vec{B} = \mu_o \lambda_e^2 \frac{\partial \vec{J}}{\partial t}$$

in the ideal MHD equations, it can be shown that the Shear Alfvén wave dispersion relation will change such that

$$\omega^2 = \frac{k_z^2 V_A^2}{1 + k_\perp^2 \lambda_e^2} \tag{1.58}$$

where λ_e is the electron inertial length as mentioned earlier and $k_\perp$ is the wavenumber perpendicular to the ambient magnetic field.

On the other hand, for the case of a warmer plasma ($\beta > \frac{m_e}{m_i}$), it can be shown (refer to Appendix A) that the dispersion relation becomes,

$$\omega^2 = k_z^2 V_A^2 (1 + \frac{1}{2} k_x^2 \rho_s^2) \tag{1.59}$$

where $\rho_s = \lambda_e v_{th}/V_A$ is the effective ion gyroradius. These two dispersion relations are the dispersion relations for inertial Shear Alfvén wave and and kinetic Alfvén wave respectively. They are dispersive because they lead to a propagation in the perpendicular direction with short perpendicular wavelength. This is evident from the fact that the perpendicular group velocity, $\frac{\partial \omega}{\partial k_\perp}$, is non-zero. The inertial Alfvén wave will propagate into regions of lower density and the kinetic Alfvén wave will propagate into regions of higher density. More detail on these waves will be given later in this chapter with the discussion of FLRs and

13
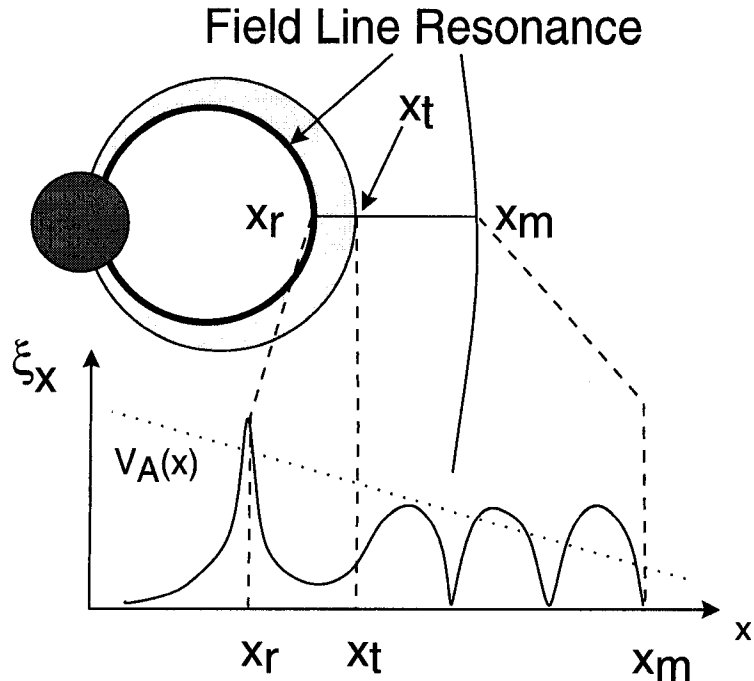
Figure 1.4: Schematic of a Field Line Resonance

in the following Chapters (especially chapters 2 and 4). The existence of these dispersive waves in space plasmas was first noted by Hasegawa (1976).

1.8 Field Line Resonances

Magnetohydrodynamics is a good starting point for the study of FLRs because it incorporates all the necessary wave modes needed to understand the phenomenon. In this section, the basic physics behind the resonance will be discussed along with the linear theory developed by Chen and Hasegawa (1974) and Southwood (1974).

The basic mechanism is as follows (refer to figure (1.4)). Compressional waves are excited in the dayside magnetospheric region by several possible sources including pulses from the solar wind, due to such things as coronal mass ejections, interacting with the magnetopause boundary. As these waves propagate Earthward, they see an increasing Alfvén wave gradient which causes the wave to be reflected at some point known as the turning point, x_t (this reflection is actually a gradual refraction, but for the simple model considered here, it is a good approximation to regard it as a reflection). However, not all the energy of the compressional mode is reflected, part of the energy evanesces past the turning point and when it encounters a dipole magnetic field line with a natural eigenmode equal to the frequency of the incident compressional wave a standing SAW is excited along this field line. It is this excitation of the shear Alfvén wave along the dipole field line that

14
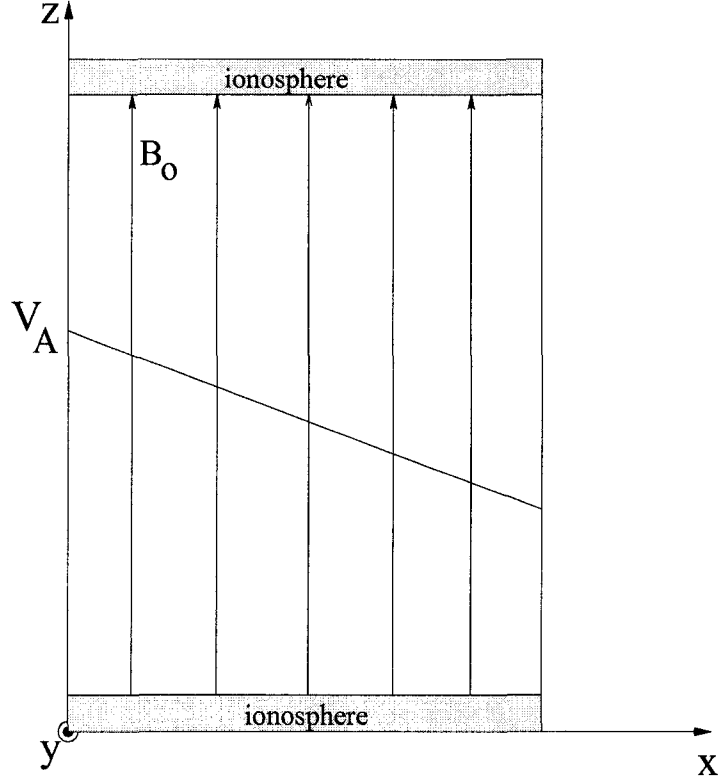
Figure 1.5: Box Model of Magnetosphere

is called an FLR.

For the basic linear theory of an FLR, it is possible to simplify the geometry to that of a box so that the field aligned direction becomes z and the radial direction is x (see Figure (1.5)). The ambient magnetic field is constant and the Alfvén wave gradient is introduced via a radial gradient in the density. Then assuming perturbations of the form

$$e^{i(\omega t - k_y y - k_z z)} \tag{1.60}$$

the following wave equation can be derived from the linearized MHD equations

$$\frac{\partial^2 E_y}{\partial x^2} - \frac{k_y^2}{[(\omega/V_A)^2 - k_z^2]\kappa^2} \frac{\partial}{\partial x} \left(\frac{\omega^2}{V_A^2}\right) \frac{\partial E_y}{\partial x} + \kappa^2 E_y = 0 \tag{1.61}$$

where

$$\kappa^2 = \omega^2/v_A^2 - k_x^2 - k_z^2. \tag{1.62}$$

This equation has two singular solutions, when $\frac{\omega^2}{V_A^2} = k_z$ and when $\kappa^2 = 0$. The latter corresponds to the turning point x_t where the compressional mode is reflected, but part of the energy evanesces in the direction of increasing Alfvén wave gradient. The former corresponds to the resonance position x_r. At this point, the wave equation can be reduced to

15

$$\frac{\partial^2 E_y}{\partial x^2} + \frac{1}{x - x_r}\frac{\partial E_y}{\partial x} + \kappa^2 E_y = 0. \tag{1.63}$$

This equation has the form of the modified Bessel function of order zero with infinite solutions at $x = x_r$. However, from the work of Chen and Hasegawa (1974) and Southwood (1974), it is known that the singularity can be avoided if there is a small amount of dissipation in the system. This is a realistic situation, because the ionosphere is not perfectly reflecting and so energy of the FLR is lost over time. This sink can be represented by a small imaginary component in k_z, such that

$$k_z = k_{zr} + ik_{zi}. \tag{1.64}$$

With this assumption, the wave equation becomes

$$\frac{\partial^2 E_y}{\partial x^2} + \frac{1}{x - x_r + i\epsilon}\frac{\partial E_y}{\partial x} + \kappa^2 E_y = 0 \tag{1.65}$$

and the solution for the radial component of the electric field (see figure (1.6) is given by

$$E_x = \frac{-ik_y(\partial E_y/\partial x)}{\omega^2/V_A^2 - k_z^2 k_y^2}. \tag{1.66}$$

Now in the cold plasma limit with perfectly conducting ionospheric boundary conditions, the singularity at the resonance position is not avoided, except with the inclusion of the dispersive wave effects. In the low β limit ($\beta < \frac{m_e}{m_i}$), the net result is that the resonance would narrow to approximately $2\pi\lambda_e$ and then an inertial SAW would begin to propagate from the resonance layer in the direction of decreasing density (increasing Alfvén wave gradient). This situation is applicable to the region close to the ionosphere where the magnetic field is sufficiently high that magnetic pressure effects become dominant. In the limit $\beta > \frac{m_e}{m_i}$, the situation would be reversed with a kinetic Alfvén wave propagating in the direction of increasing density (decreasing Alfvén wave gradient).

The characteristic frequencies of high latitude FLRs are in the 1-4 mHz range and some seem to occur at well established frequencies (1.3,1.9,2.6 and 3.2 mHz) (Walker, 1992; Samson et al., 1991,1992a) Several theories have been proposed to explain this (Samson et al., 1992b; Wright, 1994) but there is as of yet no complete consensus as to the explanation. This question however is beyond the scope of this thesis and in the simulations to follow, we will pick parameters so that the FLR frequencies are in the mHz range.

Now, with reference to the profile in E_x (figure (1.6)), from the ideal MHD approximation, this radial electric field accompanies a similar profile in azimuthal velocity, u_y. For the simulations presented in the thesis, we will assume a narrow Gaussian in the place of the radial eigenmode for the initial SAW pulse as a close approximation. This neglect of a compressional mode driver is justified since this study is focused primarily with wave-particle interactions in the context of the standing SAWs.

16
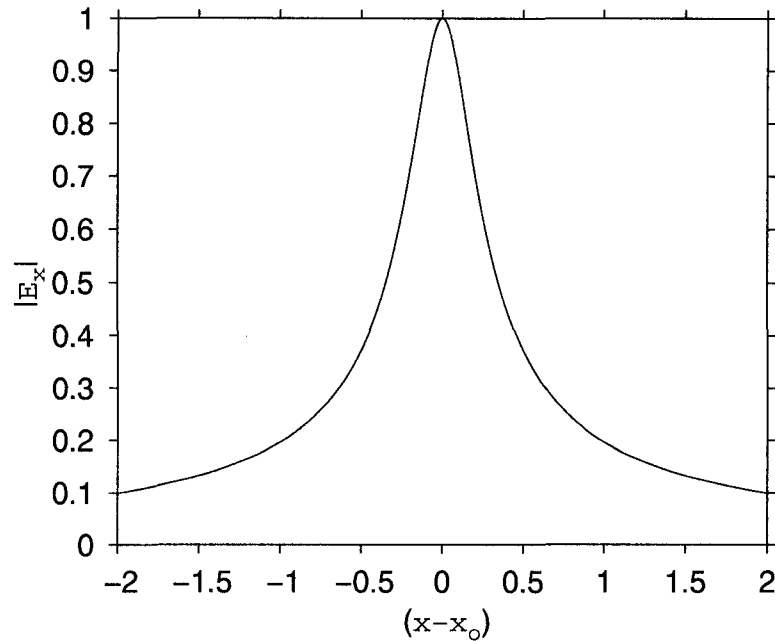
Figure 1.6: Example of solution for E_x near the resonance point.

1.9 Discrete Auroral Arcs and Field Line Resonances

The most energetic auroral displays are associated with the magnetospheric substorm which involves the stretching and dipolarization of the magnetosphere. These are generally most clearly visible during periods of high solar activity as this is when the solar wind can stretch the magnetotail to its greatest extent. However, a subclass of the aurora called discrete auroral arcs are still visible at much quieter times and it is with this type of arc that the work in the thesis pertains.

Discrete auroral arcs are very narrow, typically only tens of kilometers in latitudinal extent and can break up into even finer kilometer scale bands and vortices (see figure 1.7). They are usually associated with an "inverted-V" potential structure and satellite observations (Karlsson and Marklund, 1996; Carlson et al., 1998; Lotko et al.,1998) have measured electric fields and current densities on the order of mV/m and tens of $\mu A/m^2$ respectively along with precipitating electron energies on the order of hundreds of eV to tens of keV. This potential structure is often only on the order of ten kilometres wide, but extends from about 2 to 5 R_E above the Earth, along the dipolar magnetic field lines. This is known as the auroral acceleration region. The source of this inverted-V potential structure which accelerates the electrons is the current topic of much debate and there are several competing theories (see review paper by Borovsky, (1993)) which try to explain its formation.

As already noted, since the work of Hasegawa (1976) and Goertz and Boswell (1979), it has been known that dispersive Alfvén waves have a component of the electric field parallel to the ambient magnetic field. This means that these dispersive waves can accelerate

17

electrons parallel to the electric field and may potentially account for some auroral arcs. The short perpendicular wavelengths associated with these waves also are consistent with the fine structure observed in many auroral arcs. The low β nature of the plasma in this region implies inertial Shear Alfvén waves and so much research has been done in this direction (Hui and Seyler, 1992; Kletzing, 1994; Thompson and Lysak, 1996; Wei et al., 1994; Knudsen et al., 1996) and generally electron accelerations of various magnitudes have been found. However, in most cases, the source of the SAW is unclear. Hasegawa (1976) and Goertz (1984), considered the mode conversion of an MHD surface wave to to Shear Alfvén wave as one possibility, while another candidate involves the mode conversion between compressional modes and the SAW - the FLR (Chen and Hasegawa, 1974; Southwood, 1974; Inhester, 1987). The case for the latter has been enhanced over the last twenty years as many observations have made the FLR a well established phenomenon (Samson et al. 1992a; Fenrich et al., 1995) as well as many observations that link the FLR to discrete auroral arcs (Samson et al., 1991, 1996; Xu et al., 1993; Lotko et al., 1998).

Rankin et al. (1993a, 1993b), performed the first nonlinear resistive MHD simulations of the FLR in the box geometry. It was noted that FLRs can narrow sufficiently to reach inertial Aflvén wave scale lengths. Wei et al. (1994), extended this MHD model to include electron inertial effects. The parallel electric field magnitudes produced were however still several orders of magnitude below the observed values. The importance of the dipolar magnetic field and plasma inhomogeneity in the parallel direction to the enhancement of the Shear Alfvén wave parallel electric field was noted by Streltsov and Lotko (1997). Similarly, nonlinear simulations by Frycz et al. (1998) and Rankin et al. (1998) have shown that the pondermotive force effects can lead to density cavity formation above the auroral ionospheres and enhanced parallel electric fields as the cavities tend to enhance electron inertial effects.

However, even with the inclusion of nonlinear effects, the MHD simulations are able to reproduce the observed scale structure and current densities associated with auroral arc observations, but are unable to account for the observed parallel electric field. The conductivity of the MHD system is too high. Steltsov and Lotko (1999), were able to reproduce observed electric fields by the inclusion of anomalous resistivity in a linear 2-fluid MHD model. The anomalous resistive layer is caused by the interaction of the SAW with a microturbulent layer, but the source of the microturbulence is not addressed. Rankin et al. (1999) and Tikhonchuk et al. (2000), combined MHD with an electron kinetic equation using perturbation theory and were able define an Ohm's law with a conductivity matrix such that

$$j_{\parallel}(l) = \int \sigma(l',l) E_{\parallel}(l') dl' \qquad (1.67)$$

where l is the length along the field line. The conductivity matrix is derived from the integration of the electron kinetic equation and thus incorporates wave-particle interactions including mirror force effects not evident in the Generalized Ohm's Law. Although not a

18

trivial calculation, once the MHD current is specified, the necessary parallel electric field can be determined by the inversion of the convolution integral. With this formulation, they were able to show that wave-particle interactions reduced the nonlocal conductivity and led to parallel electric fields in the ionospheric regions comparable to those observed. This work highlighted the significance of mirror force trapping of current carrying electrons in the equatorial region as an important reason for the drop in conductivity. Therefore, the picture that emerges from these works is that the dispersive waves are not responsible in themselves for the magnitudes of the parallel electric fields observed, but may play an important role as the modulating influence that explains the fine structure seen in the arcs.

The next logical step in the approach to this problem is to attempt to model the FLR system with an actual system of electrons rather than the use of electron kinetic equation as the latter makes it necessary to a priori prescribe the form of the electron distribution function. As well this approach makes it straightforward to study of the interaction of the SAW system with the electron distribution function self consistently as a function of time.

The use of hybrid MHD-kinetic computer models for the study of auroral arc phenomena is very recent. Hui and Seyler (1992) used an approach similar in some ways to the model that will be presented here, but for the study of electron acceleration due to inertial Shear Alfvén wave breaking in the auroral acceleration region. Thompson and Lysak (1996) in studying electron acceleration due to inertial Alfvén wave pulses, used an algorithm to locally subtract energy used to accelerate an electron from the inertial Alfvén wave. Genot et al. (2000) used fully kinetic simulations to look at electron acceleration due to wave-particle interactions in localized density cavities. However, the work presented in this thesis is the first to attempt to self consistently model a full FLR system with a hybrid MHD-kinetic computational approach. It is also the first to do so in the natural dipolar coordinate system. This approach is used here to address a FLR system, but it is also applicable to other Standing Shear Alfvén wave systems in space plasmas such as solar coronal loops as well as transient SAWs.

1.10 Outline of Thesis

In this study, we shall introduce a new hybrid MHD-kinetic model to study wave-particle interactions in a standing Shear Alfvén wave system. Before progressing to a full description of the hybrid model, we will outline the 1D cold plasma MHD model of a standing Shear Alfvén wave including electron inertial effects in Chapter 2. This will serve to introduce the necessary physics along with technical details that are relevant to the rest of the thesis.

In Chapter 3, we outline the hybrid model for both cartesian (box) geometry and generalized curvilinear coordinates, with the latter part being broken down into cylindrical and dipolar coordinates.

Chapter 4 illustrates simulations for the box model with periodic and perfectly conducting boundary conditions. An analytical dispersion relation for the periodic Alfvén

19
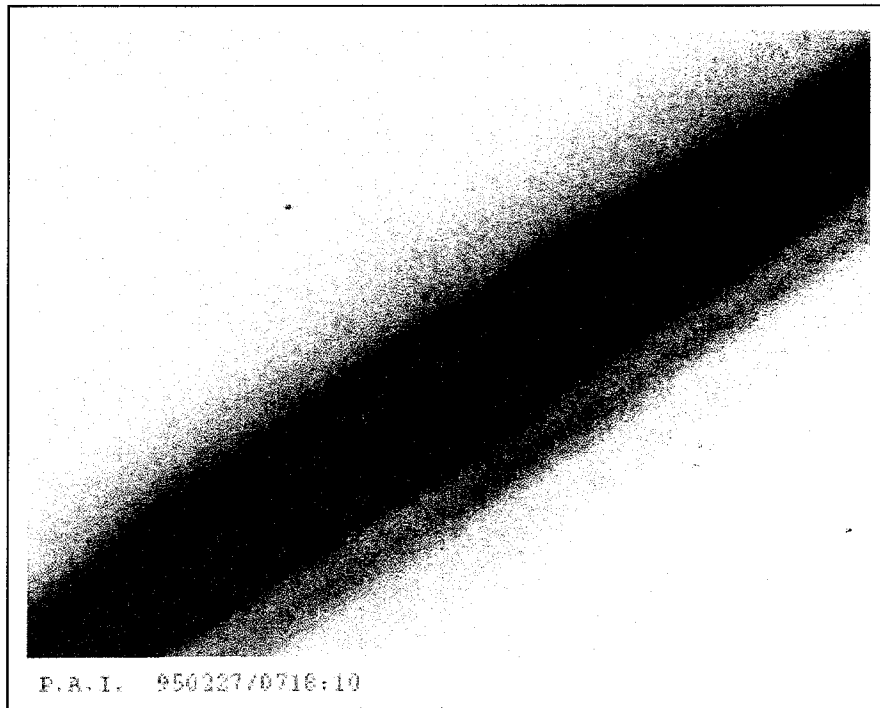
Figure 1.7: False colour image of an auroral arc. Photo by Dr. Trond Trondsen using the University of Calgary Portable Auroral Imager (P.A.I).

20

wave system is also presented and the predicted Landau damping rate is compared with that measured from the numerical simulations. In the fluid limit, the 2D results are also contrasted with the 1D results illustrated in Chapter 2.

Chapter 5 outlines the simulation results for the dipolar fluid and hybrid models with perfectly conducting ionospheric boundary conditions. The result of the cold plasma MHD fluid model are contrasted with the nonlinear MHD model developed by Voronkov (1998), while the hybrid model results are illustrated in the cold and warm plasma limits. Chapter 6 concludes the thesis and offers suggestions for both future research directions and model enhancements.

Chapter 2

1D Model of FLR with electron inertial effects

2.1 Preamble

In this chapter, a 1D fluid model of a FLR is developed from the cold plasma equations and the Generalized Ohm's Law. Simulations are presented for both the case $\lambda_e = 0$ and $\lambda_e \neq 0$. In the first case, the phase mixing of the resonance is evident, while in the latter, the formation of the inertial SAW is illustrated, propagating in the direction of increasing Alfvén wave speed.

The topics presented here are well addressed in the papers by Wei et al. (1994) and Rickard and Wright (1994). They are re-examined here to introduce the main characteristics of the FLRs that will be revisited in subsequent chapters. Also, the numerical techniques used for this code form the basis of the more advanced models to follow and a comparison will be made between the 1 and 2 D fluid simulations in Chapter 3.

2.2 1D cold plasma equations

For this simulation, the radial direction is denoted by x, the azimuthal direction by y and the field aligned direction by z. Periodicity is assumed in the y direction and the plasma velocities are chosen to vary as

$$\vec{u} = \left\{ \begin{array}{c} u_{xr}(x,t)sin(k_z z)e^{ik_y y} \\ iu_{yi}(x,t)sin(k_z z)e^{ik_y y} \\ 0 \end{array} \right\}$$

where the $sin(k_z z)$ implies velocity nodes at the ionospheres and the subscripts 'i' and 'r' denote the real and imaginary parts respectively. With these choices, the magnetic field components in turn vary as

$$\vec{b} = \left\{ \begin{array}{c} b_{xr}(x,t)cos(k_z z)e^{ik_y y} \\ ib_{yi}(x,t)cos(k_z z)e^{ik_y y} \\ b_{zr}(x,t)sin(k_z z)e^{ik_y y} \end{array} \right\}.$$

22

The perpendicular electric field is determined from the ideal MHD assumption $\vec{E}_\perp = -\vec{u} \times \vec{B}$. Linearizing, the components of the perpendicular electric field are given by

$$E_x = -u_y B_o = iu_{yi}(x,t)B_o sin(k_z z)e^{ik_y y} = E_x(x,t)sin(k_z z)e^{ik_y y}$$
$$E_y = u_x B_o = u_{xr}(x,t)B_o sin(k_z z)e^{ik_y y} = E_y(x,t)sin(k_z z)e^{ik_y y}.$$

For the parallel electric field, the Generalized Ohm's Law is used. With the variable choices quoted above this becomes

$$E_z = \mu_o \lambda_e^2 \frac{\partial j_z}{\partial t} = \mu_o \lambda_e^2 \frac{\partial j_z}{\partial t}(x,t)cos(k_z z)e^{ik_y y} = E_z(x,t)cos(k_z z)e^{ik_y y}$$

where $E_z(x,t) = \mu_o \lambda_e^2 \frac{\partial j_z(x,t)}{\partial t}$. With all these assumptions, the cold plasma equations take the form,

$$\frac{\partial u_x}{\partial t} = -\frac{B_o}{\mu_o \rho}(k_z b_x + \frac{\partial b_z}{\partial x})$$
$$\frac{\partial u_y}{\partial t} = -\frac{B_o}{\mu_o \rho}(k_z b_y + ik_y b_z)$$
$$\frac{\partial b_x}{\partial t} = ik_y E_z - k_z E_y$$
$$\frac{\partial b_y}{\partial t} = k_z E_x - \frac{\partial E_z}{\partial x}$$
$$\frac{\partial b_z}{\partial t} = \frac{\partial E_y}{\partial x} - ik_y E_x$$

where all the variables are now functions of x and t only.

2.3 Numerical Model

The fluid equations are solved using a predictor-corrector type method. The first order differential equation $\frac{dy}{dt} = F$ is finite differenced in time as follows

$$y_p^{t+\Delta t} = y^{t-\Delta t} + 2\Delta t F(y^t) \tag{2.1}$$

$$y^{t+\Delta t} = y^t + \frac{\Delta t}{2}[F(y^t) + F(y_p^{t+\Delta t})] \tag{2.2}$$

where the subscript 'p' denotes the predicted value. With this scheme, it is necessary to keep track of all values at three points in time, but the algorithm is very stable for long integration times. Since it is not possible to know, $j_z^{t+2\Delta t}$ in order to obtain $E_z^{t+\Delta t}$ from the Generalized Ohm's Law, the approximation $E_z^{t+\Delta t} = E_z^{t-\Delta t} + 2E_z^t$ was used. This was fine as long as the time step was sufficiently small.

23

The first order derivatives are evaluated using the standard two point formula.

$$\frac{\partial f}{\partial x} = \frac{f_{j+1} - f_{j-1}}{2\Delta x} \qquad (2.3)$$

where Δx, is the distance between adjacent points on the grid.

In order to normalize the fluid equations, the following set of variables is introduced

$$\vec{r}' = \frac{\vec{r}}{L_x}; t' = \frac{t}{t_N}\vec{B}' = \frac{\vec{B}}{B_o}; \vec{V}' = \frac{\vec{V}}{V_N}; \vec{\rho}' = \frac{\rho}{\rho_O}; \vec{j}' = \frac{\vec{j}}{j_N}; \vec{E}' = \frac{\vec{E}}{E_N} \qquad (2.4)$$

where $L_x = 1\ R_E$, $\rho_N = \rho(x = 0)$, $V_N = \sqrt{B_o^2/(\mu_o \rho_N)}$, $t_N = \frac{L_x}{V_N}$, $j_N = B_o/(\mu_o L_x)$ and $E_n = v_N B_o$. In the set of nondimensional variables, the cold plasma equations become

$$\frac{\partial u_x}{\partial t} = -\frac{1}{\rho}(k_z b_x + \frac{\partial b_z}{\partial x})$$

$$\frac{\partial u_y}{\partial t} = -\frac{1}{\rho}(k_z b_y + i k_y b_z)$$

$$\frac{\partial b_x}{\partial t} = i k_y E_z - k_z E_y$$

$$\frac{\partial b_y}{\partial t} = k_z E_x - \frac{\partial E_z}{\partial x}$$

$$\frac{\partial b_z}{\partial t} = \frac{\partial E_y}{\partial x} - i k_y E_x$$

where the primes have been left out for simplicity of notation.

Although, the equations are solved in nondimensional form, all values for the initial variables were chosen to approximately correspond to conditions in the dayside equatorial magnetosphere before being made nondimensional. The ambient magnetic field B_o and density ρ_N were chosen to be 10 nT and $10^5\ m_p m^{-3}$ respectively, where m_p is the proton mass in kg. This yields a value of $v_N = 6.9 \times 10^5\ m/s$. The Alfvén speed and density profiles were normalized to both have values of 1 at $x = 0$ where the simulation grid goes from $x = 0$ to $x = 1.2$. The nondimensional Alfvén velocity profile is then specified with the function

$$v_A = tanh(\alpha x + \phi) + \beta \qquad (2.5)$$

where $\alpha = 7$, $\beta = 2$ and $\phi = -0.5$ and because of the constant ambient magnetic field, the nondimensional density is simply given by

$$\rho = \frac{1}{v_A^2}. \qquad (2.6)$$

Both functions are displayed in figure (2.1). The corresponding electron inertial length profile is calculated via the definition given in Chapter 1

$$\lambda_e = \sqrt{\frac{m_p m_e}{\rho e^2}} \qquad (2.7)$$

24
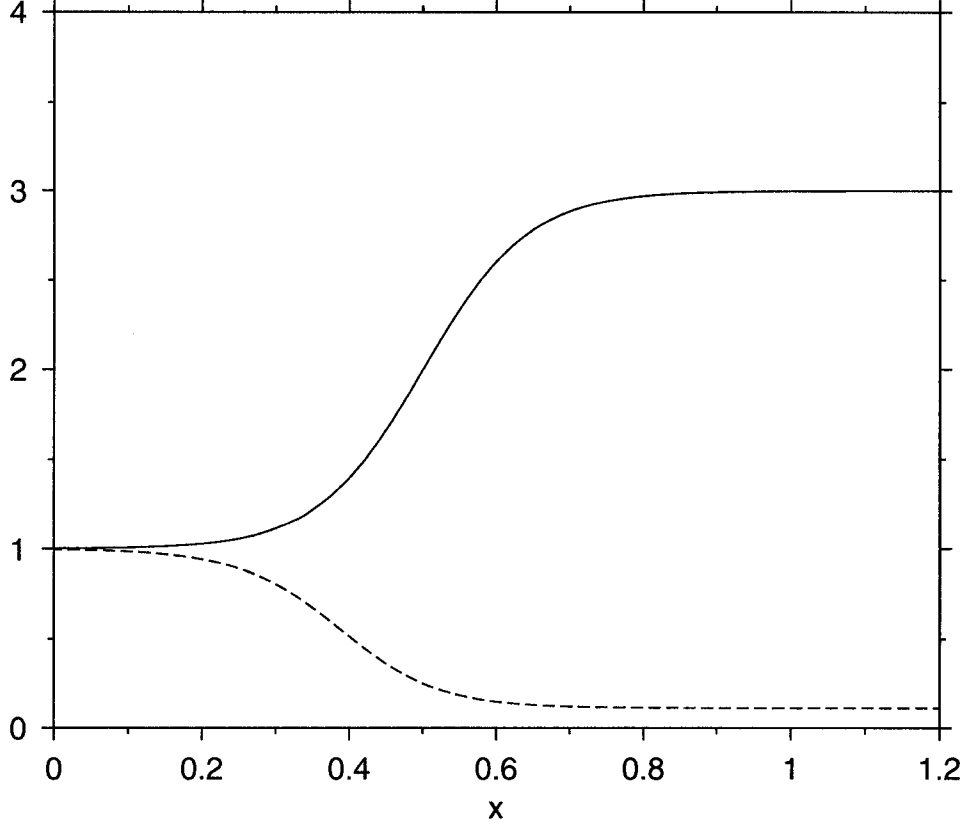
Figure 2.1: Graphs of V_A vs x (solid line) and ρ vs x (dashed line).

in MKS units and then normalized by the characteristic length, L_x. The profile is displayed in figure (2.2).

In this work, the evolution of the standing SAW is the prime point of interest, not the mode conversion process that results in its formation. Therefore for this simulation, a toroidal Shear mode ($u_x = 0$) with a Gaussian shape in x around the resonance position is assumed for an initial condition (see Figure 2.3). The value $k_y = 0.2/R_E$ is chosen so that most of the energy stays in the toriodal mode. For the parallel wave number, the value $k_z = \frac{2\pi}{18R_E}$ was chosen because 18 R_E is the approximate length of the L=8 dipolar magnetic field line.

2.3.1 Boundary Conditions

For the boundaries at $x = 0, L_x$, perfectly reflecting boundary conditions in x are assumed. This implies $u_x = 0$ at $x = 0, L_x$. This assumption is equivalent to the magnetic field going to a very large value instantly at the boundaries. From this assumption and the ideal MHD approximation, it is evident then that $E_y = 0$ as well.

Now assuming periodicity in time ($e^{i\omega t}$), the Generalized Ohm's Law for the parallel electric field becomes,

25
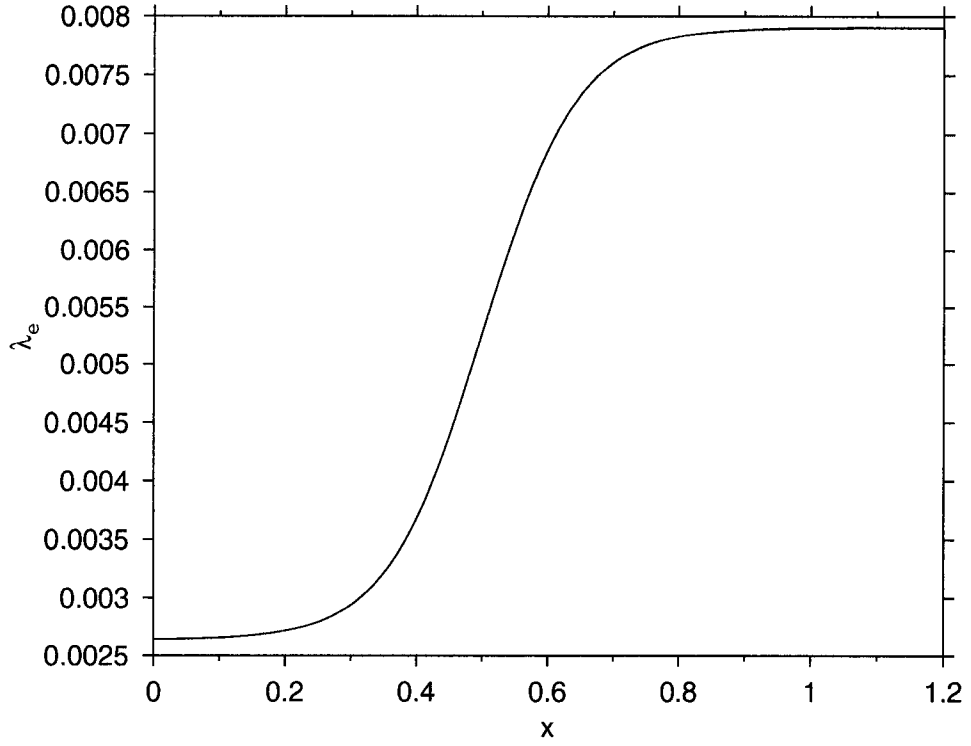
Figure 2.2: Graph of electron inertial length (nondimensional), λ_e, vs x.
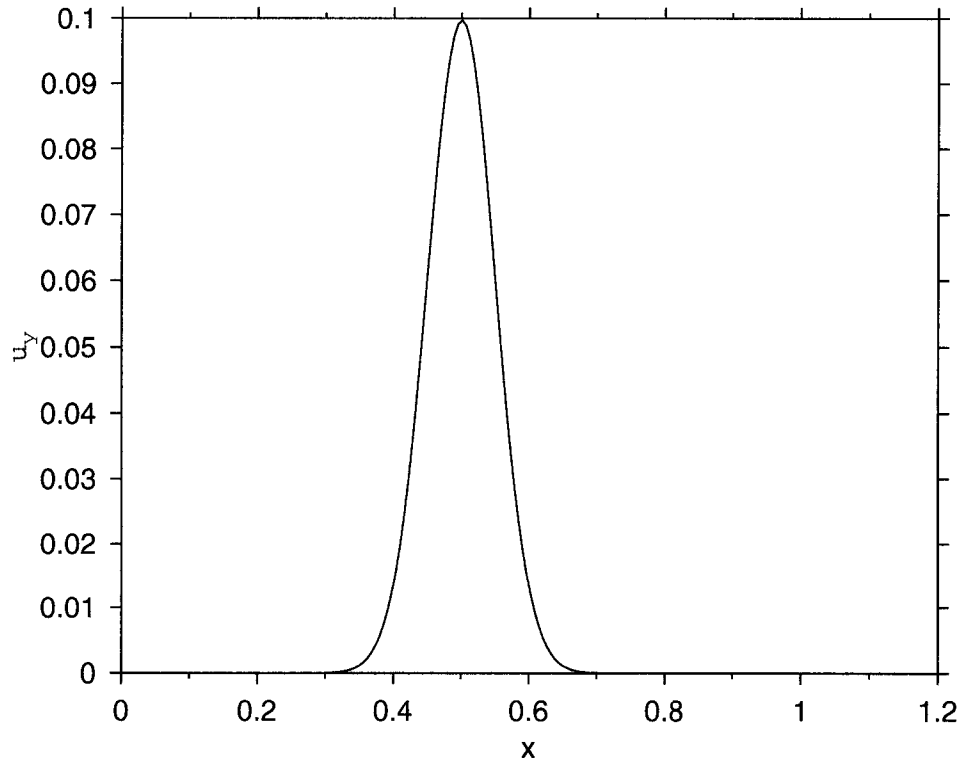
Figure 2.3: Graph of initial Shear Alfvén velocity profile.

26

$$E_z = i\omega\lambda_e^2 j_z \tag{2.8}$$

and for the boundaries far from the resonance, $j_z = 0$ and so $E_z = 0$. Similarly, the x component of Faraday's law becomes

$$i\omega b_x = ik_y E_z - k_z E_y \tag{2.9}$$

and with $E_y = E_z = 0$ at $x = 0, L_x$, therefore $b_x = 0$. From the x component of the momentum equation

$$i\omega u_x = -\frac{B_o}{\rho\mu_o}[k_z b_x + \frac{\partial b_z}{\partial x}] \tag{2.10}$$

and since, $u_x = b_x = 0$, then $\frac{\partial b_z}{\partial x} = 0$. From the y component of the momentum equation

$$i\omega u_y = -\frac{B_o}{\rho\mu_o}[k_z b_y + ik_y b_z]. \tag{2.11}$$

Taking the derivative with respect to x,

$$i\omega\frac{\partial u_y}{\partial x} = [k_z\frac{\partial b_y}{\partial z} - k_y\frac{\partial b_z}{\partial x}] \tag{2.12}$$

where the functional dependence of the Alfvén velocity implies $\frac{\partial V_A}{\partial x} = 0$ at the radial boundaries. From the y component of Faraday's law, we also have

$$i\omega\frac{\partial b_y}{\partial x} = \frac{\partial^2 E_x}{\partial x^2} - \frac{\partial}{\partial x}(\frac{\partial E_x}{\partial z}). \tag{2.13}$$

Comparison of these two equations illustrates that both are satisfied only if $\frac{\partial u_y}{\partial x} = \frac{\partial b_y}{\partial x} = 0$ and since $E_x = u_y B_o$, it is consistent that $\frac{\partial E_x}{\partial x} = 0$.

In all cases, the boundary conditions are enforced across the first two and last two grid cells. For the boundary conditions $F(0) = 0$, then $F_1 = -F_2$, while for $\frac{\partial F}{\partial x}(0) = 0$, $F_1 = F_2$ where the subscripts 1 and 2 indicate the first and second grid points respectively.

2.4 Evolution of FLR

For the following simulations 250 grid points were used for the $\lambda_e = 0$ case while 200 grid points were used for $\lambda_e \neq 0$. The larger number in the former case is to more accurately capture the phase mixing. For both simulations, 100,000 time steps were used for 20 Alfvén periods. Figure (2.4) illustrates the evolution of the shear velocity u_y through 15 periods for both $\lambda_e = 0$ and $\lambda_e \neq 0$ on the left and right hand sides respectively. For the $\lambda_e = 0$ case, the resonance narrows continually due to phase mixing. This phase mixing is the result of the radial Alfvén speed gradient which means that each field line has its own slightly different eigenfrequency. Over time each field line becomes more and more out of phase with its neighbour evolving into finer structure evident. Since there are no dispersive

27
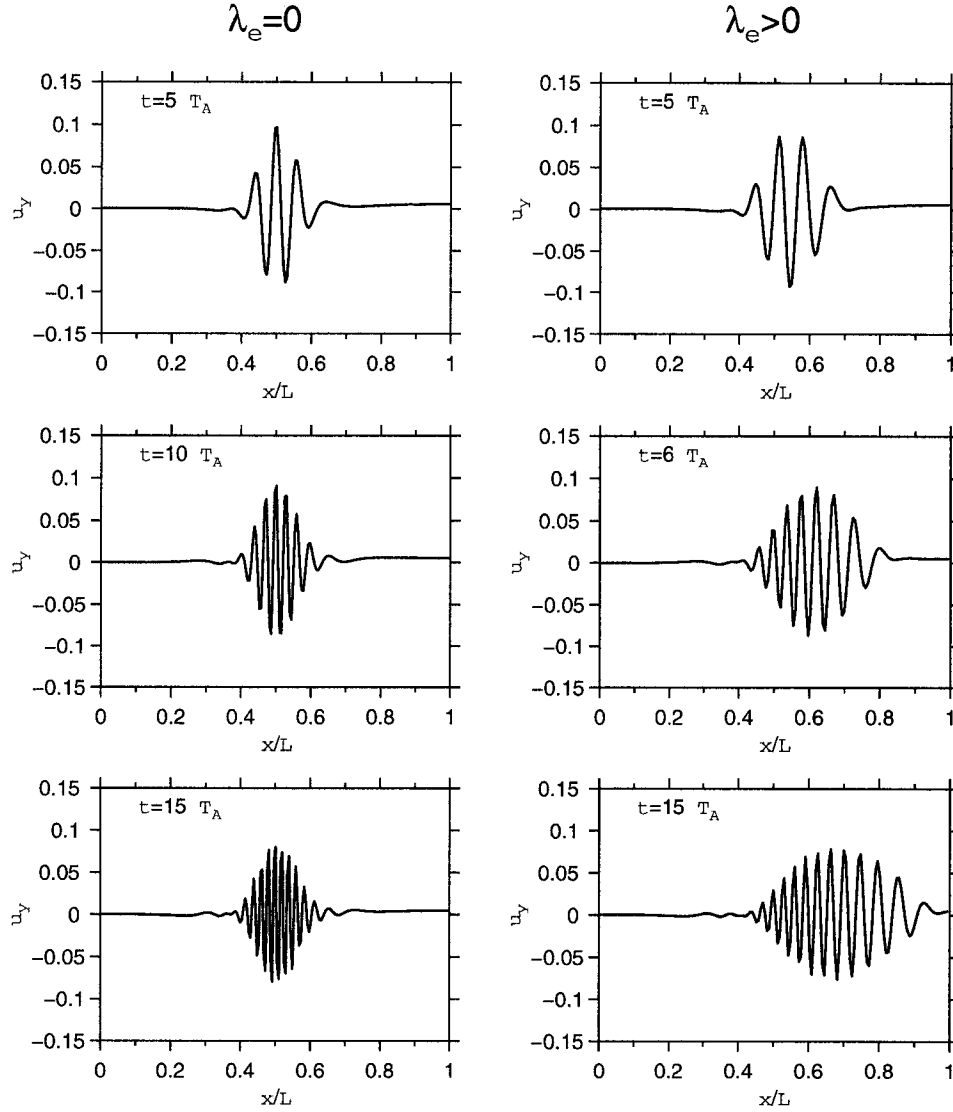
Figure 2.4: Time slices of u_y vs x for the case of $\lambda_e = 0$ (left side) and for the case of $\lambda_e \neq 0$.

waves in this limit, there is no radial propagation and packet retains the width of the initial Gaussian profile. Mathematically, the narrowing within the packet would continue until a singular solution is reached, but for the numerical case, it narrows until the resonance is on the order of the grid scale and the model becomes unstable.

In the $\lambda_e \neq 0$ case, the resonance only narrows until the scale length of about $2\pi\lambda_e$ is reached at which point an inertial SAW begins to propagate in the direction of increasing Alfvén wave speed. For the present model parameters, $2\pi\lambda_e \approx 0.05$.

The SAW dispersion relation in the limit $\lambda_e = 0$, $\omega = k_z V_A$, yields a value for the frequency $\omega = 0.0755s^{-1}$ for the parameters considered here. This results in a period $T_A = 83.2s$. In order to confirm this, the value of u_y at x=0.5 is plotted as a function of time in figure (2.5) and it is clearly evident that the predicted and actual period are in good

28
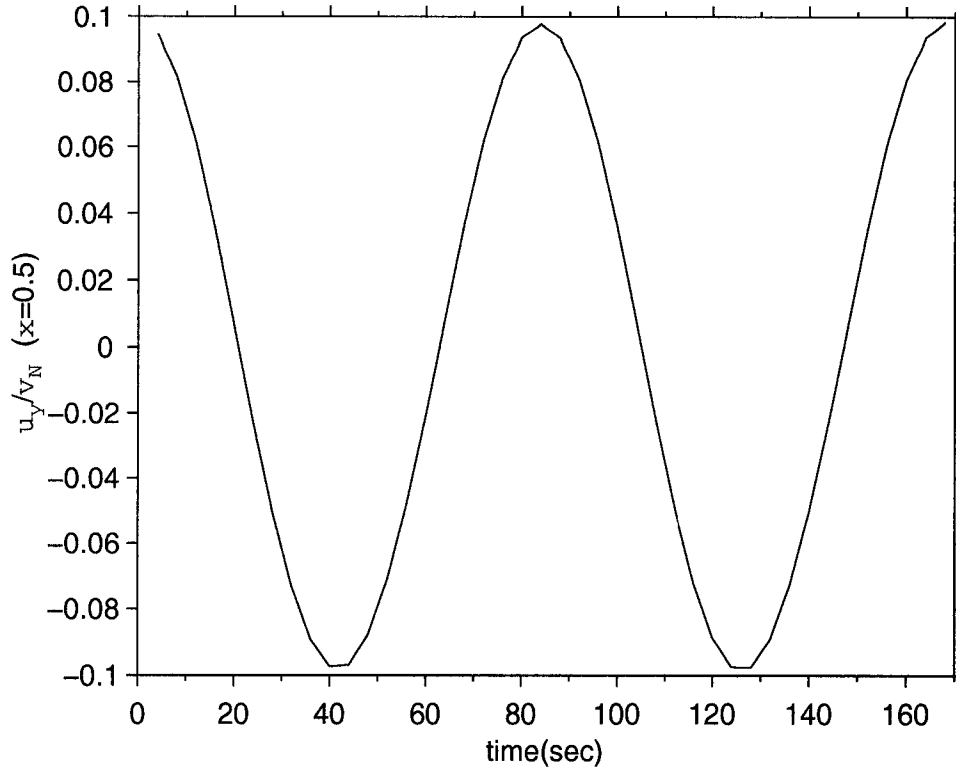
Figure 2.5: Plot of u_y at x=0.5 as a function of time.

agreement.

2.4.1 Energy

The energy density of a cold plasma system (without electron inertia) is given by (Rickard and Wright, 1994)

$$\epsilon = \frac{\rho}{2}(u_x^2 + u_y^2) + \frac{1}{2\mu_o}(b_x^2 + b_y^2 + b_z^2). \tag{2.14}$$

There is additional energy in the ambient magnetic field B_o, but in the linear approximation this is a constant value and is not considered in this calculation. The total energy of the perturbations

$$E_T = \int_0^1 \epsilon(x)dx \tag{2.15}$$

should be conserved, and this is confirmed in figure (2.6) illustrating the effectiveness of the predictor-corrector scheme.

2.4.2 Summary

The 1D simulations illustrate the phenomenon of phase mixing and the propagation of an inertial SAW in the direction of increasing Alfvén wave speed. The eigenfrequency of the

29
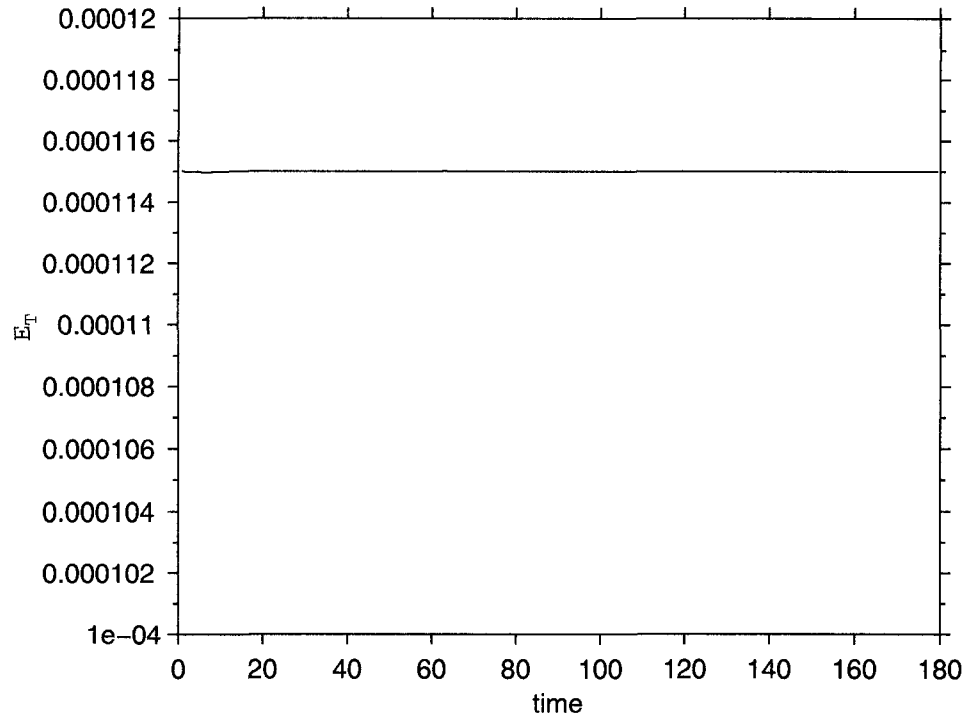
Figure 2.6: Total Energy vs time for $\lambda_e = 0$.

resonance agrees well with that prediction from the SAW dispersion relation.

The predictor-corrector scheme is very stable for the solution of the cold plasma equations with the Generalized Ohm's law for long integration times. The algorithm conserves energy in the $\lambda_e = 0$ limit to a high degree of accuracy.

30

Chapter 3

Hybrid kinetic-MHD model

3.1 Preamble

In Chapter 1, the failure of the MHD approach to account for the observed electric fields in FLRs was summarized along with the limitations of the hybrid kinetic-MHD approaches considered to date. In this chapter a new hybrid MHD-kinetic approach is introduced using the 2D cold plasma equations and a kinetic system of electrons, the dynamics of which are solved using the guiding center equations. The closure between the two systems is achieved via the parallel electric field.

This chapter is divided into three main parts. The first part reviews the basic particle dynamics in electromagnetic fields and introduces the guiding center equations. The second part introduces the hybrid box model, while the third covers the hybrid model in general curvilinear coordinates and discusses the application to dipolar coordinates. The simulations using the box model are summarized in Chapter 4, while Chapters 5 presents the dipolar model results.

3.2 Charged Particle Motion in Electromagnetic fields

The motion of a particle in an electromagnetic field is governed by the Lorentz equation

$$\frac{d\vec{v}}{dt} = \frac{q\vec{E}}{m} + \frac{q}{m}(\vec{v} \times \vec{B}) \tag{3.1}$$

and in the limit of $E = 0$ and constant magnetic field, the gyromotion of the charged particle around the magnetic field line is well known (see figure (3.1)). The gyrofrequency or cyclotron frequency of the orbit is given by

$$\omega_g = \frac{qB}{m} \tag{3.2}$$

while the gyroradius, r_g is

$$r_g = \frac{v_\perp}{|\omega_g|} = \frac{mv_\perp}{|q|B}. \tag{3.3}$$

31
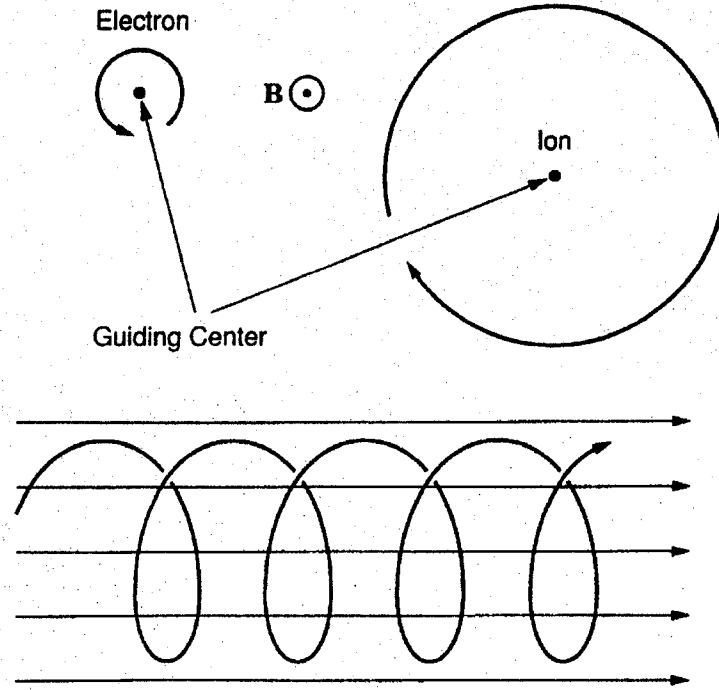
Figure 3.1: Top: Gyromotion of electrons and ions in a constant magnetic field. Bottom: Motion of an ion in a uniform magnetic field (Baumjohann et al. 1996).

Ignoring the gyromotion, there are several drifts motions of the guiding center. In general, a charged particle subject to a general force $\vec{F}$ will experience a drift motion due to that force, $\vec{v}_F$ given by

$$\vec{v}_F = \frac{\vec{F} \times \vec{B}}{qB^2}. \tag{3.4}$$

3.2.1 Electric Field Drifts

If a static electric field is introduced to the constant magnetic field case, the well known $\vec{E} \times \vec{B}$ drift results (figure (3.2))

$$\vec{v}_E = \frac{\vec{E} \times \vec{B}}{B^2}. \tag{3.5}$$

There is no current associated with the drift because both ions and electrons drift in the same direction. In a time dependent electric field there is an additional drift to consider in the polarization drift

$$\vec{v}_p = \frac{m}{qB^2} \frac{\partial \vec{E}}{\partial t}. \tag{3.6}$$

In this case, electrons and ions drift in opposite directions and so there is a net polarization current given by

32
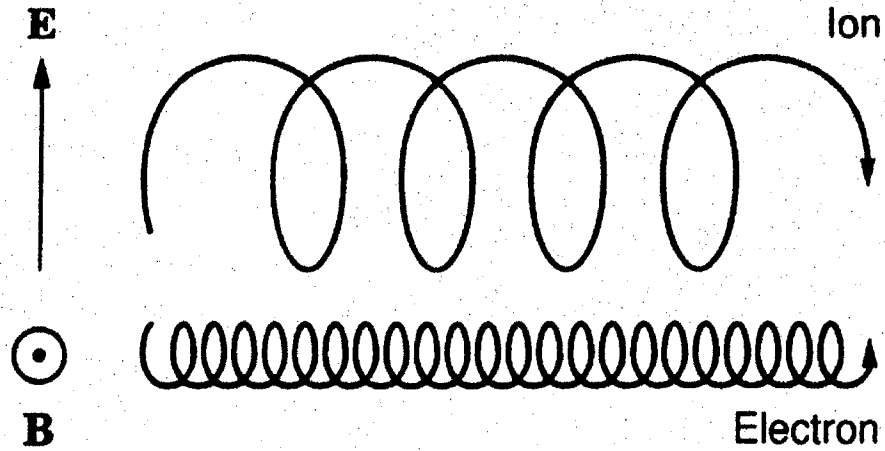
Figure 3.2: Particle drifts in crossed electric and magnetic fields (Baumjohann et al., 1996).
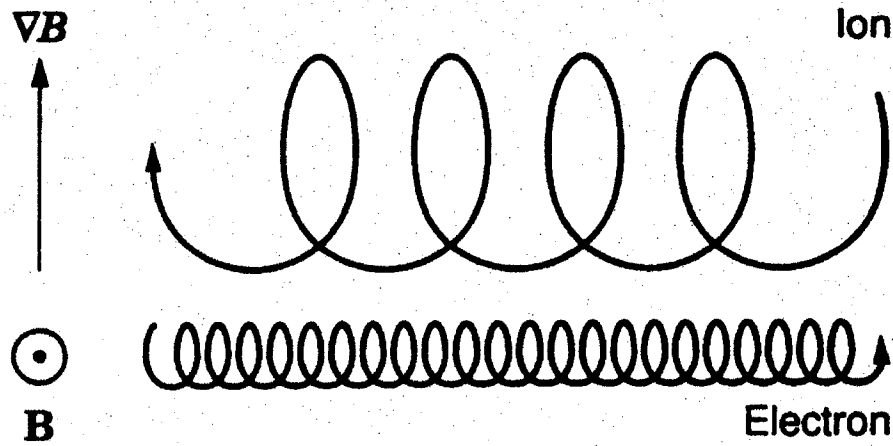
Figure 3.3: Gradient Drift of the guiding center (Baumjohann et al., 1996).

$$\vec{j}_p = n_e e (\vec{v}_{pi} - \vec{v}_{pe}) = \frac{n_e(m_i + m_e)}{B^2} \frac{d\vec{E}_\perp}{dt}. \tag{3.7}$$

As stated in Chapter 1, the ion current perpendicular to the dipolar field lines is associated with this drift. The more massive ions can move across the magnetic field lines and the electrons are forced to move along the field line forming a parallel current to maintain the quasineutrality of the plasma.

3.2.2 Magnetic Field Drifts

For motion in a nonuniform magnetic Field $\vec{B}$, there are two drift motions, one due to the curvature in the field

33
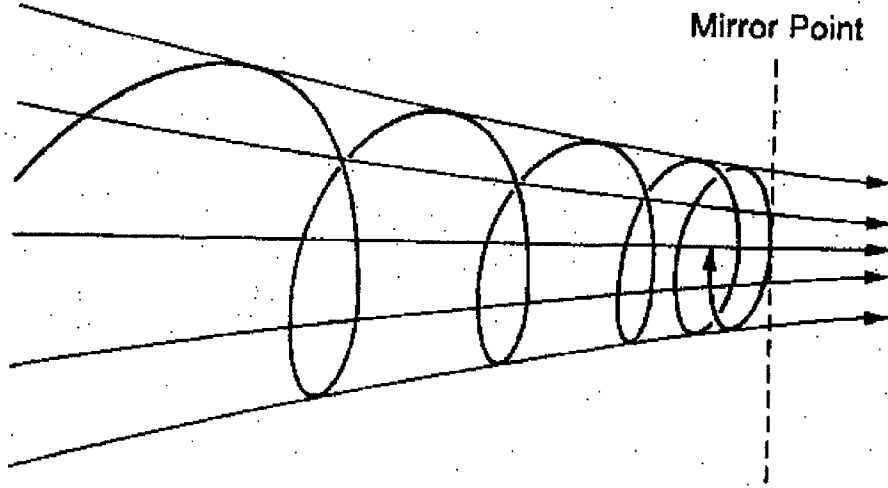
Figure 3.4: Motion of a proton in a dipolar magnetic field (Baumjohann et al., (1996)).

$$\vec{W}_c = \frac{mv_{\parallel}^2}{qB^4}[\vec{B} \times (\vec{B} \cdot \nabla)\vec{B}] \tag{3.8}$$

and one due to the gradient (see figure (3.3))

$$\vec{W}_{\nabla_B} = \frac{mv_{\perp}^2}{2qB^3}(\vec{B} \times \nabla B). \tag{3.9}$$

In a dipolar magnetic field, both gradient and curvature drifts result in motion perpendicular to the ambient magnetic field lines. Both these drifts are in the same direction for the same charged particle, but electrons and ions gradient and curvature drift in opposite directions.

3.2.3 Mirroring

For the case where the guiding center is moving along an inhomogeneous magnetic field, there is a force which acts in opposition to the motion of the particle when the magnetic field lines converge called the mirror force

$$m\frac{dv_{\parallel}}{dt} = -\mu\nabla_{\parallel}B \tag{3.10}$$

where $\mu = \frac{mv_{\perp}^2}{2B}$ is the magnetic moment. Figure (3.4) illustrates the reflection of an ion in a converging magnetic field due to the mirror force. It is important to note that the magnetic moment is an invariant of the motion.

The ratio of the perpendicular and parallel velocities defines an angle known as the pitch angle, α, and is given by

$$\alpha = tan^{-1}\frac{v_{\perp}}{v_{\parallel}} \tag{3.11}$$

34
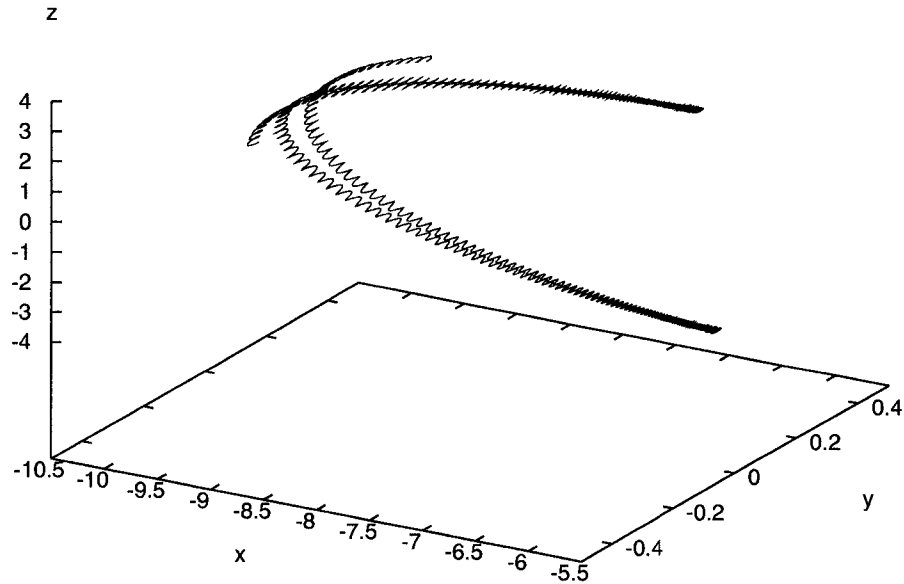
Figure 3.5: Motion of a proton in a constant dipolar magnetic field.

where $v_{\parallel} = vcos(\alpha)$ and $v_{\perp} = vsin(\alpha)$. At the mirroring point $v_{\parallel} = 0$ and $\alpha = \frac{\pi}{2}$. In a dipolar magnetic field, the pitch angle in the equatorial plane is denoted by α_o. The value of this angle is indicative of the mirroring position of the charged particle in the dipolar field as will be seen in the summary of the dipolar model. The smaller the equatorial pitch angle, the closer to the earth the particles mirroring position is located.

3.2.4 Particle motion in a dipolar magnetic field

Figure (3.5) illustrates the motion of a proton in a dipolar magnetic field. Evident is the gyromotion of the proton around the field line, the mirroring due to the convergence of the magnetic field line and the azimuthal motion due to gradient and curvature drifts.

For electrons, the azimuthal drifts are very slow and so the changes in any azimuthal fields due to change in particle position is of secondary importance. Therefore, for the hybrid model developed here, the azimuthal drifts are neglected, and the only motions that will be considered for the electrons is the field aligned motion and the $\vec{E} \times \vec{B}$ drift.

35

3.3 Guiding Center Equations

The gyroradius of the electrons is a lot smaller than any other scale lengths in the FLR system. Therefore, instead of using the full Lorentz equations of motion for the electrons, it is possible to use another set of equations that follow only the motion of the electrons guiding center, r_g. These are known simply as the guiding center equations (see Parks, (1991)) and including only the $\vec{E} \times \vec{B}$ drift and the mirroring force, they are expressed as

$$\frac{\partial v_{||}}{\partial t} = -eE_{||} - \mu_m \nabla_{||} B \tag{3.12}$$

$$\frac{d\vec{r_g}}{dt} = \vec{v_{||}} + \vec{v_\perp} \tag{3.13}$$

where $\vec{v_{||}} = v_{||} \frac{\vec{B}}{B}$ and

$$\vec{v_\perp} = \frac{\vec{E} \times \vec{B}}{B^2}. \tag{3.14}$$

For the straight magnetic field configuration in the box model used in Chapter 2, the mirror force vanishes and the linearized guiding center equation take the form

$$\frac{\partial v_{gz}}{\partial t} = -eE_z \tag{3.15}$$

$$\frac{\partial r_{gz}}{\partial t} = v_{gz} \tag{3.16}$$

$$\frac{\partial r_{gx}}{\partial t} = \frac{v_{gz} b_x}{B_o} + \frac{e_y}{B_o}. \tag{3.17}$$

3.4 Hybrid MHD-kinetic Box Model

As already stated, the hybrid MHD-kinetic model couples the cold plasma MHD equations with a kinetic system of electrons, the dynamics of which are governed by the guiding center equations. It is a two dimensional model, including the field aligned and the radial directions, denoted by z and x respectively in the box geometry. (figure (3.6)).

3.4.1 Model equations

Instead of choosing periodicity in the azimuthal direction as in Chapter 2, u_x is chosen to have an azimuthal dependence of $sin(k_y y)$. With this assumption, the rest of the fluid, magnetic and electric field components vary as

$$\vec{u} = \left\{ \begin{array}{c} u_x(x, z, t) sin(k_y y) \\ u_y(x, z, t) cos(k_y y) \\ 0 \end{array} \right\}$$

36
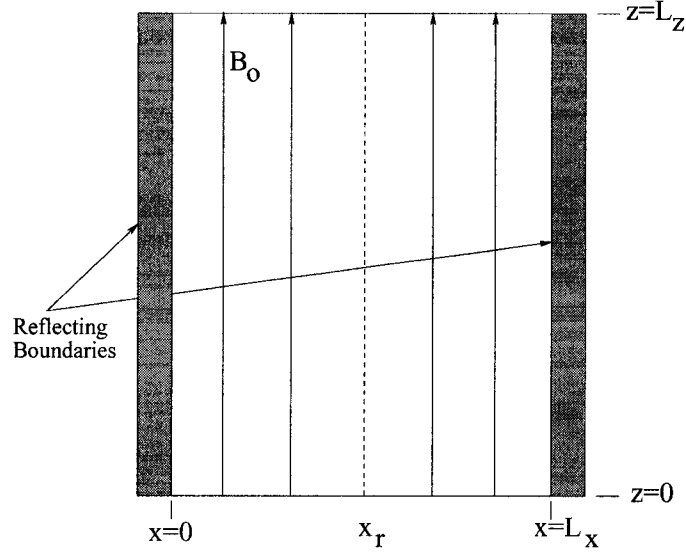
Figure 3.6: Two dimensional box model.

$$\vec{b} = \left\{ \begin{array}{l} b_x(x,z,t)sin(k_y y) \\ b_y(x,z,t)cos(k_y y) \\ b_z(x,z,t)sin(k_y y) \end{array} \right\}$$

$$\vec{e} = \left\{ \begin{array}{l} e_x(x,z,t)cos(k_y y) \\ e_y(x,z,t)sin(k_y y) \\ e_z(x,z,t)cos(k_y y) \end{array} \right\}$$

and the two dimensional cold plasma equations are denoted by

$$\frac{\partial u_x(x,z,t)}{\partial t} = \frac{B_o}{\mu_o \rho}(\frac{\partial b_x(x,z,t)}{\partial z} - \frac{\partial b_z(x,z,t)}{\partial x})$$

$$\frac{\partial u_y(x,z,t)}{\partial t} = \frac{B_o}{\mu_o \rho}(\frac{\partial b_y(x,z,t)}{\partial z} - k_y b_z(x,z,t))$$

$$\frac{\partial b_x(x,z,t)}{\partial t} = \frac{\partial E_y(x,z,t)}{\partial z} - \frac{\partial E_z(x,z,t)}{\partial y}$$

$$\frac{\partial b_y(x,z,t)}{\partial t} = \frac{\partial E_z(x,z,t)}{\partial x} - \frac{\partial E_x(x,z,t)}{\partial z}$$

$$\frac{\partial b_z(x,z,t)}{\partial t} = \frac{\partial E_x(x,z,t)}{\partial y} - \frac{\partial E_y(x,z,t)}{\partial x}.$$

The perpendicular electric field values are determined again via the ideal MHD approximation, but for the parallel electric field, the use of the Generalized Ohm's law is abandoned for an algorithm to be introduced in a subsequent section.

Similarly, the guiding center equations become

37

$$\frac{\partial v_z(x,y,z,t)}{\partial t} = -eE_z(x,z,t)cos(k_y y) \tag{3.18}$$

$$\frac{\partial r_{gz}}{\partial t} = v_z \tag{3.19}$$

$$\frac{\partial r_{xz}}{\partial t} = \frac{1}{B_o}(v_z b_x(x,z,t) + e_y(x,z,t))sin(k_y y) \tag{3.20}$$

where the mirror term is neglected because of the straight magnetic field configuration.

3.4.2 Numerical Notes

The normalizations, radial boundary conditions and method of solutions used in this model are exactly the same as already outlined in Chapter 2. The one significant difference is the use of a higher order spatial finite differencing scheme for the first derivative, given by

$$\frac{\partial f}{\partial x} = \frac{-f_{j-2} + 8f_{j-1} - 8f_{j+1} + f_{j+2}}{12\Delta x} \tag{3.21}$$

in order to reduce noise and make the coupling more stable. The model uses a rectangular grid with constant spacing in each direction, the size of which can be specified independently.

With respect to the field aligned boundary conditions, two models exist, one with periodic boundary conditions and one with perfectly conducting boundary conditions. The application of each will be summarized in Chapter 4.

3.4.3 Particle moment interpolation

All the fluid fields are solved at the set grid points, but the electrons themselves are free to move anywhere in the plane. Therefore it is necessary to have some scheme to interpolate the particle moment information onto the fluid grid. This is achieved via the use of the Particle Shape function $S(\vec{x}, \vec{x}_i)$. Figure (3.7), illustrates bilinear weighting, where each of the areas defined by a given lower case letter is assigned to the grid point denoted by the same letter in upper case. Therefore, for the velocity v_i, for example, the fraction

$$\frac{a}{a+b+c+d}v_i \tag{3.22}$$

is assigned to grid point A. In terms of the particle shape function, the first two moments of the distribution function, electron number density, n_e, and electron parallel current, j_e, are denoted by,

$$n_e = \sum_i S(\vec{x}, \vec{x}_i)$$

$$j_e = -e\sum_i v_i S(\vec{x}, \vec{x}_i).$$

38
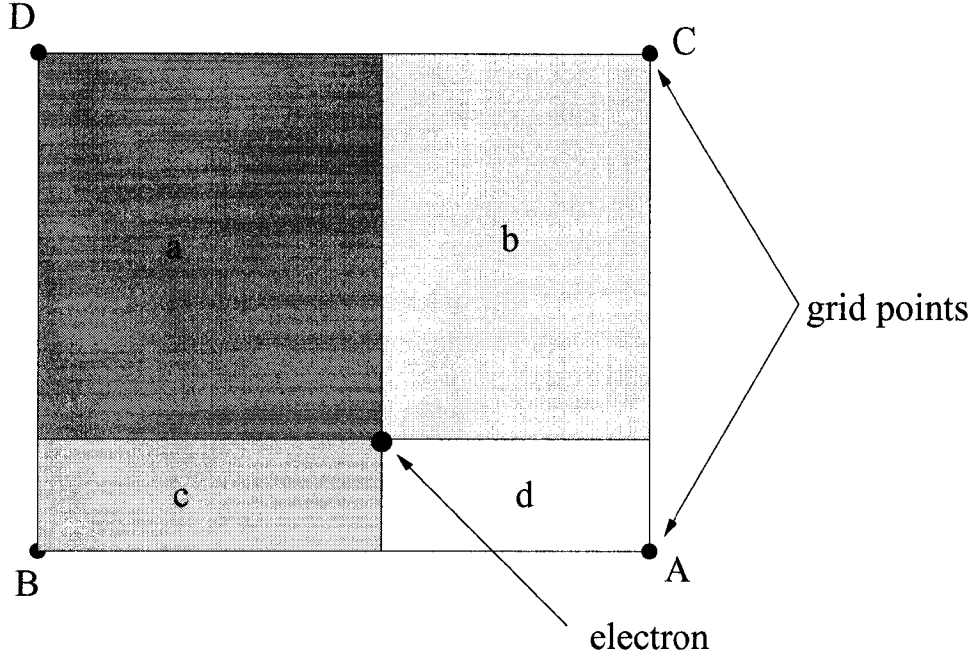
Figure 3.7: Bilinear interpolation grid. Areas denoted by lower case letters apply to the grid point denoted by the same letter in upper case.

In order to interpolate the fields to the particle position $F(\vec{r}_{gi})$, the same weighting is used, such that

$$F(\vec{r}_g) = \frac{AF(\vec{r}_A) + BF(\vec{r}_B) + CF(\vec{r}_C) + DF(\vec{r}_D)}{a + b + c + d}. \tag{3.23}$$

The model itself uses the higher order biquadratic spline routine where the interpolation utilizes 9 adjacent points.

3.4.4 Particle loading and velocity assignment.

For the simulations to be considered in Chapter 3, the electron density will be allowed to vary in the x direction, but will be constant in the z direction. To accomplish the loading, there are a user specified number of assigned electron positions in each direction, n_{p_x} and n_{p_z} where $n_p = n_{p_x} n_{p_z}$ is the total number of user specifed electrons. The positioning of the n_{p_x} electrons in the radial direction is assigned by a cumulative probability approach (Gould et al., 1996) using a user specified density function. Once these positions are assigned n_{p_z} electrons are placed at each position equally spaced in z.

The velocities are assigned to the electrons using the cumulative probability approach, but with a maxwellian function given by

$$f(v_z) = \frac{n}{\sqrt{\pi} v_{th}} exp(-\frac{v_z^2}{v_{th}^2}) \tag{3.24}$$

as the probability distribution function where $v_{th} = \sqrt{2 k_B T / m_e}$.

39

3.4.5 Parallel Electric Field Formalism

Taking the partial time derivative of Ampere's Law and combining with Faraday's law yields

$$-\nabla \times (\nabla \times \vec{E}(\vec{x})) = \mu_o \frac{\partial \vec{j}(\vec{x})}{\partial t}. \tag{3.25}$$

Using the vector identity $\nabla \times (\nabla \times \vec{E}) = \nabla(\nabla \cdot \vec{E}) - \nabla^2 \vec{E}$ this becomes

$$\nabla^2 \vec{E}(\vec{x}) - \nabla(\nabla \cdot \vec{E}(\vec{x})) = \mu_o \frac{\partial \vec{j}(\vec{x})}{\partial t} \tag{3.26}$$

and taking only the z component yields

$$\nabla^2 \vec{E}_z(\vec{x}) - \frac{\partial(\nabla \cdot \vec{E}(\vec{x}))}{\partial z} = \mu_o \frac{\partial j_z(\vec{x})}{\partial t}. \tag{3.27}$$

For the FLR system, the parallel current is entirely due to the electrons and so j_z can be replaced by the electron current, $j_e(\vec{x}) = -e \sum_i v_i S(\vec{x}, \vec{x}_i)$ (where $v = v_z$). Substituting this in for j_z and expanding the time derivative yields

$$\nabla^2 \vec{E}_z(\vec{x}) - \frac{\partial(\nabla \cdot \vec{E}(\vec{x}))}{\partial z} = -e\mu_o \left[\frac{\partial v_i}{\partial t} S(\vec{x}, \vec{x}_i) + v_i \frac{\partial S(\vec{x}, \vec{x}_i)}{\partial t} \right]. \tag{3.28}$$

The notation j_e has been introduced simply to stress the fact that the parallel current is coming from the kinetic electrons and not from the solution of Ampere's law. The notation j_z will be used from now on to signify the solution of Ampere's law. When the hybrid model is working properly, these two variables should have the same value within a small numerical error. Now, with the use of the electron momentum equation $\frac{\partial v_i(\vec{x})}{\partial t} = -\frac{e}{m_e} E_z(\vec{x})$, the last expression becomes

$$\nabla^2 \vec{E}_z(\vec{x}) - \frac{\partial(\nabla \cdot \vec{E}(\vec{x}))}{\partial z} = -e\mu_o \sum_i \left[\frac{-e}{m_e} E_z(\vec{x}_i) S(\vec{x}, \vec{x}_i) + v_i \frac{\partial S(\vec{x}, \vec{x}_i)}{\partial t} \right]. \tag{3.29}$$

and using the continuity equation

$$\frac{dn}{dt} = \sum_i \frac{\partial S(\vec{x}, \vec{x}_i)}{\partial t} = \sum_i \left[\frac{\partial S(\vec{x}, \vec{x}_i)}{\partial t} + v_i \frac{\partial S(\vec{x}, \vec{x}_i)}{\partial z} \right] = 0 \tag{3.30}$$

the partial time derivative of the particle Shape function can be replaced with the advection term resulting with

$$\nabla^2 \vec{E}_z(\vec{x}) - \frac{\partial \nabla(\nabla \cdot \vec{E}(\vec{x}))}{\partial z} = \frac{\mu_o e^2}{m_e} \sum_i E_z(\vec{x}_i) S(\vec{x}, \vec{x}_i) + \mu_o e \sum_i v_i^2 \frac{\partial S(\vec{x}, \vec{x}_i)}{\partial z}. \tag{3.31}$$

Assuming $E_z(\vec{x}_i) \approx E_z(\vec{x})$, and that $\frac{\partial v_i^2}{\partial z} \approx 0$ (since the ambient distribution function is not dependent on z) we then have

$$\nabla^2 \vec{E}_z(\vec{x}) - \frac{\partial \nabla (\nabla \cdot \vec{E}(\vec{x}))}{\partial z} = \frac{\mu_o e^2}{m_e} E_z(\vec{x}) n_e(\vec{x}) + \mu_o e \frac{\partial}{\partial z} \sum v_i^2 S(\vec{x}, \vec{x_i}) \qquad (3.32)$$

where $n_e(\vec{x}) = \sum_i S(\vec{x}, \vec{x_i})$. Rearranging, and using the definition for the electron inertial length, we have

$$\nabla^2 E_z(\vec{x}) - \frac{1}{\lambda_e^2(\vec{x})} E_z(\vec{x}) = \frac{\partial (\nabla \cdot \vec{E})}{\partial z} + \mu_o e \frac{\partial}{\partial z} \sum v_i^2 S(\vec{x}, \vec{x_i}). \qquad (3.33)$$

Now for the FLR system, the parallel wavenumber is much smaller than the perpendicular values. The parallel electric field is also much smaller than E_x and E_y allowing the equation to be further simplified

$$\frac{\partial^2 E_z(\vec{x})}{\partial x^2} - \frac{1}{\lambda_e^2(\vec{x})} E_z(\vec{x}) = \frac{\partial (\nabla \cdot \vec{E}_\perp)}{\partial z} + \mu_o e \frac{\partial}{\partial z} \sum v_i^2 S(\vec{x}, \vec{x_i}). \qquad (3.34)$$

This derivation is similar to the approach used by Busnardo-Neto et al. (1977) and Okuda et al., (1979) for their work on magnetostatic particle codes. The expression is the same as used by Hui and Seyler (1992) for their hybrid model, although it was derived slightly differently there by utilizing the Generalized Ohm's Law.

If the second term on the right is neglected, this equation along with the 2D cold plasma equations are completely self consistent and the fields can be used as input for the guiding center equations for test particle simulations. However, although the second term on the right incorporates the effects of electron pressure on electric field generation, the equation as is, is not sufficient for a self consistent hybrid code. There needs to be a "correction field" for the charge separation induced between the fluid ions and kinetic electrons. This expression is determined as follows. Adding the continuity equations for the electrons and ions

$$\frac{\partial n_i}{\partial t} + \nabla \cdot (n_i \vec{v}_i) = 0 \qquad (3.35)$$

$$\frac{\partial n_e}{\partial t} + \nabla \cdot (n_e \vec{v}_e) = 0 \qquad (3.36)$$

yields

$$\frac{\partial (n_i - n_e)}{\partial t} + \nabla \cdot [(n_i v_i - n_e v_e)] = 0. \qquad (3.37)$$

Using Poisson's equation

$$\nabla \cdot E = \frac{e}{\epsilon_o} (n_i v_i - n_e v_e) \qquad (3.38)$$

and the definition of current

$$\vec{j} = e(n_i \vec{v}_i - n_e \vec{v}_e) \qquad (3.39)$$

41

yields the following relationship between the divergence of current and the divergence of electric field

$$\epsilon_o \frac{\partial}{\partial t}(\nabla \cdot \vec{E}) = -\nabla \cdot \vec{j}. \tag{3.40}$$

As noted earlier, $k_z \ll k_\perp$ and $E_\perp \gg E_z$, therefore it is possible to simplify this expression to

$$\epsilon_o \frac{\partial}{\partial t}(\nabla \cdot \vec{E}_{c_\perp}) = -\nabla \cdot \vec{j}, \tag{3.41}$$

where the notation E_c has been introduced to distinguish this field from the field calculated via the ideal MHD approximation $E_\perp = -\vec{u} \times \vec{B}_o$. The coupling for the correction field comes via the use of the electron current density in the divergence of the current density, such that

$$\nabla \cdot \vec{j} = \frac{\partial j_x}{\partial x} + k_y j_y + \frac{\partial j_e}{\partial z} \tag{3.42}$$

where j_x and j_y come from the fluid fields. In the MHD limit $\nabla \cdot \vec{J} = 0$ by default since $\nabla \cdot (\nabla \times \vec{b}) = 0$ and so there is no correction field.

It should be noted that this closure is somewhat different than that used by Hui and Seyler (1992) for their hybrid model used to examine electron acceleration due to SAW breaking. They coupled in the electron current density moment via an expression derived from the definition of ion polarization current.

3.4.6 Scaling of Electron number density

Now, obviously, it is not possible to use the real number of electrons for a system of magnetospheric scale. Therefore each simulation electron is actually representative of a "cloud" of electrons and the proper scaling is achieved via the ratio of the ambient fluid density and the unperturbed electron number density at t=0 (t_o). For example, the scaled electron current density is then

$$j_e(x, y, z, t) = j_e(x, z) cos(k_y y) = \frac{n_f(x, z)}{\sum_i S(\vec{x}, \vec{x}_i, t_o)} \sum_i v_i S(\vec{x}, \vec{x}_i). \tag{3.43}$$

Therefore, the electron current density that is input into the fluid model is given by

$$j_e(x, z) = \frac{1}{cos(k_y y)} \frac{n_f(x, z)}{\sum_i S(\vec{x}, \vec{x}_i, t_o)} \sum_i v_i S(\vec{x}, \vec{x}_i). \tag{3.44}$$

The second moment term in the equation for the parallel electric field is scaled in the same way and using the phase choices discussed earlier, the final form of this equation is

42

$$\frac{\partial^2 E_z(x,z,t)}{\partial x^2} - \frac{1}{\lambda_e^2(\vec{x})} E_z(x,z,t) \;=\; \frac{\partial(\nabla \cdot \vec{E}_\perp(x,z,t))}{\partial z}$$

$$+ \;\; \mu_o e \frac{n_f(x,z)}{\sum_i S(\vec{x},\vec{x}_i,t_o) cos(k_y y)} \frac{\partial}{\partial z} \sum v_i^2 S(\vec{x},\vec{x}_i).$$

3.4.7 Summary of Box Model Equations

The complete set of the hybrid MHD-kinetic box model equations is then given by the five cold plasma MHD equations

$$\frac{\partial u_x(x,z,t)}{\partial t} = \frac{B_o}{\mu_o \rho}\Big(\frac{\partial b_x(x,z,t)}{\partial z} - \frac{\partial b_z(x,z,t)}{\partial x}\Big)$$

$$\frac{\partial u_y(x,z,t)}{\partial t} = \frac{B_o}{\mu_o \rho}\Big(\frac{\partial b_y(x,z,t)}{\partial z} - k_y b_z(x,z,t)\Big)$$

$$\frac{\partial b_x(x,z,t)}{\partial t} = \frac{\partial E_y(x,z,t)}{\partial z} - \frac{\partial E_z(x,z,t)}{\partial y}$$

$$\frac{\partial b_y(x,z,t)}{\partial t} = \frac{\partial E_z(x,z,t)}{\partial x} - \frac{\partial E_x(x,z,t)}{\partial z}$$

$$\frac{\partial b_z(x,z,t)}{\partial t} = \frac{\partial E_x(x,z,t)}{\partial y} - \frac{\partial E_y(x,z,t)}{\partial x}$$

the three guiding center equations

$$\frac{\partial v_z(x,y,z,t)}{\partial t} = -eE_z(x,z,t)cos(k_y y) \tag{3.45}$$

$$\frac{\partial r_{gz}}{\partial t} = v_z \tag{3.46}$$

$$\frac{\partial r_{xz}}{\partial t} = \frac{1}{B_o}(v_z b_x(x,z,t) + e_y(x,z,t))sin(k_y y) \tag{3.47}$$

the ideal MHD approximation for the perpendicular electric fields, $\vec{E}_\perp = -\vec{u} \times \vec{B}_o$ and the equations for the parallel electric field

$$\frac{\partial^2 E_z(x,z,t)}{\partial x^2} - \frac{1}{\lambda_e^2(\vec{x})} E_z(x,z,t) \;=\; \frac{\partial(\nabla \cdot \vec{E}_\perp(x,z,t))}{\partial z}$$

$$+ \;\; \mu_o e \frac{n_f(x,z)}{\sum_i S(\vec{x},\vec{x}_i,t_o) cos(k_y y)} \frac{\partial}{\partial z} \sum v_i^2 S(\vec{x},\vec{x}_i)$$

and correction field

$$\epsilon_o \frac{\partial}{\partial t}(\nabla \cdot \vec{E}_{c_\perp}) = -\nabla \cdot \vec{j}, \tag{3.48}$$

As already stated, the model is designed to be used as either a test particle code or as a coupled model. For the test particle model, the pressure term in equation (3.48) is

43

neglected and the correction field E_c is not determined. For the hybrid model, $\nabla \cdot E_c$ is determined with a modified Euler scheme such that

$$\nabla \cdot E_{c\perp}^{n+1} = \nabla \cdot E_{c\perp}^n - dt\frac{1}{2\epsilon_o}[(\nabla \cdot \vec{j})_c + (\nabla \cdot \vec{j})_p] \tag{3.49}$$

where $(\nabla \cdot \vec{j})_c$ and $(\nabla \cdot \vec{j})_p$ are the divergences of current determined at the predictor and corrector steps respectively. This divergence is then used at the end of the predictor step to determine E_z for the next time step as follows

$$\nabla^2 E_z^{n+1}(\vec{x}) - \frac{1}{\lambda_e^2(\vec{x})}E_z^{n+1}(\vec{x}) = \frac{\partial(\nabla \cdot \vec{E}_\perp^{n+1} + \nabla \cdot E_{c\perp}^{n+1})}{\partial z} +$$

$$\mu_o e\frac{n_f(x,z)}{\sum_i S(\vec{x}, \vec{x}_i, t_o)cos(k_y y)}\frac{\partial}{\partial z}\sum v_i^2 S(\vec{x}, \vec{x}_i)$$

This equation is solved quite readily for E_z using a tridiagonal matrix solver.

3.5 Hybrid Kinetic-MHD Model in Generalized Curvilinear Coordinates

The dipolar model is designed exactly as the box model with the exception that now the mirror force term in the equation of motion for the electrons must be taken into account and this in turn introduces an extra term in the equation of the parallel electric field. Before introducing the model, a brief summary of generalized curvilinear coordinates and dipolar coordinates are presented.

3.5.1 Cold Plasma Equations in Generalized Curvilinear Coordinates

Generalized Curvilinear Coordinates expresses in one form any orthogonal coordinate system (such as cartesian, spherical or dipolar) where the individual coordinate system is identified through the form of the scale factors (sometimes denoted Lamé coefficients). For example, the the curl of the vector χ is written in Generalized Curvilinear Coordinates as

$$\nabla \times \vec{\chi} = \frac{1}{h_1 h_2 h_3}\sum_{l,m,n} h_l\hat{x}_l[\frac{\partial}{\partial x_m}(h_n\chi_n) - \frac{\partial}{\partial x_n}(h_m\chi_m)] \tag{3.50}$$

where $l, m, n = 1,2,3$ or $2,3,1$ or $3,1,2$ and h_1, h_2 and h_3 are the scale factors. This expression is coordinate system independent, but for cartesian coordinates for example, $h_1 = h_2 = h_3 = 1$. In general, the scale factors between the curvilinear coordinate system x_n and the cartesian coordinate system X_n are given by

$$h_n^2 = \sum_i(\frac{\partial X_i}{\partial x_n})^2. \tag{3.51}$$

44

Defining the ambient magnetic field to be in the x_1 direction such that $\vec{B} = B_o \widehat{x_1}$, and using the definition of the curl in curvilinear coordinates, the linear cold plasma equations in generalized curvilinear coordinates can be written as

$$\mu_o \rho \frac{\partial u_2}{\partial t} = \frac{B_o}{h_1 h_2} [\frac{\partial}{\partial x_1}(h_2 b_2) - \frac{\partial}{\partial x_2}(h_1 b_1)] \tag{3.52}$$

$$\mu_o \rho \frac{\partial u_3}{\partial t} = \frac{-B_o}{h_1 h_3} [\frac{\partial}{\partial x_3}(h_1 b_1) - \frac{\partial}{\partial x_1}(h_3 b_3)] \tag{3.53}$$

$$\frac{\partial b_1}{\partial t} = \frac{-1}{h_2 h_3} [\frac{\partial}{\partial x_2}(h_3 E_3) - \frac{\partial}{\partial x_3}(h_2 E_2)] \tag{3.54}$$

$$\frac{\partial b_2}{\partial t} = \frac{-1}{h_1 h_3} [\frac{\partial}{\partial x_3}(h_1 E_1) - \frac{\partial}{\partial x_1}(h_3 E_3)] \tag{3.55}$$

$$\frac{\partial b_3}{\partial t} = \frac{-1}{h_1 h_2} [\frac{\partial}{\partial x_1}(h_2 E_2) - \frac{\partial}{\partial x_2}(h_1 E_1)]. \tag{3.56}$$

3.5.2 Guiding Center Equations

In curvilinear coordinates coordinates, the velocity vector is given by

$$\frac{d\vec{v}}{dt} = h_1 \dot{x}_1 \hat{x}_1 + h_2 \dot{x}_2 \hat{x}_2 + h_3 \dot{x}_3 \hat{x}_3 \tag{3.57}$$

where the dot denotes the time derivative. Using this and the definition of the gradient in curvilinear coordinates

$$\nabla \psi = \sum \widehat{x}_n \frac{1}{h_n} \frac{\partial \psi}{\partial x_n} \tag{3.58}$$

it is straight forward to show that the guiding center equations are given by,

$$m_e \frac{\partial v_1}{\partial t} = -eE_1 - \mu_m \frac{1}{h_1} \frac{\partial B_o}{\partial x_1} \tag{3.59}$$

$$h_1 \dot{x}_1 = v_1 \tag{3.60}$$

$$h_2 \dot{x}_2 = v_1 \frac{b_2}{B_o} + \frac{E_3}{B_o}. \tag{3.61}$$

45

3.5.3 Parallel Electric Field

For a toroidal SAW with $k_3 = 0$ the only components of velocity and magnetic field are u_3 and B_3 respectively. The fact that $u_2 = 0$ implies $E_3 = 0$ as well. Starting with the expression for the field aligned current

$$\mu_o j_1 = \frac{1}{h_2 h_3} \frac{\partial}{\partial x_2}(h_3 B_3) \tag{3.62}$$

(where $B_2 = 0$ has been used) and taking the time derivative yields

$$\mu_o \frac{\partial j_1}{\partial t} = \frac{1}{h_2 h_3} \frac{\partial}{\partial x_2}(h_3 \frac{\partial B_3}{\partial t}). \tag{3.63}$$

Substituting for $\frac{\partial B_3}{\partial t}$, from Faraday's law

$$\mu_o \frac{\partial j_1}{\partial t} = -\frac{1}{h_2 h_3} \frac{\partial}{\partial x_2}(\frac{h_3}{h_1 h_2} \frac{\partial}{\partial x_1}(h_2 E_2)) + \frac{1}{h_2 h_3} \frac{\partial}{\partial x_2}(\frac{h_3}{h_1 h_2} \frac{\partial}{\partial x_2}(h_1 E_1)), \tag{3.64}$$

utilizing $j_1(\vec{x}) = j_e(\vec{x}) = -e \sum_i v_i S(\vec{x}, \vec{x}_i)$ and following the procedure outlined for the box model, yields the following expression for the parallel electric field E_1

$$
\begin{aligned}
\frac{1}{h_2 h_3} \frac{\partial}{\partial x_2}(\frac{h_3}{h_1 h_2} \frac{\partial}{\partial x_2}(h_1 E_1)) - \frac{1}{\lambda_e^2} E_1 \ =\ & \frac{1}{h_2 h_3} \frac{\partial}{\partial x_2}(\frac{h_3}{h_1 h_2} \frac{\partial}{\partial x_1}(h_2 E_2)) \\
& + \mu_o \frac{e}{m_e} \frac{1}{h_1} \frac{\partial B_o}{\partial x_1} \sum \mu_m S(\vec{x}, \vec{x}_i) \\
& + \frac{m u_o e}{h_1} \frac{\partial}{\partial x_1} \sum_i v_i^2 S(\vec{x}, \vec{x}_i).
\end{aligned}
$$

Defining $G = h_1 E_1$, and introducing the scaling factors as outlined for the box model, this expression can be written as

$$
\begin{aligned}
\frac{1}{h_2 h_3} \frac{\partial}{\partial x_2}(\frac{h_3}{h_1 h_2}(\frac{\partial G}{\partial x_2})) - \frac{G}{h_1 \lambda_e^2} \ =\ & \frac{1}{h_2 h_3} \frac{\partial}{\partial x_2}(\frac{h_3}{h_1 h_2} \frac{\partial}{\partial x_1}(h_2 E_2)) \\
& + \mu_o \frac{e}{m_e} \frac{1}{h_1} \frac{\partial B_o}{\partial x_1} \frac{n_f(x_2, x_1)}{\sum_i S(\vec{x}, \vec{x}_i, t_o)} \sum \mu_m S(\vec{x}, \vec{x}_i) \\
& + \frac{m u_o e}{h_1} \frac{\partial}{\partial x_1} \frac{n_f(x_2, x_1)}{\sum_i S(\vec{x}, \vec{x}_i, t_o)} \sum_i v_i^2 S(\vec{x}, \vec{x}_i)
\end{aligned} \tag{3.65}
$$

and G can be solved for using a tridiagonal solver routine and hence E_1 obtained. The correction field is obtained using the same formulation as presented for the box model. In curvilinear coordinates, the divergence of the current is given by

$$\nabla \cdot \vec{J} = \frac{1}{h_1 h_2 h_3}[\frac{\partial}{\partial x_1}(h_2 h_3 j_e) + \frac{\partial}{\partial x_2}(h_1 h_3 j_2) + \frac{\partial}{\partial x_3}(h_1 h_2 j_3)] \tag{3.66}$$

and with the assumption $k_\phi = 0$, the expression for E_c simplifies to
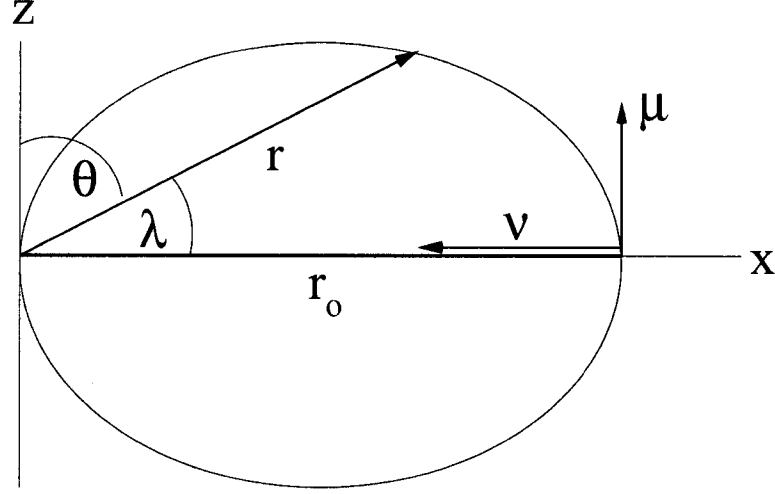
Figure 3.8: Comparison of Spherical and Dipolar Coordinates. ϕ is directed out of the page.

$$\epsilon_o \frac{\partial}{\partial t} \left(\frac{1}{h_1 h_2 h_3} \frac{\partial}{\partial x_2} [h_1 h_2 E_{2c}] \right) = -\nabla \cdot \vec{j}. \tag{3.67}$$

The method of solution for this equation and the introduction of the corrector field into the corrector step is similar to the procedure outlined for the box model. The one difference is that in the box model, it was sufficient to know $\nabla \cdot E_{c_\perp}$, but here it is necessary to spatially integrate to get E_{2c}. This is accomplished using a tridiagonal matrix solver.

3.6 Hybrid Model in Dipolar Coordinates

Dipolar coordinates are most commonly denoted by the variables μ, ν and ϕ (see figure 3.8). In the curvilinear cooridinates used thus far μ, ν and ϕ are defined by x_1, x_2 and x_3 respectively and are given in terms of spherical coordinates as the following

$$x_1 = \mu = \frac{\cos\theta}{r^2} \tag{3.68}$$

$$x_2 = \nu = \frac{\sin^2\theta}{r} \tag{3.69}$$

$$x_3 = \phi = \tan^{-1}\frac{y}{x}, \tag{3.70}$$

With these definitions, the dipolar metrics can be derived and are given in terms of spherical (and cartesian) coordinates by the following

$$h_1 = h_\mu = \frac{r^3}{(1 + 3\cos^2\theta)^{1/2}} = \frac{(x^2 + y^2 + z^2)^2}{(x^2 + y^2 + 4z^2)^{1/2}} \tag{3.71}$$

$$h_2 = h_\nu = \frac{r^2}{\sin\theta(1 + 3\cos^2\theta)^{1/2}} = \frac{(x^2 + y^2 + z^2)^2}{(x^2 + y^2)^{1/2}(x^2 + y^2 + 4z^2)^{1/2}} \tag{3.72}$$

47

$$h_\phi = r\sin\theta = \sqrt{x^2 + y^2}. \tag{3.73}$$

Unfortunately, the definition of the metrics in dipolar coordinates themselves is unknown. References as far back as Radoski (1967), always give the metrics in spherical coordinates and attempts by the author, among others, to derive them were unsuccessful. This introduced some unique problems in the implementation of the hybrid model in this dipolar system. These problems and the methods used to address them are summarized in the next two sections.

3.6.1 Single particle dynamics in a dipolar magnetic field

As noted above, the metrics in dipolar coordinates are known in terms of spherical coordinates rather than dipolar. This fact makes the solution of the guiding center equations in the dipolar coordinates very cumbersome because one must know the position simultaneously in both coordinate systems in order to both advance the equations of motion. Taking the definition for x_1 and x_2, it is straight forward to derive the equation

$$x_1^2 r^4 + r x_2 = 1 \tag{3.74}$$

the solution of which allows the conversion between the dipolar and spherical coordinates. The same method was applied by Voronkov et al. (1998) for a nonlinear resistive MHD model in dipolar coordinates (I Voronkov, private communication). Unfortunately, the inversion process is impossible if x_1, x_2 are determined simultaneously in the guiding center equations. However, the process can be made tractable for this problem by noting that the radial motion of the electron is negligible when compared to the field aligned motion (and the azimuthal motion is being neglected). This fact will be illustrated with the box model in Chapter 4. Therefore, if x_2 is specified and assumed not to change, the roots of the expression can be solved for to determine r and hence θ.

As a test, the guiding center equations were solved numerically in the absence of an electric field and the resulting bounce times and mirroring angles were compared with the analytical solution for the motion of an electron in a dipolar magnetic field (Parks, 1991). For a given equatorial pitch angle, α_0 the mirror angle is given by

$$cos^6\lambda_m - sin^2\alpha_o(1 + 3sin^2\lambda_m)^{1/2} = 0 \tag{3.75}$$

and the corresponding bounce time is given by the following

$$T_B = \int_0^{\lambda_m} \frac{r_o cos\lambda(1 + 3sin^2\lambda)^{1/2}d\lambda}{v[1 - sin^2\alpha_o\frac{(1+3sin^2\lambda)^{1/2}}{cos^6\lambda}]^{1/2}} = 4r_o\frac{I}{v} \tag{3.76}$$

where

48
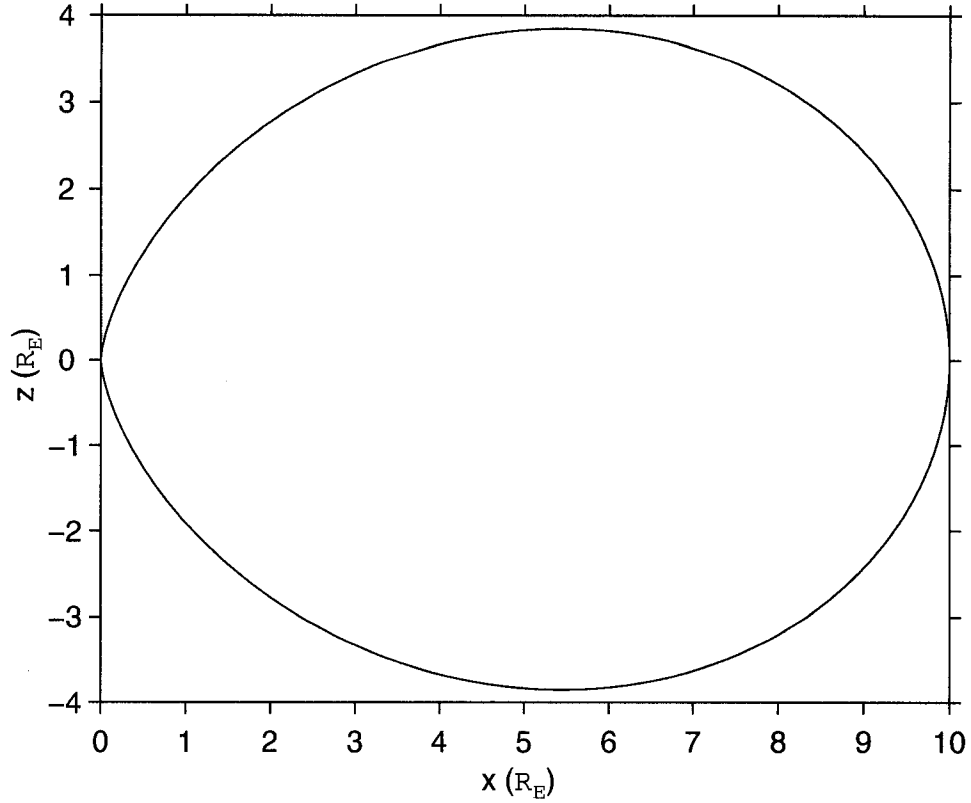
Figure 3.9: L=10 dipolar magnetic field line

$$I = \int_0^{\lambda_m} = \frac{cos\lambda(1 + 3sin^2\lambda)^{1/2}d\lambda}{[1 - sin^2\alpha_o \frac{(1+3sin^2\lambda)^{1/2}}{cos^6\lambda}]^{1/2}} \approx 1.3 - 0.56sin(\alpha_0). \tag{3.77}$$

The approximation is from Hamlin et al. (1961). Solutions for λ_m and T_b are given in Table (3.1) for 2 different equatorial pitch angles ($\alpha_o = \pi/3$ and $\alpha_o = \pi/6$) and two different kinetic energies, (T_e=100 eV and T_e=1keV). In all cases the electron is moving along the L=10 magnetic field line (figure (3.9)).

The results of the corresponding numerical solution of the guiding center equations is shown in figure (3.10). In all cases, the initial electron position is in the equatorial plane. As

case	α_o	T_e	λ_m	T_b
	(radians)	(eV)	(radians)	(s)
a)	$\pi/3$	100	0.255	35.1
b)	$\pi/3$	1000	0.255	11.1
c)	$\pi/6$	100	0.58	43.9
d)	$\pi/6$	1000	0.58	13.8

Table 3.1: Initial equatorial electron pitch angles and energies and the corresponding calculated bounce periods and mirror angles.

49
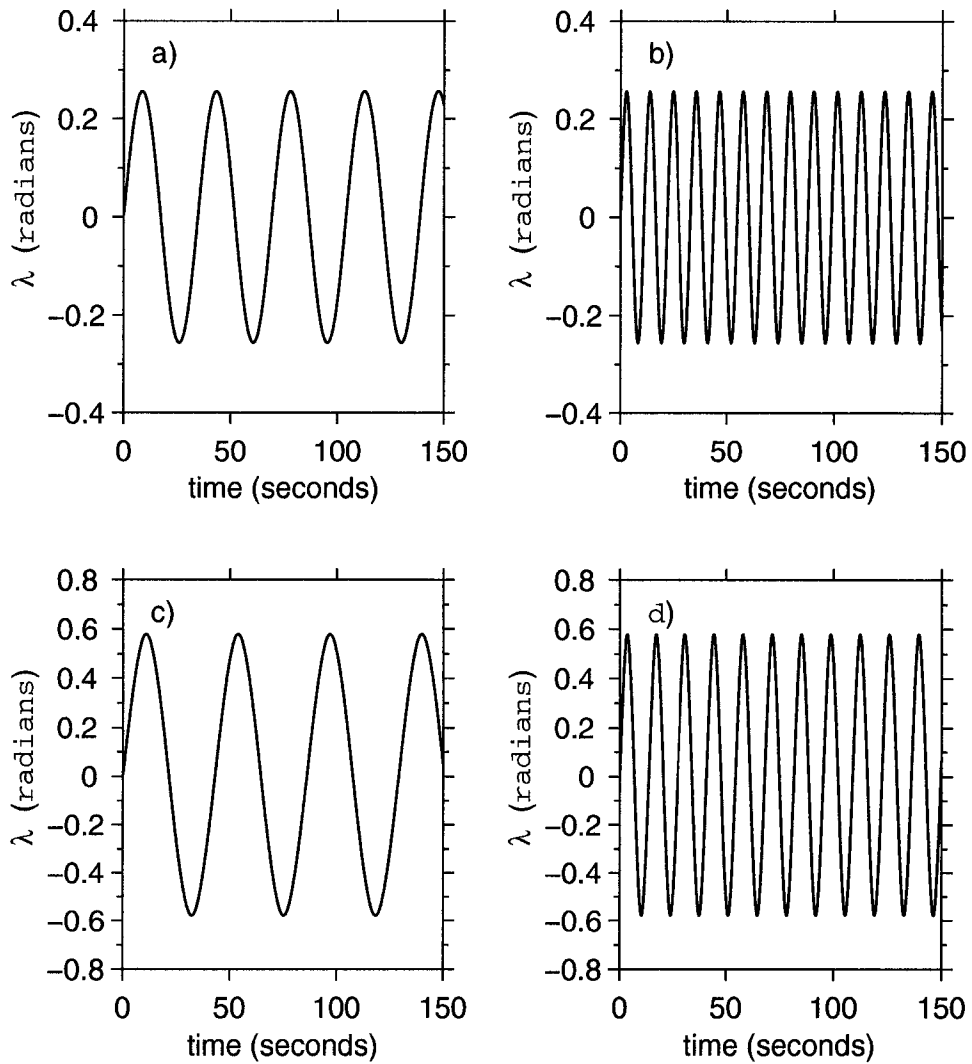
Figure 3.10: Graphs of λ vs time for an electron on the L=10 magnetic field line. The cases of each letter correspond to the parameters given in Table 3.1
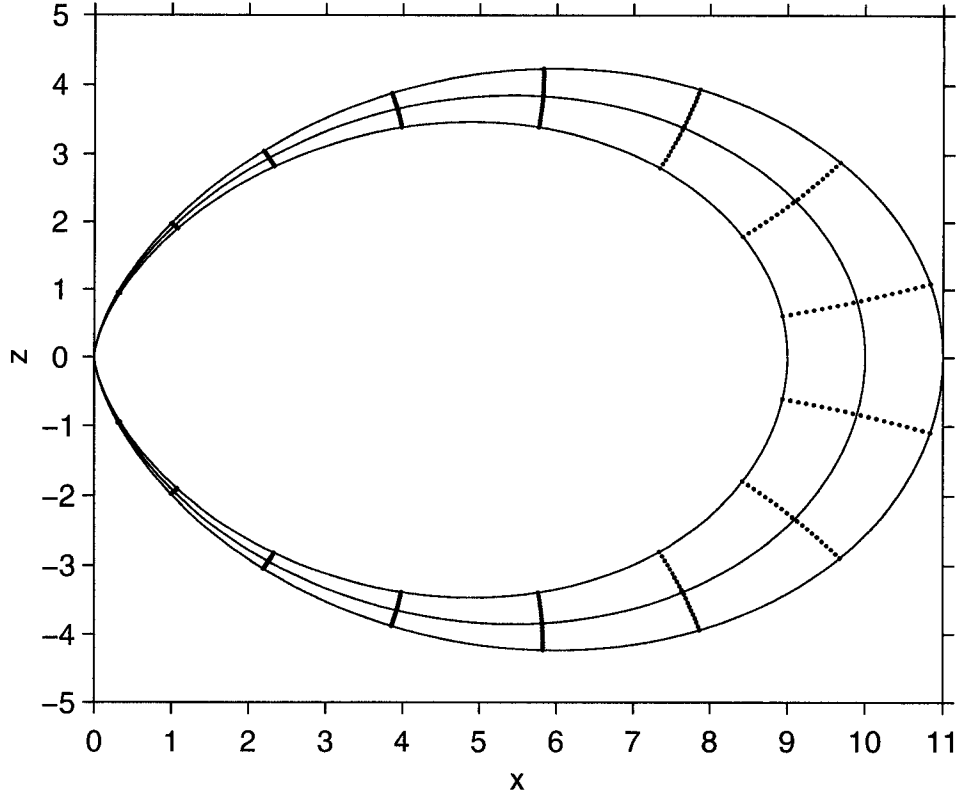
Figure 3.11: Sample numerical grid for $n_1 = 16$, $n_2 = 50$ with superimposed magnetic field lines for L=9,10 and 11.

is evident, the value of λ_m and T_B agrees well with the computed values. For the simulations presented here, the predictor-corrector routine was used again and the first order spatial derivatives were evaluated using the two point formula

$$(\frac{\partial f}{\partial x_2})_j = \frac{f_{j+1} - f_{j-1}}{x_{2_{j+1}} - x_{2_{j-1}}}. \tag{3.78}$$

As far as it is known, this is the first attempt at solving the guiding center equations in dipolar coordinates.

3.6.2 Numerical Notes

The time and spatial finite differencing of the fluid equations is the same as has already been mentioned. The primary difference between this test particle code and the version developed in Chapter 2, is that the grid is no longer rectangular. An example for the numerical grid utilized is illustrated in figure (3.11), where n_1 is the number of points in the direction along the ambient magnetic field and n_2 is the number of points perpendicular to it. For the purpose of clarity, the number of grid points shown in the diagram is significantly reduced from the number used in the simulations presented in Chapter 6.

As mentioned previously, it is unknown how to express the dipolar metrics in the dipolar

51
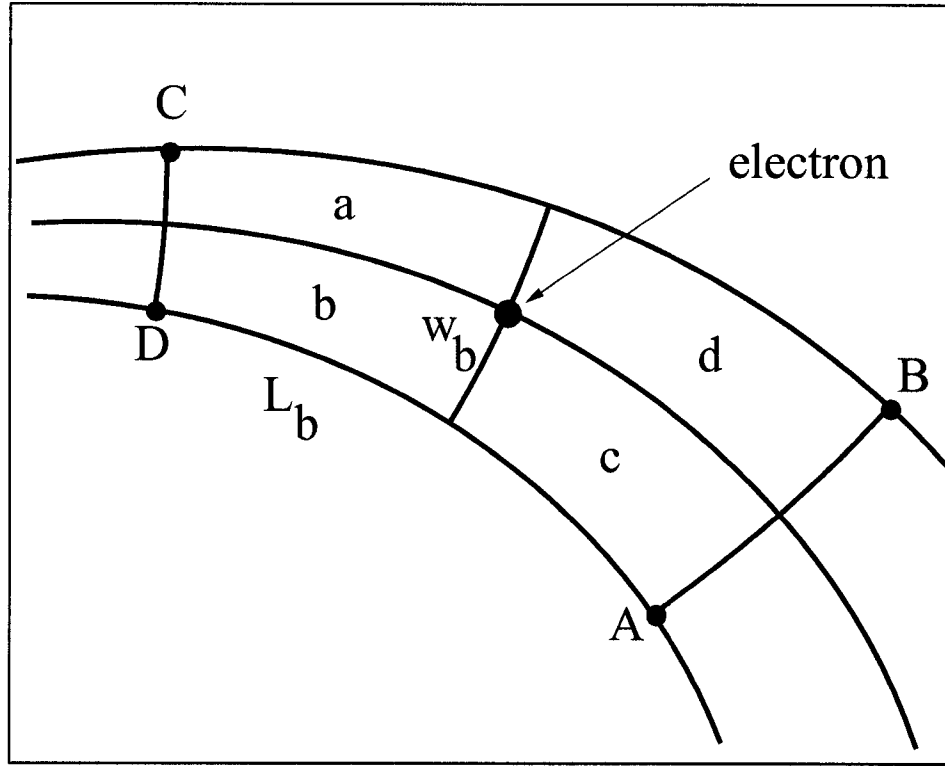
Figure 3.12: Example of bilinear interpolation scheme using parallelogram areas for weighting.

coordinates themselves and this consequently introduces the problem of how the define a unit area in dipolar coordinates. Therefore, it is necessary to use an approximation to interpolate the particle moments on to the grid and vice versa for the parallel electric field. For this, we again use the bilinear interpolation scheme and break up a grid cell into four subcells (refer to fig (3.11)). The subcell region "b" has a width and length of w_b and L_b respectively. If two points are closely spaced along an arc of constant x_1 (for example), the length of the line between the points (along the arc) can be approximated by $\overline{h_2^{12}}|\Delta x_2^{12}|$ where h_2^{12} is the average value of the metric h_2 between the two points and $|\Delta x_2^{12}| = |x_2^2 - x_2^1|$. A similar expression can be made for two points along an arc of constant x_2. Therefore as long as the grid is fine enough, we can define L_b and w_b respectively by

$$L_b \approx \frac{1}{2}(h_1^e + h_1^D)|(x_1^{DC} - x_1^e)|$$

$$w_b \approx \frac{1}{2}(h_2^D + h_2^e)|x_2^{DA} - x_2^e)|$$

where the superscript "e" indicates the electron position and x_1^{DC} is the value of x_1 along the arc between points D and C. The area of the subcell "b" can then be simply defined as $L_b w_b$.

In order to ascertain whether or not this first order approximation was sufficient, two

52
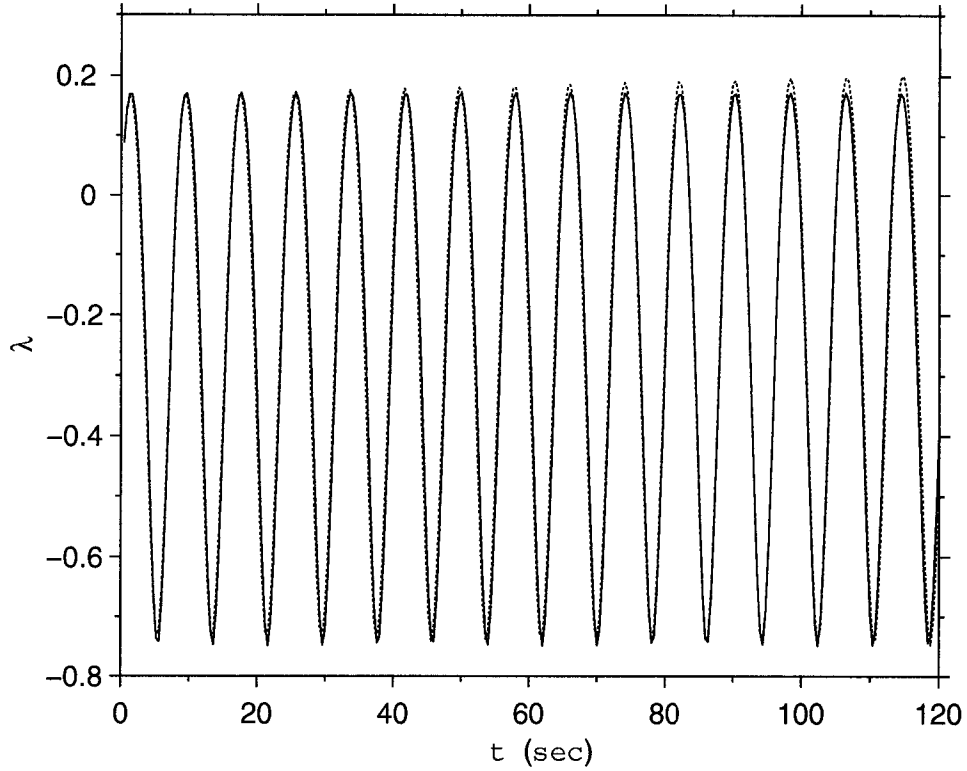
Figure 3.13: Particle angle λ as a function of time for exact calculation of the electric field at the particle position (solid line) and the interpolation of the field at the particle position (dashed line)

simulations were done of an electron in the dipolar magnetic field with a superimposed static electric field defined by

$$E_1 = E_o(sin(\theta))^{14} \tag{3.79}$$

where E_o is the amplitude of the electric field at the equator. In the first simulation, the electric field was calculated exactly at the particle position and in the second, the electric field was calculated at the grid points and interpolated to the particle position using the scheme outlined above. The electron energy was 1 keV, with an equatorial pitch angle of $\frac{\pi}{6}$ and $E_o = 1 \times 10^{-2}$ (nondimensional units). This electric field is much higher than would be generated in the hybrid simulations and is just used here as a test. The electron was started in the equatorial plane at the L=10 shell. Figure (3.13) illustrates the results of the simulations. The particle is trapped between the maximum electric field at the equator and the mirror force at the southern ionosphere. The simulation using the interpolation method (dashed line) is seen to gradually drift a little away from the simulation where the electric field was computed directly from the formula. However, as this is an extreme case, the drift is negligible. The simulation was done with 64 grid points in the field aligned direction and a time step of 0.008 seconds was used.

53

Chapter 4

Box Model Simulations

4.1 Preamble

In this chapter, simulations for the hybrid box model outlined in Chapter 3 are presented for both periodic and perfectly conducting boundary conditions in the z direction. The radial density and Alfvén profile are the same as outlined in Chapter 2. Both are constant in the z direction. The electrons are loaded according to this density profile and their velocities assigned via the Maxwellian profile as outlined in Chapter 3. All simulations are initialized using

$$u_y(t = 0) = Aexp(\frac{-(x - x_r)^2}{2w^2})sin(k_z z) \tag{4.1}$$

where $A = 0.05$ corresponds to a maximum shear velocity of 34.5 km/s and the position of the resonance is chosen to be $x_r = 0.5$ This function has the same radial profile as that used in Chapter 2. The dimensions of the box are $0 \leq x \leq 1.2R_E$ and $0 \leq z \leq 18R_E$ with n_x and n_z grid points in the x and z directions respectively. The azimuthal wave number is $k_y = 0.42/R_E$. Additional more specific points relating to the model are given in section (4.2)

The results for the periodic boundary conditions are presented in Section (4.3). The case of wave number $k_z = \frac{2\pi}{L_z}$ ($L_z = 18$ R_E) is considered in the limits $v_{th} \ll V_A$, $v_{th} \approx V_A$ and $v_{th} > V_A$. In the initial and last cases, the formation of inertial and kinetic Alfvén waves are demonstrated respectively. Landau damping of the Shear Alfvén wave is shown when $v_{th} \approx V_A$ or greater and the numerical damping rate is shown to be in good agreement with that predicted from the dispersion relation derived in Appendix A.

In section (4.4), the case of perfectly conducting boundary conditions is presented in the limit of $v_{th} \approx V_A$ for $k_z = \frac{\pi}{L_z}$ and $k_z = \frac{2\pi}{L_z}$. In both cases the SAW is again strongly Landau damped. The qualitative results for $k_z = \frac{2\pi}{L_z}$ are very similar to those from the section (4.2) thus showing that perfectly conducting boundaries do not alter the solution significantly from the periodic case.

54

4.2 Numerical Issues

As already indicated, most points relating to this model have been indicated in Chapters 2 and 3, but the more specific issues of filtering and boundary conditions are summarized in this section.

4.2.1 Filtering

In order to reduce the statistical noise, a 2D digital filter was applied to the current and pressure moments of the electron distribution function as well as the parallel electric field at both predictor and corrector steps. In one dimension, the filtered value is given by

$$F_i' = \frac{1}{4}F_{i-1} + \frac{1}{2}F_i + \frac{1}{4}F_{i+1}. \tag{4.2}$$

In the model, this was first applied in the x direction and then in the z direction. This is the lowest order digital filter (Birdsall and Langdon, 1991) and it has been used successfully in tradiational hybrid models with kinetic ions and fluid electrons (Winske et al., 1986). It has worked well in the context of this model except with regards to the parallel electric field as will be commented on later in the chapter.

4.2.2 Boundary Conditions

The boundary conditions for the fluid variables in the x direction are identical and implemented in the same way as already outlined in Chapter 2. The electrons on the other hand are loaded from $x = \frac{\Delta x}{2}$ to $x = L_x - \frac{\Delta x}{2}$. As will be shown, the radial motion of the electrons is minimal, but should they pass either boundary they are simply reintroduced at the same boundaries. This does not introduce any difficulties as there is no electron current into the x boundaries.

The handling of the boundary in the z direction is dependent on the specific boundary conditions. Periodic boundary conditions simply imply that $F_1 = F_n$. Therefore, in this case, the grid in the z direction goes from 0 to $L_z - \Delta z$ where Δz is the grid spacing but the electrons are free to move from 0 to L_z. The density and current moment contributions that would be assigned to a grid point at L_z are just contributed to the grid cell at $z = 0$ to enforce the periodic boundary conditions. Likewise for the fluid variables, this grid point is used in the calculation of derivatives at $z = L_z - \Delta_z$ (and vice-verse for z=0). Electrons that move past the $z = 0$ or $z = L_z$ boundaries are reintroduced at the opposite boundary with the same velocity.

In the case of the perfectly conducting boundary conditions, the treatment of the electrons at the boundaries is more complicated than in the periodic model and the method used will be summarized at the start of section (4.4).

55

4.3 Simulations with Periodic Boundary Conditions

This section summarizes the simulations of the hybrid box model with field aligned periodic boundary conditions. Before proceeding to the hybrid simulations though, the new electric field formulation outlined in Chapter 3 will be contrasted with the Generalized Ohm's Law, the solution of the 2D fluid model will be contrasted with the 1D results from Chapter 2 and the test particle and hybrid models will be compared for an initial electron δ-function distribution.

Whether in the fluid or hybrid limits though, all the following simulations were done with $n_x = 200$, $n_z = 25$ and 70000 time steps for 10 Alfvén wave periods. Since this is the 2D analogue of the simulations presented in Chapter 2, the frequency and period of the resonance are again, $0.0755\ s^{-1}$ and 83.2 seconds respectively.

4.3.1 Comparison of Electric Field Formulations

Using the same method as for Chapter 2, a version of the 2D fluid model was written incorporating the Generalized Ohm's law formulation for the parallel electric field. The output of this model was compared with the output of the fluid model with the electric field formulation derived in Chapter 3 given, without the pressure moment, by

$$\frac{\partial^2 E_z(\vec{x})}{\partial x^2} - \frac{1}{\lambda_e^2(\vec{x})} E_z(\vec{x}) = \frac{\partial(\nabla \cdot \vec{E_\perp})}{\partial z} + \mu_o e \frac{\partial}{\partial z} \sum v_i^2 S(\vec{x}, \vec{x_i}). \tag{4.3}$$

For both simulations, $n_x = 128$, $n_z = 16$ and 200,000 time steps were used for ten Alfvén periods. A slice of the parallel electric field taken in both cases at z=12.35 for $t = 3\ T_A$ is displayed in figure (4.1). The resulting electric fields are very close illustrating the basic equivalence of these two formulations. The advantage of the latter, even in the fluid limit, is that it is very stable for significantly larger time steps.

4.3.2 Comparison of 1D and 2D models

Although the physical systems for the 1 and 2D models do share exactly the same boundary conditions in z, it is interesting to compare the two models. If $k_z = \frac{2\pi}{18}$ is used in the 1 dimensional model, it corresponds to the initial condition specified here. Figure (4.2) compares the amplitude of the first order mode for u_y at $t = 5T_A$ with the values from the 1D model for the same time. In both simulations $\lambda_e = 0$. As would be expected, in the cold plasma limit and with a constant field aligned density, the 2D and 1D solutions are in good agreement.

4.3.3 Single Particle Dynamics

Figure (4.3) illustrates the radial and field aligned motion of the guiding center of an electron started at (x, z)=(0.5, 9) with an initial velocity $v_{gz} = 0$. As is evident, the radial motion of the electron is negligible relative to the field aligned motion which is consistent with the

56
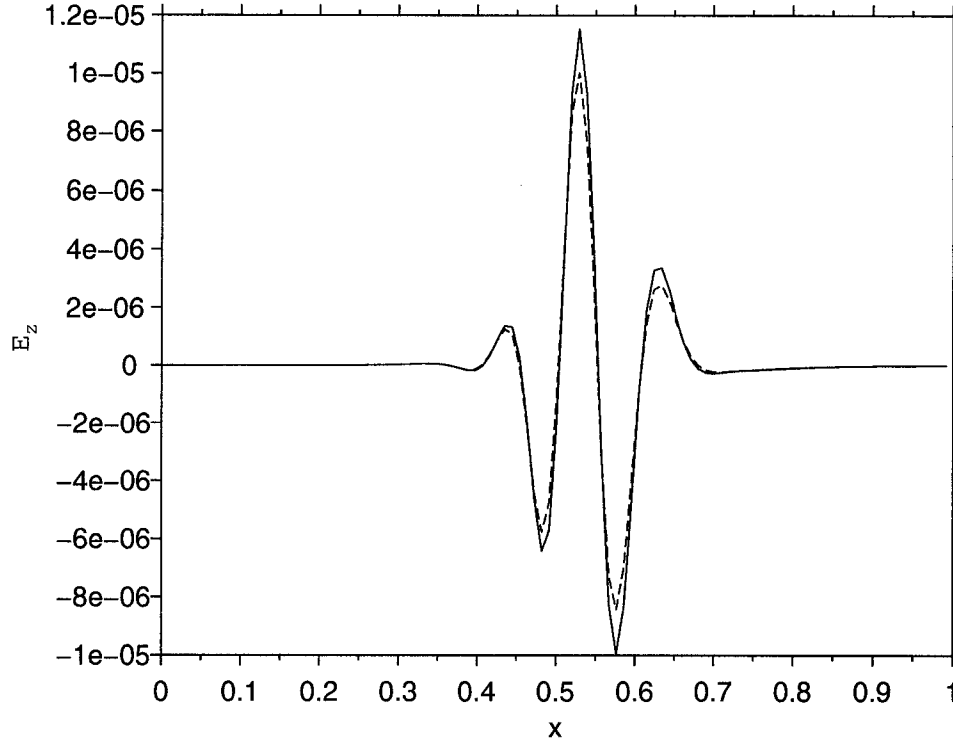
Figure 4.1: Comparison of E_z from the Generalized Ohm's Law (solid line) and from expression (4.3) (dashed line) at $t = 3\ T_A$. Slice at z=12.35

current picture within a FLR as outlined in Chapter 1. The shift of the electron position at $t \approx 85$ is the electron passing through one boundary and re-entering at the other (and vice-verse).

4.3.4 Comparison of Test Particle and Hybrid Model results

This section presents calculations using both the test particle model and coupled model for an initial δ function distribution of electrons. The top panel of figure (4.4) displays the test particle results for the current density while the bottom panel displays the hybrid model results at $t = 2\ T_A$. In both cases, j_z is the parallel current density calculated from Ampere's law, while j_e is the electron current density as interpolated to the grid. As is evident, j_z and j_e diverge very quickly in the test particle model, but stay very nicely in line in the hybrid model case. This trend continues more dramatically as time goes on. Therefore with no feedback of the electrons on the fluid, the test particle approach is valid for only a very short time.

4.3.5 Comparison of Hybrid model simulations for different initial distributions.

For the system under consideration here, the phase velocity of the standing SAW is $v_{ph} = \frac{\omega}{k_z} = \pm 2$. Therefore, it is expected that for a sufficiently wide distribution function, Landau

57
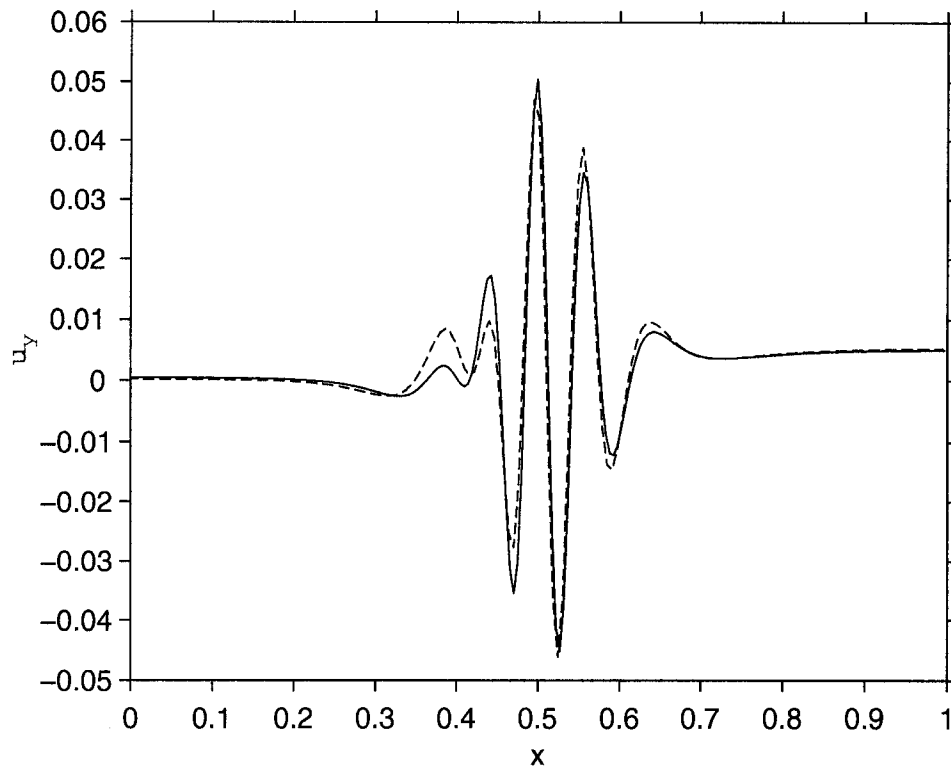
Figure 4.2: Amplitude of the first order mode for u_y from the 2D periodic fluid model (solid line) compared to output of the 1D model (dashed line) at $t = 5T_A$. Both cases are for $\lambda_e = 0$.
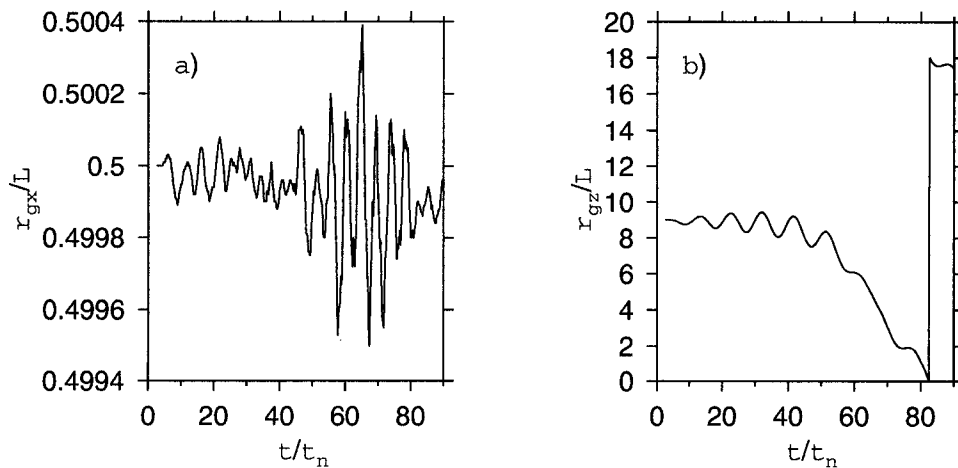
Figure 4.3: a) The radial motion of an electron guiding center in the standing SAW system. b) The field aligned motion.

58
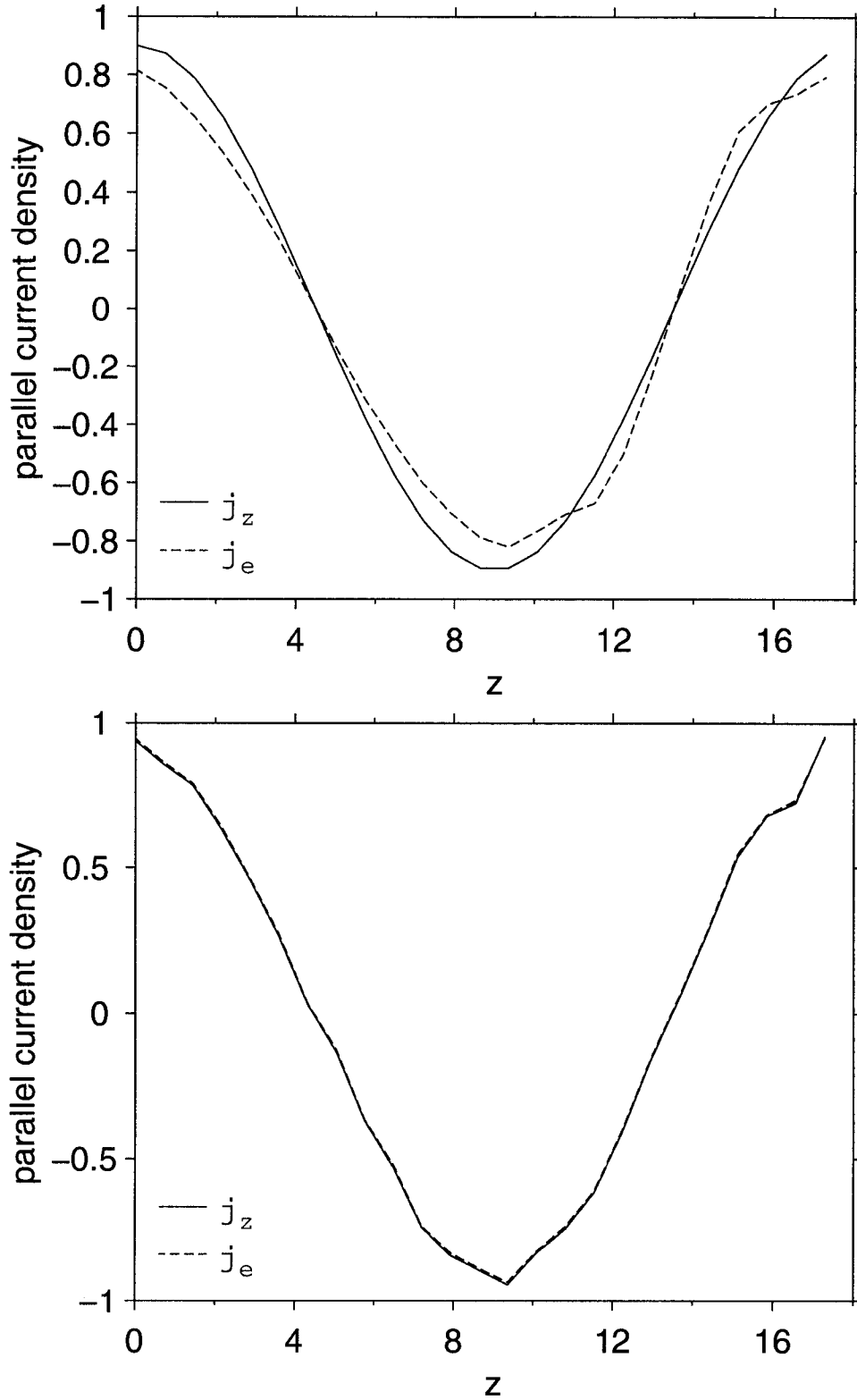
Figure 4.4: Comparison of kinetic electron current j_e and the Ampere's law current j_z from the test particle model at $t = 2$ T_A (top) and the hybrid model at $t = 6$ T_A . Slice at x=0.597.

59

damping effects should become evident. This would manifest itself as a flattening of the distribution around $v_z = \pm 2$ as electrons with velocity a little less than the phase velocity of the SAW are accelerated to a little beyond v_{ph}. The gradual loss of energy from the SAW to the electrons will be evident as a gradual decrease in amplitude of the SAW. To test this, simulations were conducted with 4 different initial distribution functions, a δ function distribution (v_{th}=0) and three Maxwellian distributions (v_{th}=0.71, 1.41, 4.24). All hybrid model simulations used one million particles ($n_{p_x} = 1000, n_{z_p} = 1000$) except in the $v_{th} = 4.24$ case where two million particles ($n_{p_x} = 1000, n_{z_p} = 2000$) were used. The illustrated distribution functions are average distribution functions compiled using electrons close to the resonance, ($0.5 \leq x \leq 0.65$) and anywhere in the z plane. One hundred velocity bins are used in the compilation.

For the case of the cold plasma limit, figure (4.5) illustrates the azimuthal velocity at $t = 4\ T_A$ and $t = 8\ T_A$ for fluid model and the hybrid model using the initial δ-function distribution and $v_{th} = 0.71$ distribution. As would be expected, the hybrid description and the cold plasma MHD fluid description diverge little. The formation of an inertial SAW propagating to the right (the direction of increasing Alfvén wave speed) is evident.

The case of $v_{th} \approx V_A$ is illustrated in Figure (4.6) where the azimuthal velocity for the hybrid model using $v_{th} = 1.41$ for $t = 4\ T_A$ and $t = 7\ T_A$ is displayed along with the MHD results. The gradual Landau damping of the SAW as a function of time is clearly evident. The numerical damping rate measured from this calculation will be compared with the theoretical value determined from the dispersion relation in a later subsection.

The final example of $v_{th} > V_A$ is illustrated in figure (4.7) where the evolution of the azimuthal velocity at $t = 4\ T_A$ and $t = 8\ T_A$. The resonance in the hybrid model is seen to maintain its position while it propagates as an inertial wave pulse in the cold plasma MHD limit. This increase in temperature implies that the system is entering into the kinetic Alfvén wave regime and close examination indicates a slight propagation in the direction of decreasing Alfvén wave speed. The wave is strongly damped though and is nonexistent by $t = 6\ T_A$.

The evolution of the corresponding electron distribution functions are illustrated in figure (4.8). The top panel illustrates the $v_{th} = 0.71$ distribution case and it is evident that the distribution function is heated a little during the length of the simulation, but only changes marginally. In the middle panel the $v_{th} = 1.41$ case is presented. The Maxwellian is being modified at the $v_z = \pm 2$, which as mentioned previously is the classic plateauing due to Landau trapping effects. The warmest case, $v_{th} = 4.24$ is highlighted in the bottom panel. The distribution function is not as strongly modified as in the $v_{th} = 1.41$ case, but there is evidence of some trapping around $v_z \approx v_{ph}$. The damping is actually stronger, as is evident from the figure (4.7), because the slope of the distribution function at the resonance position is steeper than for $v_{th} = 1.41$. The lack of strong modification of the distribution function is probably due to the larger number of electrons around the resonance position

60
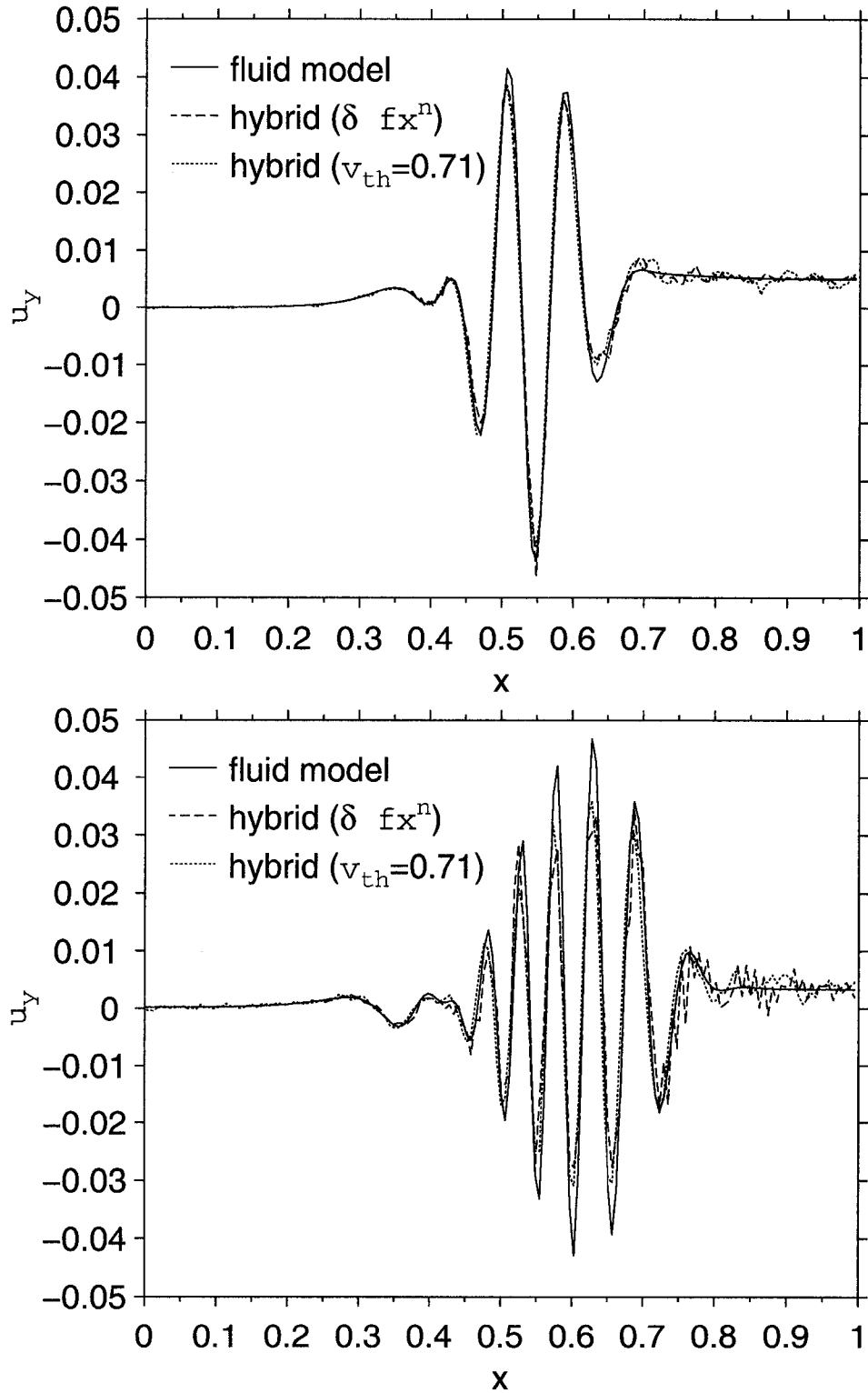
Figure 4.5: Top: Comparison of azimuthal velocity at t=$4T_A$ from the fluid model (solid line) and the hybrid model for the for the initial δ-function electron distribution (dashed line) and v_{th} = 0.71 initial electron distribution function (dotted line). Slice at z=3.6. Bottom: same at $t = 8$ T_A.

61
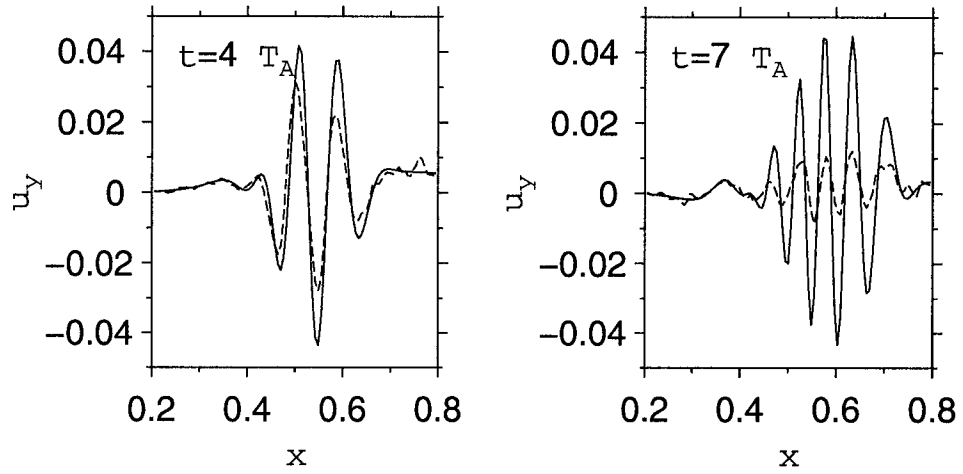
Figure 4.6: Comparison of azimuthal velocity from the fluid model (solid line) and the hybrid model with $v_{th} = 1.41$ initial electron distribution function (dashed line). Slice at z=3.6.
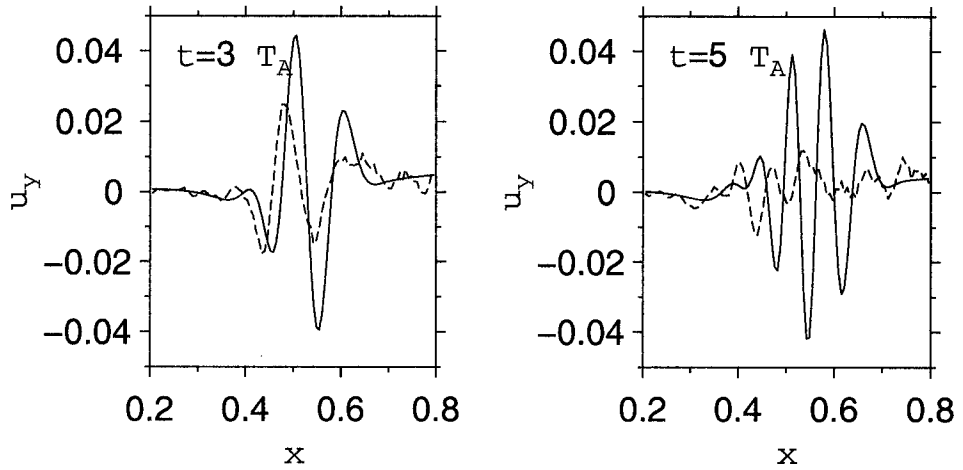
Figure 4.7: Comparison of azimuthal velocity from fluid model (solid line) and hybrid model with $v_{th} = 4.24$ (dashed line). Slice at z=3.6.

62

than in previous case.

In order to show that the coupling holds properly in these higher temperature cases, figure (4.9) illustrates the comparison of j_e and j_z for $v_{th} = 4.24$. The two currents still agree with each other to a high degree of accuracy in spite of the evident noise. This noise can be further reduced with increased particle number.

4.3.6 Significance of Pressure Term

As was indicated in Chapter 3, the formulation for the parallel electric field includes a term for the electron pressure. In order to ascertain how important the contribution of this term was for the plasma parameters considered here, the $v_{th} = 1.41$ case was run again, but with the pressure moment term turned off in the expression for the parallel electric field. Figure (4.10) illustrates a comparison of the azimuthal velocity from the fluid code (solid line) and the hybrid code with (dashed line) and without the pressure term (dotted line). The negligible difference between the two hybrid model runs illustrates, that for the parameters considered here, electric field contributions due to electron pressure are negligible and most of the important physics comes via the electric field generated to enforce quasineutrality.

4.3.7 Effects of particle number

An important consideration in any statistical model is how the number of simulation electrons effects the results. It is necessary to have a sufficient number to adequately represent the system as well as keep noise issues to a minimum. However, as indicated previously, the number of simulation electrons are scaled to a realistic value and so after a point, the general results should be insensitive the simulation electron number. In order to test this, the $v_{th} = 1.41$ simulation was redone with two million simulation electrons. The current moment results in both cases (along with the MHD results) are illustrated in figure (4.11). As is evident, there is little quantitatively significant difference until well into the run and the evolution of the system is the same in both cases. Therefore the hybrid code results are robust with respect to particle number.

4.3.8 Parallel Electric Field

As alluded to earlier, the parallel electric field is typically too noisy to be visible, even with the smoothing algorithm used. However, the field can be seen with the application of a post-simulation spectral filter using the hyper-gaussian function to filter out higher order spectral modes. The function has the form

$$e^{-(\frac{i}{n})^{20}} \tag{4.4}$$

where i is the spectral mode number and n is a parameter to be specified. The filtering, in each direction, is accomplished by first doing the forward fourier transform, multiplying

63
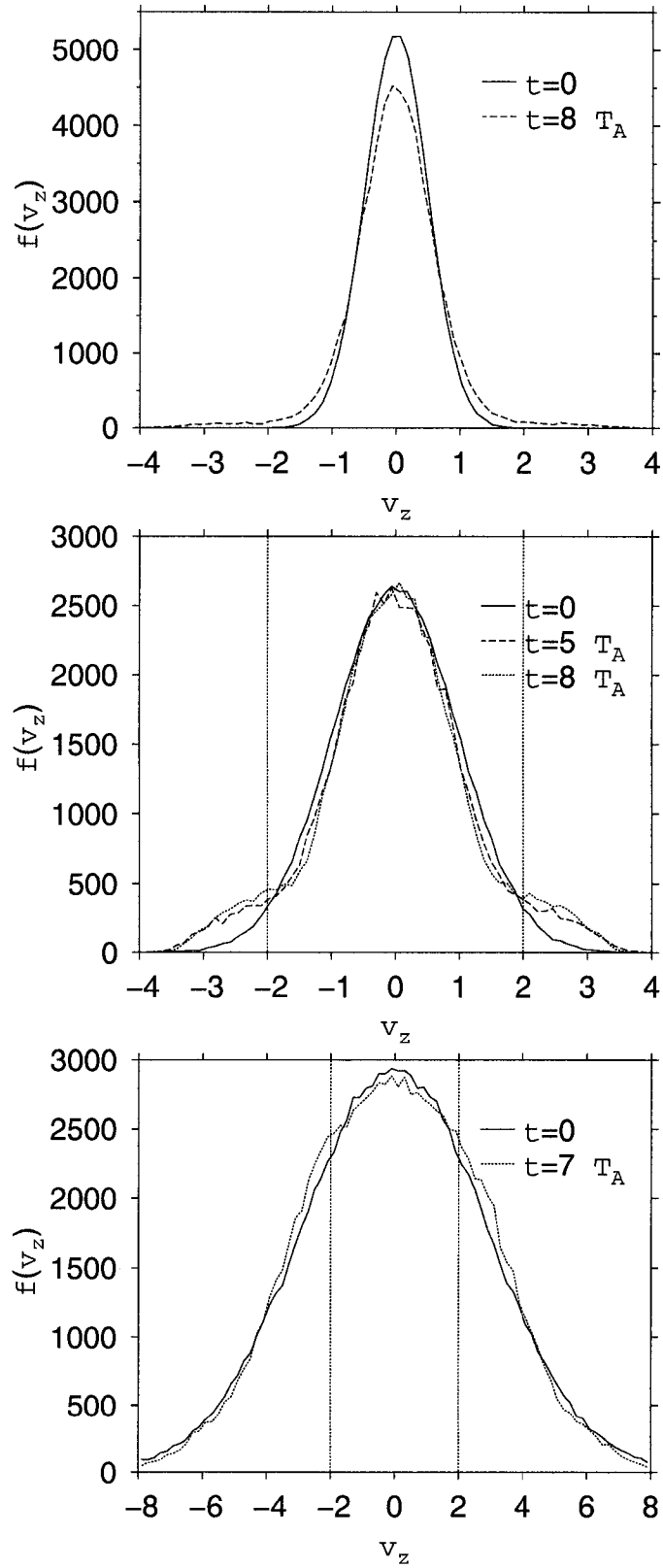
Figure 4.8: Distribution function evolution. Top: Case of $v_{th} = 0.71$. Middle: Case of $v_{th} = 1.41$. Bottom: Case of $v_{th} = 4.24$.

64
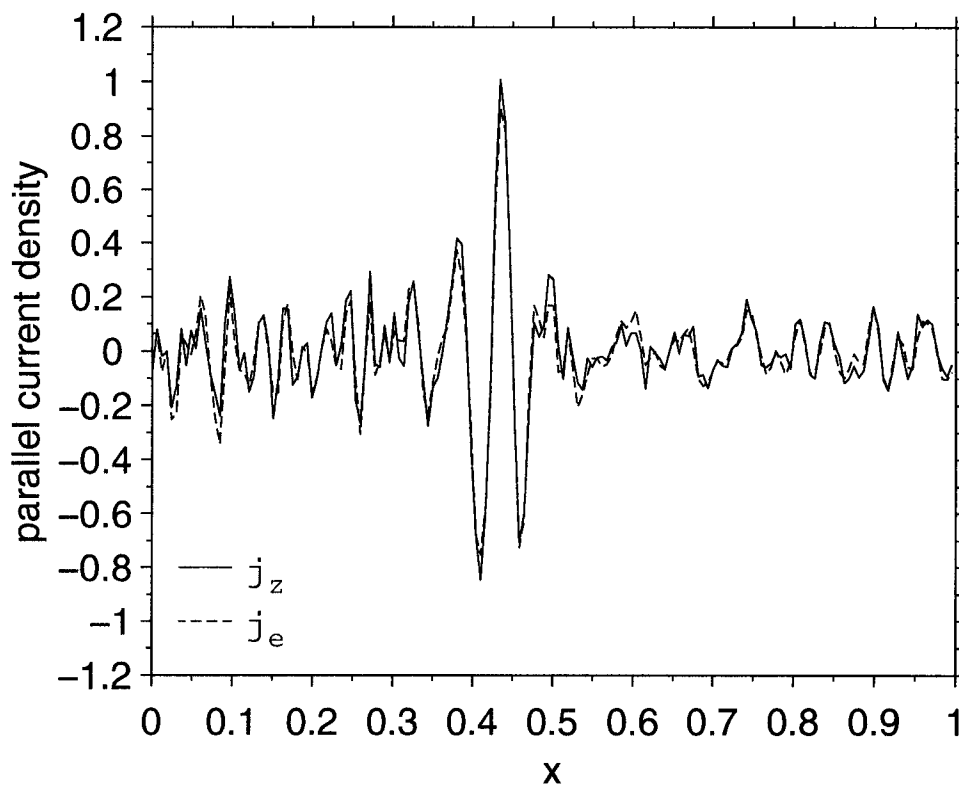
Figure 4.9: Comparison of kinetic parallel electron current j_e (dashed line) and the solution of Ampere's Law j_z in the hybrid code for $v_{th} = 4.24$. Slice at z=7.92.

65
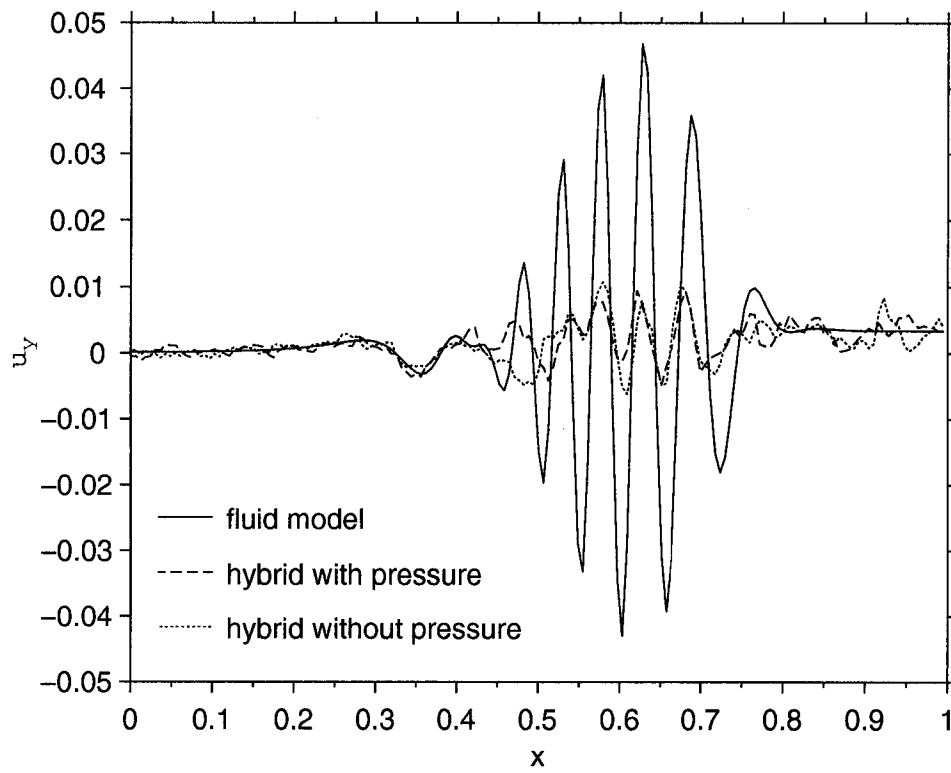
Figure 4.10: Comparison of azimuthal velocity from the fluid code (solid line) and hybrid code with (dashed line) and without pressure term (dotted line) at t=8.0 T_A. Slice at z=3.6.

66
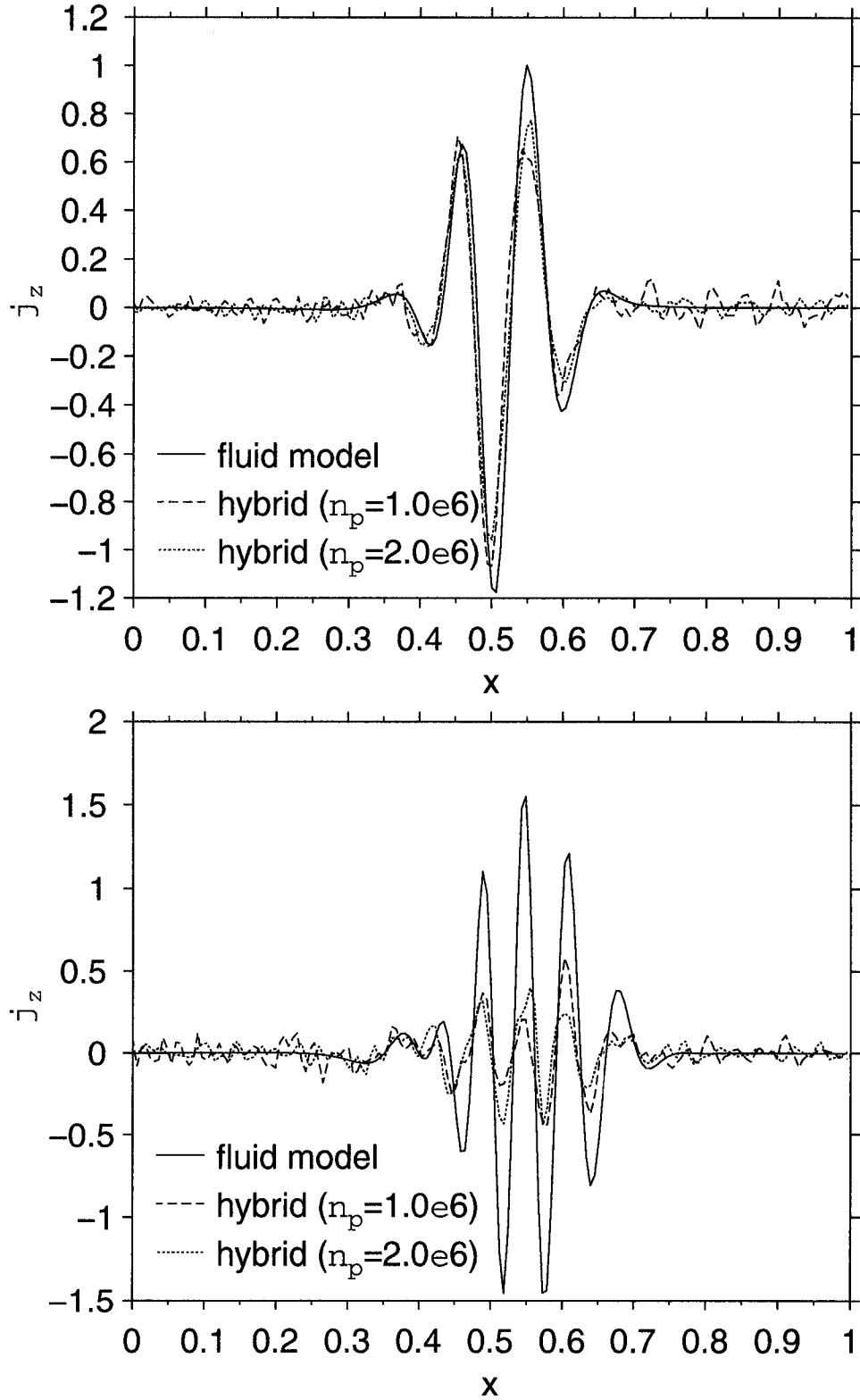
Figure 4.11: Top: Comparison of the azimuthal velocity in the hybrid model using the $v_{th} = 1.41$ initial electron distribution function with $n_p = 1 \times 10^6$ (solid line) and $n_p = 2 \times 10^6$ (dashed line) at $t = 3\ T_A$. Bottom: Same at $t = 7\ T_A$. Slice at z=7.92.

67

the transform by the filtering function and then doing the inverse transform. This is done first in the x direction and then in the z direction, but the order of the application is not significant. In the x direction, 200 grid points were used and so a value of n=80 was chosen. This filters out only the highest of the 100 possible modes as these are the main source of numerical grid scale noise.

In the z direction on the other hand, a value of n=4 was used. For any higher value, there was still too much noise to clearly see the signal in the higher temperature cases. This is not a problem though since the simulation is for the first order mode $k_z = \frac{2\pi}{L_z}$ (i=2) and most of the initial physical information is contained here. Also, although the Landau damping seems to result in some slightly higher mode structure, the application of this filter to the current does not significantly alter the profile. Therefore, it is safe to assume that applying this filter to the parallel electric field is not leading to a loss of physical information.

The unfiltered fluid parallel electric fields and filtered values for the hybrid code using $v_{th} = 0.71$ and $v_{th} = 1.41$ are displayed in Fig. (4.12). As expected, the parallel electric field in the $v_{th} = 0.71$ case does not diverge significantly from the fluid model, but the damping in the $v_{th} = 1.41$ case is clearly visible. Therefore, even though the field is not visible directly in the simulations, it is behaving as expected and consistent with the other model variables. The parallel electric field in the $v_{th} = 4.24$ case is not visible even with the filtering, but this can be rectified by increasing the particle number.

The fact that the model works so well in spite of the fact that the parallel electric field signature is drowned in noise implies that the electrons are not strongly effected by the high frequency noise, but are mainly responding to the low frequency parallel electric field signature. It is believed that signal to noise ratio is so much worse than for all other variables because the determination of E_z involves taking the divergence and then integration of already somewhat noisy quantities (i.e. j_e).

4.3.9 Density Fluctuations

As was mentioned earlier, the electron density distribution has the same profile as the specified fluid density. This is evident in the top panel of figure (4.13) which illustrates the unscaled electron number density at $t = 3\ T_A$ for hybrid model using one million particles. Superimposed on the ambient density is the perturbation due to the standing Shear Alfvén wave. The bottom panel of the same figure illustrates slices of N_e along $z = 3.6$ at the same time for both the one million and two million particle simulations. The result for the former case has been multiplied by two and lies very close to the result for the latter case. This illustrates that the ratio of the fluctuation relative to the ambient background is relatively independent of the number of simulation electrons. The magnitude of the background density is evident from the slice at $t = 0.1\ T_A$.

68
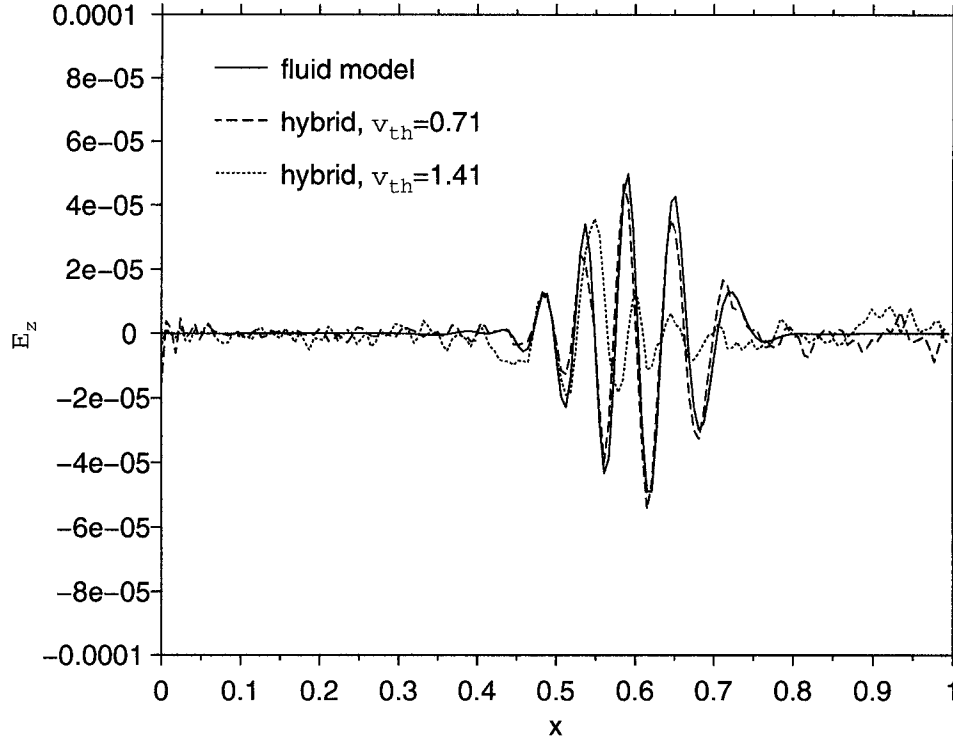
Figure 4.12: Parallel electric field after the application of the post-simulation spectral filter at $t = 7\ T_A$. Slice at $z = 7.92$. The fluid model result is unfiltered.

4.3.10 Damping rate comparison

Using the drift kinetic equation, the cold plasma equations and defining a dependence of $e^{i(k_x x + k_y y + k_z z) - i\omega t}$ it is straight forward to derive a dispersion relation for the periodic system (see Appendix 1) as

$$\omega^2 = k_z^2 V_A^2 (1 + \frac{ik_x^2}{\omega\mu_o \frac{-ie^2 n\omega}{k_z^2 k_B T}(1 + \epsilon Z(\epsilon))})^{-1}.\qquad(4.5)$$

where Z is the plasma dispersion function. This can be solved numerically for the model parameters to yield a damping rate that can be compared to the one measured numerically.

In figure (4.14) is shown a plot of the log of average value of the current density j_z between x=0.5 and x=0.6 (for a slice along z=7.92) as a function of time between 300 and 800 seconds $(0.36T_A \le t \le 0.96T_A)$ along with a best fit line. The initial 300 seconds were truncated as the average current density was increasing with time for this period. The regression statistics of the line are then

$$y = (-0.0042 \pm 0.0005)t + 0.5 \pm 0.3\qquad(4.6)$$

of which the slope gives the damping rate of the resonance $\gamma = -0.0042 \pm 0.0005 s^{-1}$. This result can be compared with the values obtained from the imaginary part of the kinetic

69

'd_dn030' ———
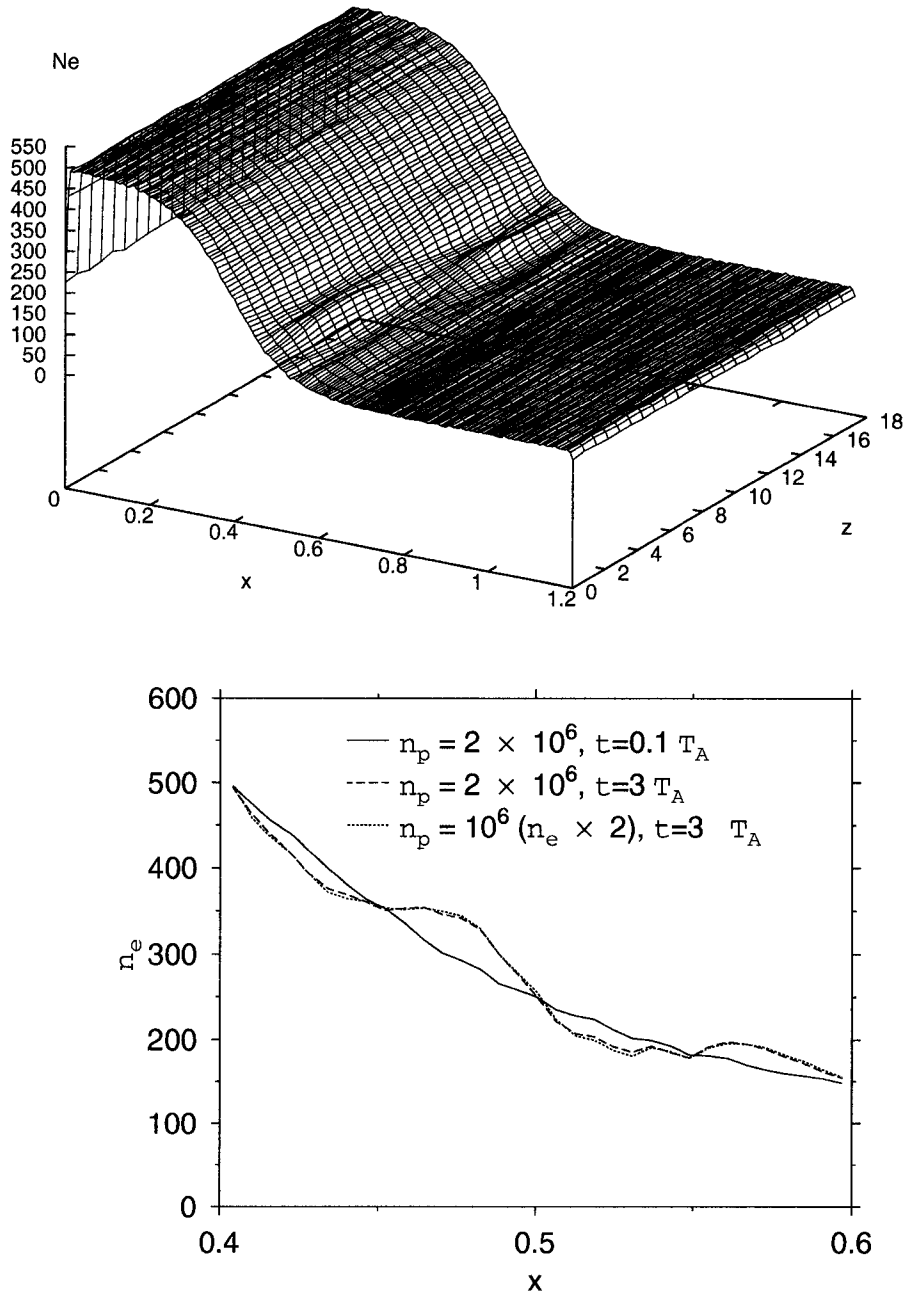
Figure 4.13: Top: Unscaled electron number density from the hybrid model with $v_{th} = 1.41$ and $n_p = 1 \times 10^6$ at $t = 3\ T_A$. Bottom: Slices of the unscaled electron number density at z=3.6 for $t = 3\ T_A$ with $n_p = 1 \times 10^6$ (dashed line) and $n_p = 2 \times 10^6$ (dotted line). The ambient density profile is indicated by the solid line for $t = 0.1\ T_A$.

70
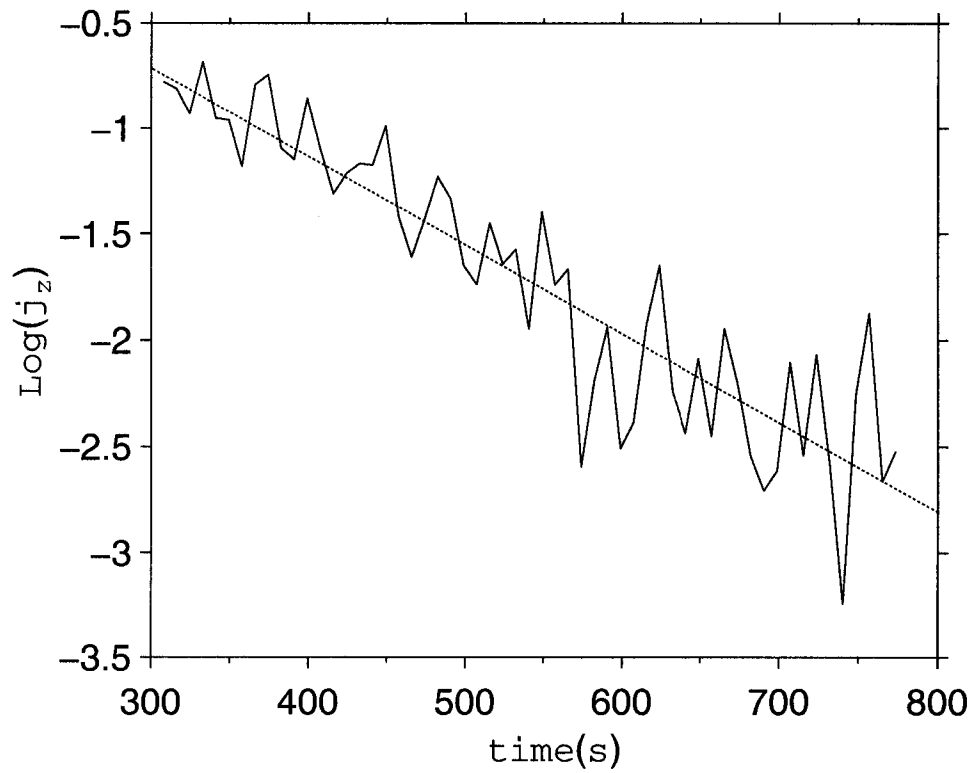
Figure 4.14: Log of the average value of the parallel current density between $x = 0.5$ and $x = 0.6$ vs time for a slice along $z = 7.92$ (solid line) and best fit line (dashed line). Data for $t < 300$ seconds is truncated.

71

dispersion relation. This is only a rough comparison as the Alfvén velocity profile changes from 2 to 2.6 in the range considered and the resonance narrows from about $k_x \approx \frac{2\pi}{0.1 R_e} \rightarrow \frac{2\pi}{0.05 R_e}$ as the resonance evolves. Assuming the local Alvén wave speed and electron inertial length at $x = x_r$ damping rates for the $v_{th} = 1.41$ distribution function are calculated to be 0.0016 s^{-1} and 0.0058 s^{-1} for $k_x = \frac{2\pi}{0.1 R_e}$ and $k_x = \frac{2\pi}{0.05 R_e}$ respectively. Thus the numerical damping rates and that obtained from the kinetic dispersion relation are in the same range.

4.4 Simulations with Conducting Boundary Conditions

In this section, simulations using the hybrid model with perfectly conducting boundary conditions are presented for $v_{th} = 1.41$ and compared with the MHD results. Both fundamential ($k_z = \frac{\pi}{L_z}$) and first order ($k_z = \frac{2\pi}{L_z}$) modes were considered with the latter case being contrasted with the periodic model results. First of all though, the method used to handle the new boundary conditions is summarized.

4.4.1 Boundary Condition Implementation

The model with perfectly conducting boundary conditions differs from the periodic case with the addition of two guard cells at each end $z = 0$ and $z = L_z$. These cells are used to enforce the boundary conditions on each of the fluid variables corresponding to perfectly conducting ionospheres. These are $u_x = u_y = b_y = 0$, and $\frac{\partial b_x}{\partial z} = \frac{\partial b_z}{\partial z} = \frac{\partial j_z}{\partial z} = \frac{\partial E_z}{\partial z} = 0$.

The boundaries for the electrons are handled by allowing the electrons to freely propagate into the guard cell regions as if no boundaries existed at $L = 0$ and $L = L_z$ responding to the forces imposed on the guard cells by the fluid boundary conditions. The particle moments are then collected at only the grid cells in the region $0 < z < L_z$. The boundary conditions for the current and pressure moments are then imposed on the guard cells as with the case of the fluid. When the electrons reach the last guard cell at either end, they are then reflected back into the box to conserve particle number. This reflection appears to introduce some relatively large density fluctuations in the guard cell regions, but as long as the initial Shear Alfvén wave amplitude and distribution function temperature are maintained in the range considered here, these fluctuations do not significantly effect the results. For the simulations presented in this chapter the number of radial grid points, $n_x = 128$, and the number of field aligned grid points, $n_z = 20$, but comparison tests were made with $n_z = 14$ and $n_z = 28$. These two different resolutions change the size the guard cell regions by a factor of two, but the results were still found to be quantitatively consistent. For much higher temperature and Shear Alfvén wave amplitudes a different scheme for handling the perfectly conducting boundary conditions should be developed.

4.4.2 Simulations for $k_z = \frac{\pi}{L_z}$ and $k_z = \frac{2\pi}{L_z}$.

For the fundamental mode, $k_z = \frac{\pi}{L_z}$, the resonance frequency and period are respectively half and twice the values for $k_z = \frac{2\pi}{L_z}$. For both wavenumbers, ten period runs were conducted and so the former case actually evolved for twice as long in physical time. For each simulation, 70,000 time steps were used and figures (4.15) and (4.16) illustrate the evolution of the equatorial azimuthal velocity as a function of time for $k_z = \frac{\pi}{L_z}$ and $k_z = \frac{2\pi}{L_z}$ respectively. In both cases, the damping of the SAW is clearly evident but it is slightly stronger in the first order mode case. In addition, there is a slightly stronger shift to the right between the hybrid and fluid cases in the fundamental mode simulation relative to

73
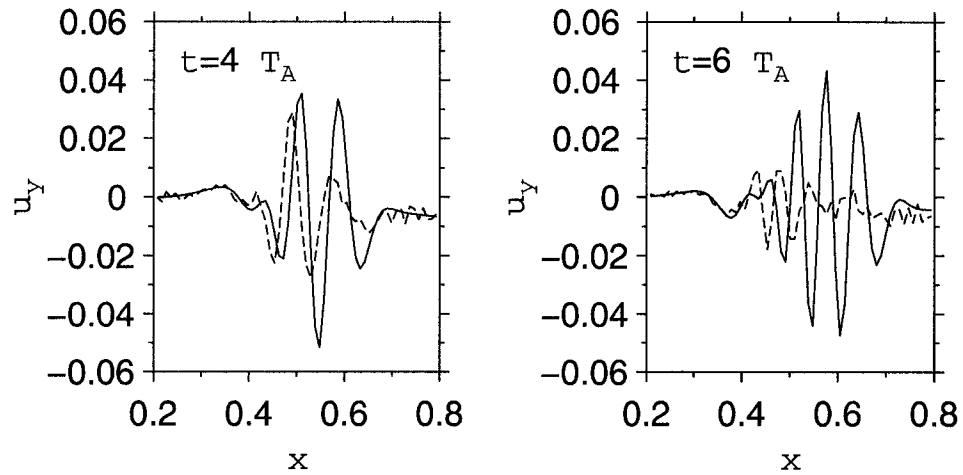
Figure 4.15: Comparison of the azimuthal velocity from the fluid model (solid line) and the hybrid model with conducting boundary conditions (dashed line) using the $v_{th} = 1.41$ initial electron distribution function for $k_z = \frac{\pi}{L_z}$. Slice at $z = 8.44$.
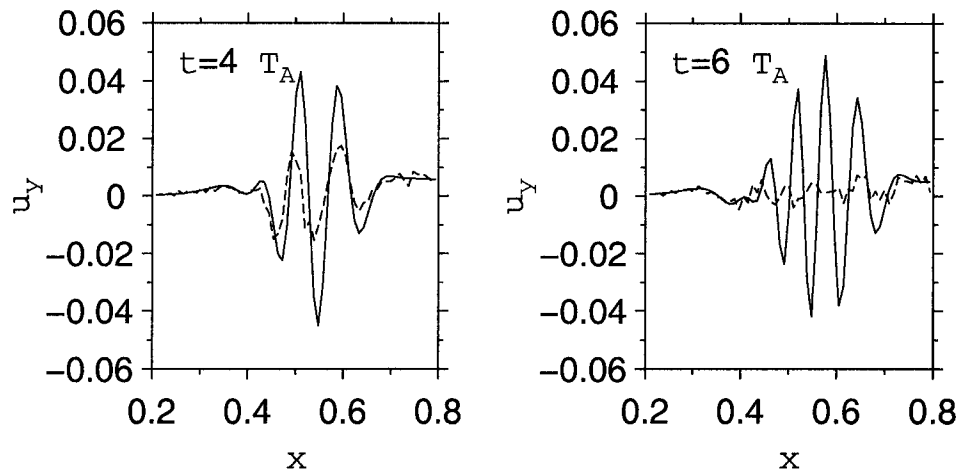
Figure 4.16: Comparison of azimuthal velocity for the fluid code (solid line) and the hybrid code with conducting boundaries (dashed line) for $v_{th} = 1.41$ and $k_z = \frac{2\pi}{L_z}$. Slice at z=3.94.

74

the latter. As mentioned previously, this shift is most likely due to the initial propagation of a kinetic SAW in the direction of decreasing Alfvén wave speed. The shift may be more dramatic in the fundamental mode case since the kinetic SAW would have twice as long to propagate relative to the first order mode case.

The evolution of the distribution function in both cases is illustrated in figure (4.17). Both distribution functions are strongly modified due to Landau trapping effects which is consistent with the decrease in the amplitude of u_y. It should be noted that even though, the frequency has different values for the two different wavenumbers, the ratio $\frac{\omega}{k_z}$ are the same in both cases. Therefore it is consistent that the modification of the distribution function should be taking place around $v_z = \pm 2$. The shape is slightly different in both cases, but this may have something to do with how the electrons interact with the different SAW modes. Also, in the first order mode case, the evolution of the distribution function shows more heating around $v_z = 0$ than in the case with periodic boundary conditions and may be a function of the different boundary conditions.

These results indicate a qualitative similarity between the results for the first order mode here and the simulations with periodic boundary conditions. A more quantitative comparison can be made through a comparison of the damping rate. The same procedure as used previously yields a value of $-0.005 \pm 0.001 s^{-1}$ which is the same order of magnitude as the damping rate measured for the $k_z = \frac{2\pi}{L_z}$ case with the periodic model. Therefore, the different boundary conditions do not seem to strongly effect the evolution of the system for current parameters.

75
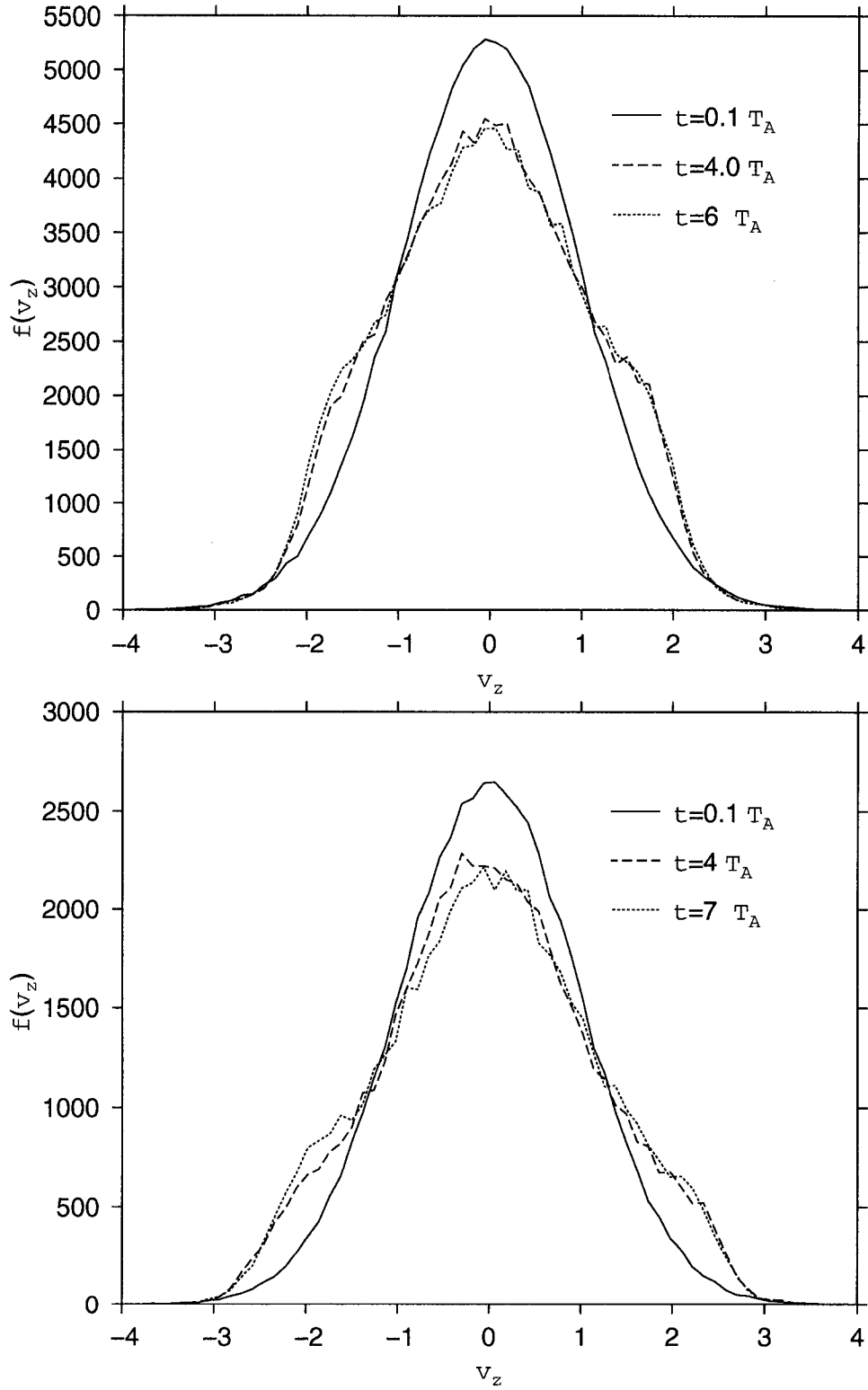
Figure 4.17: Top: Evolution of distribution function for the hybrid model with conducting boundary conditions for $k_z = \frac{\pi}{L_z}$ and $v_{th} = 1.41$. Bottom: Evolution of distribution function for the hybrid model with conducting boundary conditions for $k_z = \frac{2\pi}{L_z}$ and $v_{th} = 1.41$.

76

4.5 Summary

In this chapter, the 2D hybrid model was tested with both periodic and perfectly conducting boundary conditions. In the former case, the following was illustrated.

- The new electric field algorithm and the generalized ohm's law are identical in the fluid limit.

- The hybrid and cold plasma MHD models agree well in the limit that $v_{th} \ll V_A$ including the formation of an inertial Alfvén wave pulse.

- With $v_{th} \approx V_A$ and greater SAW can be strongly Landau damped. Damping rates are in good agreement with that determined from the analytical dispersion relation. The initial formation of a kinetic Alfvén wave is evident when $v_{th} > V_A$.

- The parallel electric field is generally too noisy to see directly from the simulation, but can be visualized with the post-simulation, frequency domain filtering. The noise does not effect the simulation results and the filtered electric field is consistent with other model variables.

For the model with perfectly conducting boundary conditions, it was shown that for $v_{th} \approx V_A$.

- Landau damping was evident for both the fundamental mode ($k_z = \frac{\pi}{L_z}$) and the first order mode ($k_z = \frac{2\pi}{L_z}$)

- for the first order mode, the quantitative results are very similar to the case with periodic boundary conditions indicating that the choice of boundaries in this case does not significantly effect the evolution of the system.

Therefore, with the exclusion of electric field resolution, the hybrid box model has been demonstrated to effectively capture the main physics expected between electrons and standing SAWs in different temperature regimes and with different boundary conditions. The evolution of the system can be followed accurately and stably with relatively small numbers of simulations electrons and the code should prove useful for the study of electron-SAW interactions in general.

Chapter 5

Dipole Model Simulations

5.1 Preamble

This chapter is broken up into two main sections. In the first, we will illustrate the cold plasma MHD model in dipolar coordinates. Results are presented for both the case $\lambda_e = 0$ and $\lambda_e > 0$. The results in the $\lambda_e = 0$ limit are contrasted with the results of a nonlinear resistive MHD model (Voronkov, 1998) run in the cold plasma limit. The resonance shift in frequency between the nonlinear and linear cases is illustrated, but it is shown that from the point of view of the number of periods, the phase mixing evolution in both cases is essentially identical.

In the second part, results of the hybrid model are presented for several equatorial densities and two ionospheric positions (at 3 and 5 R_E). Within this, the hybrid and test-particle models are contrasted in the cold plasma limit, the inertial SAW and thermal plasma limits are examined and the parallel electric field in the hybrid and MHD cases are compared in the cold plasma limit. It is found that the model has very good agreement with the cold plasma MHD results in the cold plasma limit, including for the parallel electric field. As well, the divergence of the cold plasma MHD and hybrid model in the thermal plasma case illustrates the model is consistent in this regime as well.

5.1.1 Boundary Conditions

As with the hybrid model in cylindrical coordinates, open boundary conditions are again chosen for the radial direction. At the ionospheres, we use perfectly conducting boundary conditions so as outlined before, we have $u_2 = u_3 = E_2 = E_3 = 0$ and $\frac{\partial j_1}{\partial x_1} = \frac{\partial E_1}{\partial x_1} = 0$. The condition that the parallel current is continuous across the ionospheric boundary yields the magnetic field boundary conditions as follows. The curl of the magnetic field in curvilinear coordinates is given by,

78

$$\vec{j_1} = \nabla \times \vec{B} \tag{5.1}$$

$$= \frac{1}{h_1 h_2 h_3}[h_1 \hat{x}_1(\frac{\partial}{\partial x_2}(h_3 B_3) - \frac{\partial}{\partial x_3}(h_2 B_2)) \tag{5.2}$$

$$+ h_2 \hat{x}_2(\frac{\partial}{\partial x_3}(h_1 B_1) - \frac{\partial}{\partial x_1}(h_3 B_3)) \tag{5.3}$$

$$+ h_3 \hat{x}_3(\frac{\partial}{\partial x_1}(h_2 B_2) - \frac{\partial}{\partial x_2}(h_1 B_1))]. \tag{5.4}$$

The boundary condition for the field aligned current is that $\frac{\partial j_1}{\partial x_1} = 0$, yields

$$\frac{\partial}{\partial x_1 \partial x_2}(h_3 B_3) - \frac{\partial}{\partial x_1 \partial x_3}(h_2 B_2)) = 0 \tag{5.5}$$

Since the shear Alfvén wave mode can be either entirely poloidal or toroidal, both terms must be equal to zero. Therefore $h_2 B_2$ =constant and $h_3 B_3$ =constant.

5.2 Fluid Model Simulations

The simulations presented in this section were done with the cold plasma MHD code. In all cases, the ionospheres were located at 1 R_E and the equatorial radial boundaries of the model are at 9 and 11 R_E. The resonance was initialized on the L=10 magnetic field line. We used 64 grid points in the field aligned direction and 200 in the radial direction. Two density profiles are considered (thus having different Alfvén periods, but in either case, the simulation was run for 60 T_A with 100,000 time steps.

The ionospheric boundary conditions highlighted in the previous section were enforced across the first two and last two grid cells in the field aligned direction. The radial boundary conditions were again assumed to be open.

5.2.1 Plasma parameters

For the simulations to follow, the FLR was initialized with a Gaussian type profile for the Shear velocity u_3 to correspond to a toroidal resonance system given by

$$u_3(t = 0) = Au_n(x_1, x_{2r})exp(-(\frac{1}{x_2} - \frac{1}{x_{2r}})^2/w^2) \tag{5.6}$$

where u_n is the eigenmode solution at the resonance position (see next section) and x_{2r} is the value of x_2 at the resonance position. The amplitude of the Shear mode is chosen so that it has a peak velocity in the equator of 50 km/s and w=0.2 in nondimensional units.

For the simulations to follow, two density distributions will be considered and they are illustrated in figure (5.1). Profiles (a) and (b) are derived from the formula

$$\rho = \rho_o = \rho_{eq}(1 - cos\theta^2)^{-1} \tag{5.7}$$

79
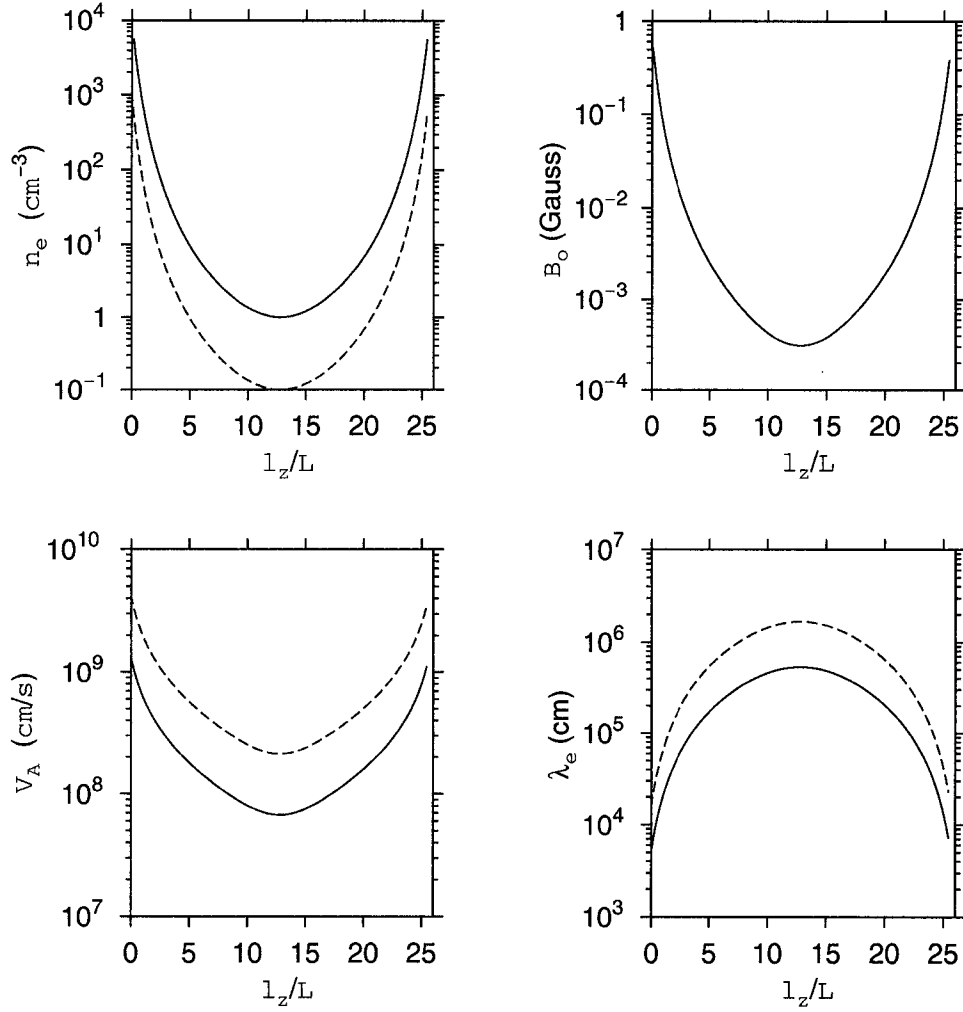
Figure 5.1: Plasma parameter profiles along the L=10 field line corresponding to density profile (a) (solid line) and density profile (b) (dashed line) (see text). Here l_z is the distance along the field line. The left hand side of the figure is the equatorial region and the right hand side is the ionosphere.

where $q = 4$ in both cases and $\rho_{eq} = m_p$ cm^{-3} for the former and $\rho_{eq} = 0.1$ m_p cm^{-3} for the latter. Density profile (a) corresponds to the profile used by Voronkov (1998). Also included in the diagram are Alfvén and electron inertial length profiles. Figure (5.2) shows the radial profile of the Alfvén at the equator. It increases in the earthward direction.

5.2.2 Linear Shear Alfvén waves in a Dipolar Magnetosphere

In both the fluid and hybrid models in dipolar coordinates, the parallel Alfvén velocity profile is not constant and so the dispersion relation for the Shear Alfvén wave is not as trivial to solve as for the cases considered in the box and cylindrical coordinate models. A discussion of the solution of the dispersion relation in dipolar coordinates is given in detail in Voronkov (1998) and won't be repeated here. The eigenmodes for u_3 and b_3 were

80
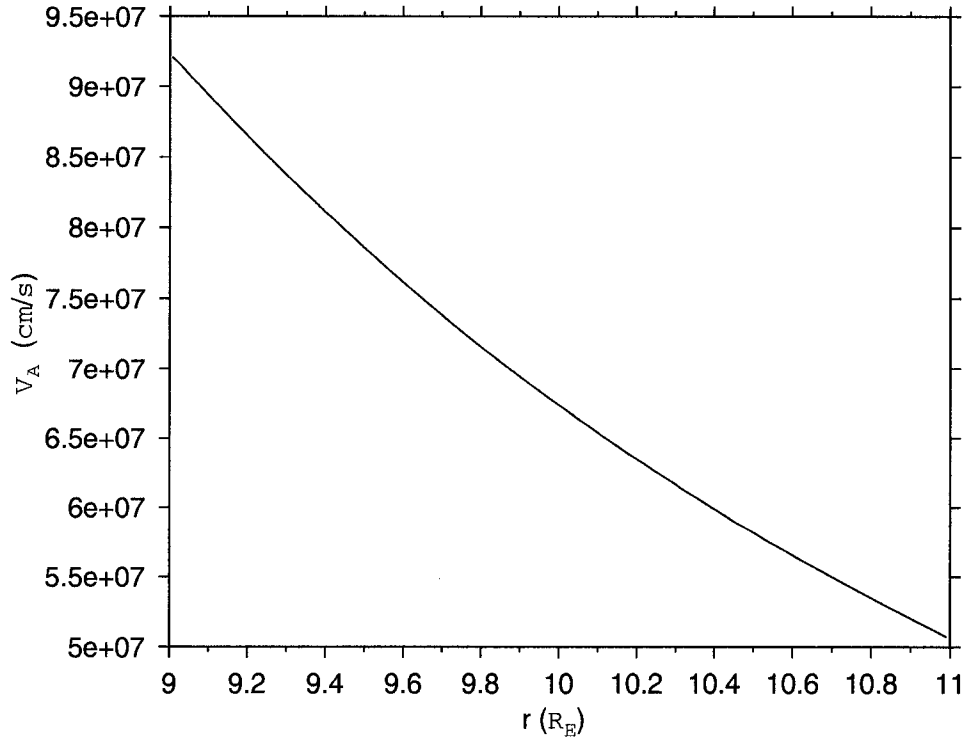
Figure 5.2: Equatorial radial Alfvén velocity profile.

calculated for density profile (a) and the normalized profiles are illustrated in figure (5.3). The period of this eigenmode is T=322 s.

5.2.3 Linear and Nonlinear Evolution in the Cold Plasma MHD Limit

In this section the linear cold plasma MHD model is contrasted with the nonlinear MHD dipolar model (Voronkov, 1998). The latter model has no parallel electric field and so this was turned off in the cold plasma code. Also, very small pressures had to be used in the nonlinear code for stability reasons.

Both programs were intialized with the same u_3 profile as already highlighted and the evolution of the equatorial amplitude of the Shear velocity is illustrated in figure (5.5). As is evident for the first two periods, there is little difference between the two simulations, but a growing phase difference is evident after that. In the nonlinear model, the resonant period of the field line is increasing and consequently, the resonant frequency is decreasing. This makes sense as there should be a decrease in resonant frequency due to nonlinear effects (Voronkov, 1998) which would not be evident in the linear code. The nonlinear effects come in via the pondermotive force which drives plasma toward the equator increasing the equatorial plasma density and consequently lowering the equatorial Alfvén velocity. Since the resonant period of the field line is proportional to the ratio of the parallel wavelength and V_A, the period increases as V_A drops. The amplitude also decreases in the nonlinear case which is also consistent with the figure.

81
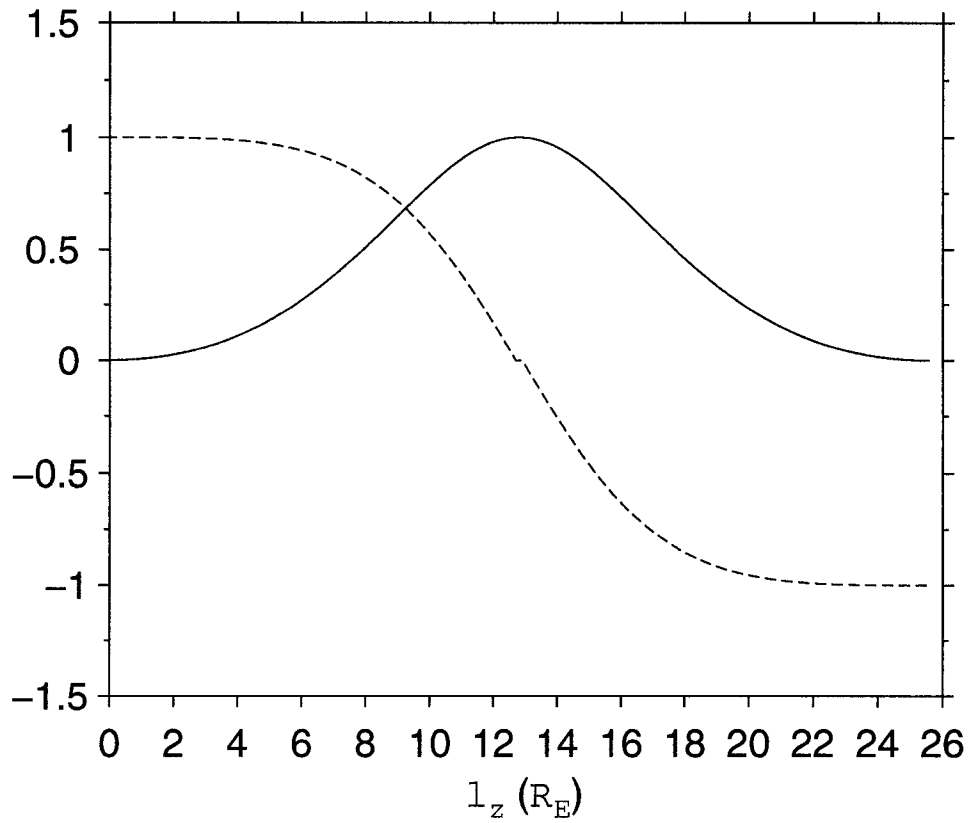
Figure 5.3: Profile of u_3 (solid line) and $h_3 b_3$ (dashed line) for the fundamental Shear Alfvén wave mode along the L=10 magnetic field line. u_3 and $h_3 b_3$ are normalized by the equatorial and boundary values respectively.
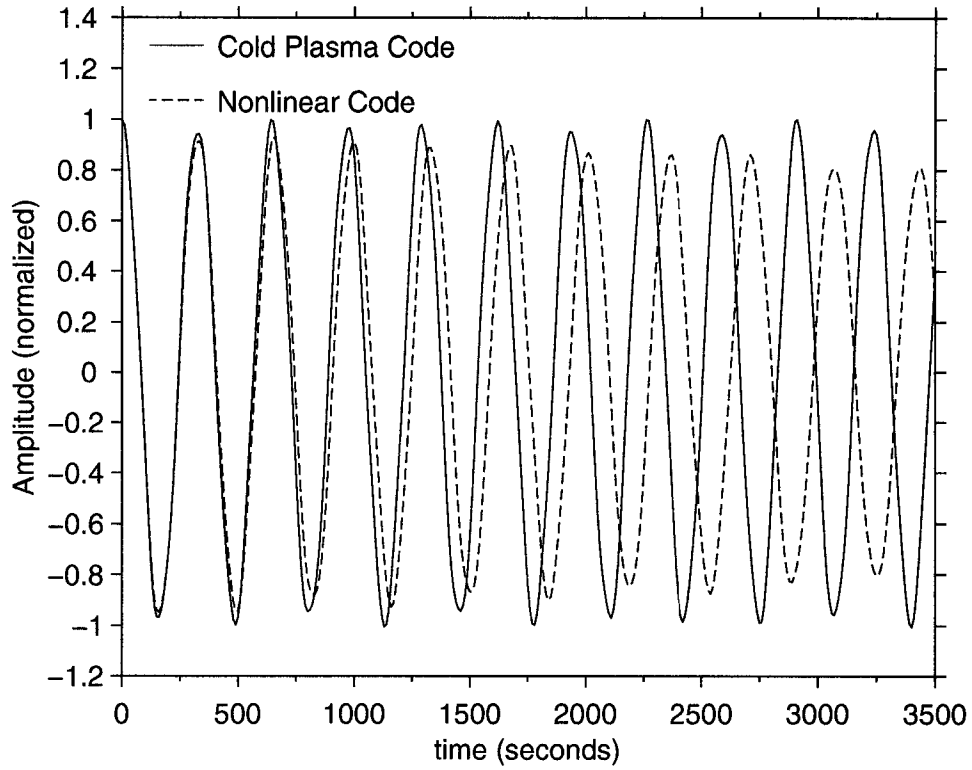
Figure 5.4: Comparison of the equatorial amplitude of u_3 at 10 R_E as a function of time for the cold plasma code (solid line) and the nonlinear code (dashed line).
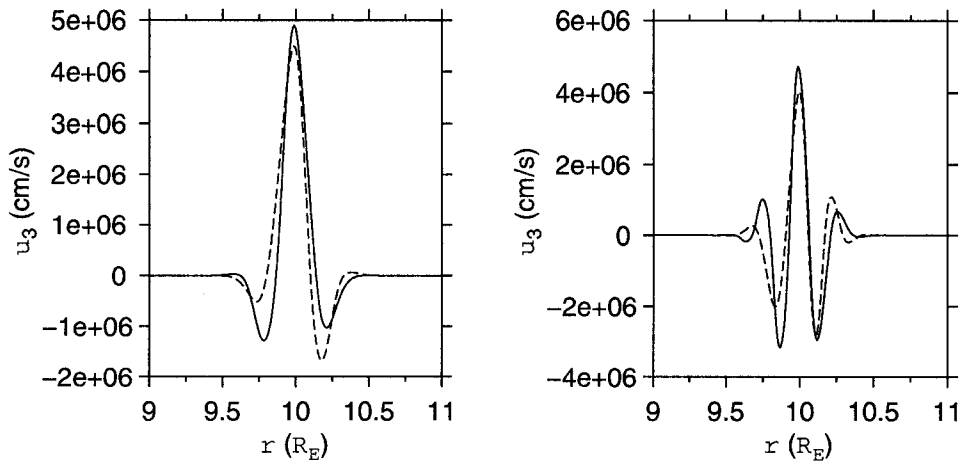
Figure 5.5: Comparison of the equatorial radial profile of u_3 for the cold plasma code (solid line) and the nonlinear code (dashed line) after 5 oscillations (left) and after 10 oscillations (right).

83

If however, this shift is neglected and the radial current densities are compared after an equal number of oscillations (see figure (5.5)), it is evident that the radial structure is very similar in both cases. Therefore, the shift in resonant frequency aside, the linear and nonlinear codes yield essentially the same results in the cold plasma limit.

5.2.4 Electron Inertial Effects in the Cold Plasma Limit

In this section we present simulations using the cold plasma MHD code including electron inertial effects. Results will be presented for both the density distributions (a) and (b) outlined previously and the same initial Shear Alfvén velocity profile will be used as in the previous section. Figure (5.6) illustrates the simulation results for density distribution (a). Phase mixing effects are clearly visible, but the electron inertial lengths are too small to have any influence. Figure (5.7) is the same plot, but now for density distribution (b) where due to the decreased density along the field line, the electron inertial effects are enhanced and some propagation of the inertial SAW pulse in the direction in increasing Alfvén wave gradient is evident (NOTE: this increase in the gradient is to the right when viewed as a function of x_2 and to the left when viewed as a function of r in the equatorial plane).

Figure (5.8) illustrates ionospheric slices of current density and electric field from both of the previous runs with $\lambda_e \neq 0$. As is consistent with other work (Rankin et al., 1999) in the MHD limit, the current density is the same order of magnitude as observed, but the magnitude of the parallel electric field is well below the mV/m scales observed.

5.3 Numerical Details for the Test Particle and Hybrid Models

5.3.1 Particle Placement

Unlike in the box and cylindrical models, the particles are not placed according to a specified fluid density function. The positions of the particles are used to specify the fluid density function. In the radial direction, we have chosen to place the electrons equally spaced in r_o. This results in a constant radial density profile as a function of x_2. Along the field line, the electrons are placed equally spaced in x_1 which yields an increasing density profile toward the ionospheres. The variables n_{p_1} and n_{p_2} respectively indicate the number of electron positions assigned in the parallel and radial directions respectively. Once all the initial simulation electron positions are established, the entire profile is then uniformly scaled so that it has an equatorial value of n_{eq}.

5.3.2 Filtering

It was discussed in Chapter 4 how the 2 D digital filter was applied quite successfully in the box model. The same was tried with the dipolar model, but the program becomes unstable at the ionospheres when filtering is applied in the field aligned direction (even when the

84
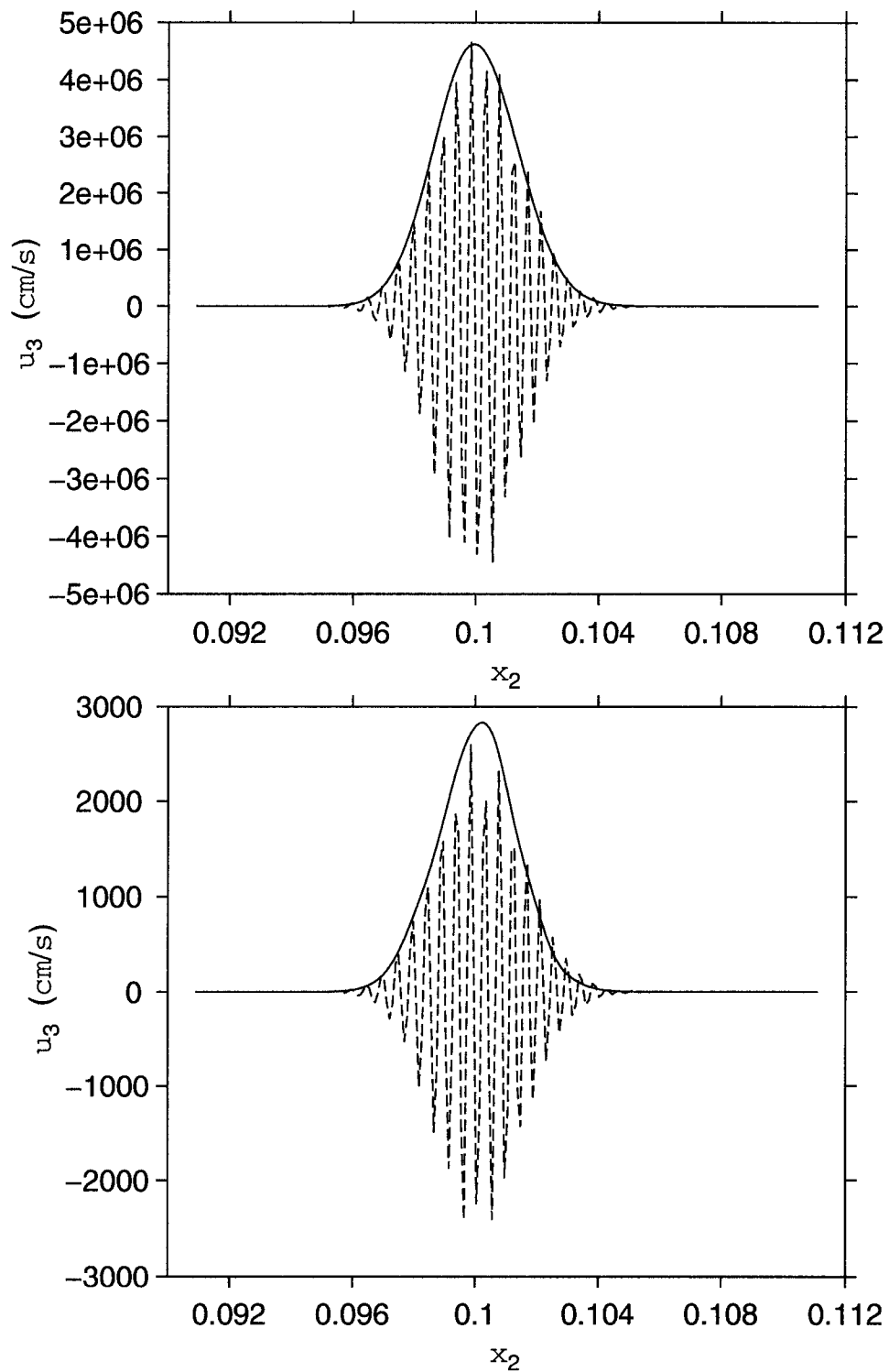
Figure 5.6: Comparison of the radial profile of u_3 for density profile (a) at t=$1T_A$ solid line and t=60 T_A (dashed line). Top: equatorial slice. Bottom: southern ionospheric slice.

85
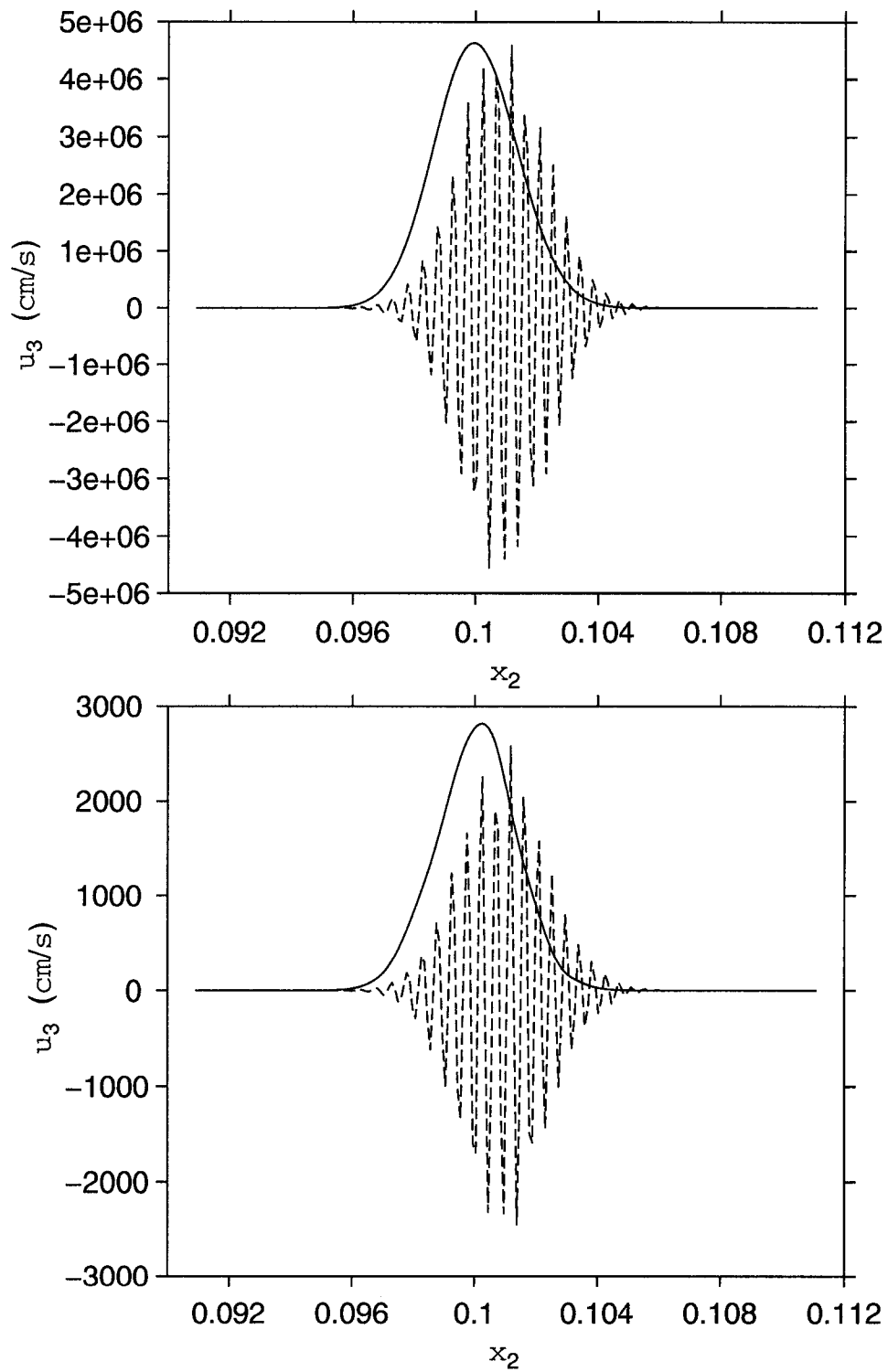
Figure 5.7: Comparison of the radial profile of u_3 for density profile (b) at t=1 T_A (solid line) and t=60 T_A (dashed line). Top: equatorial slice. Bottom: southern ionospheric slice.

86
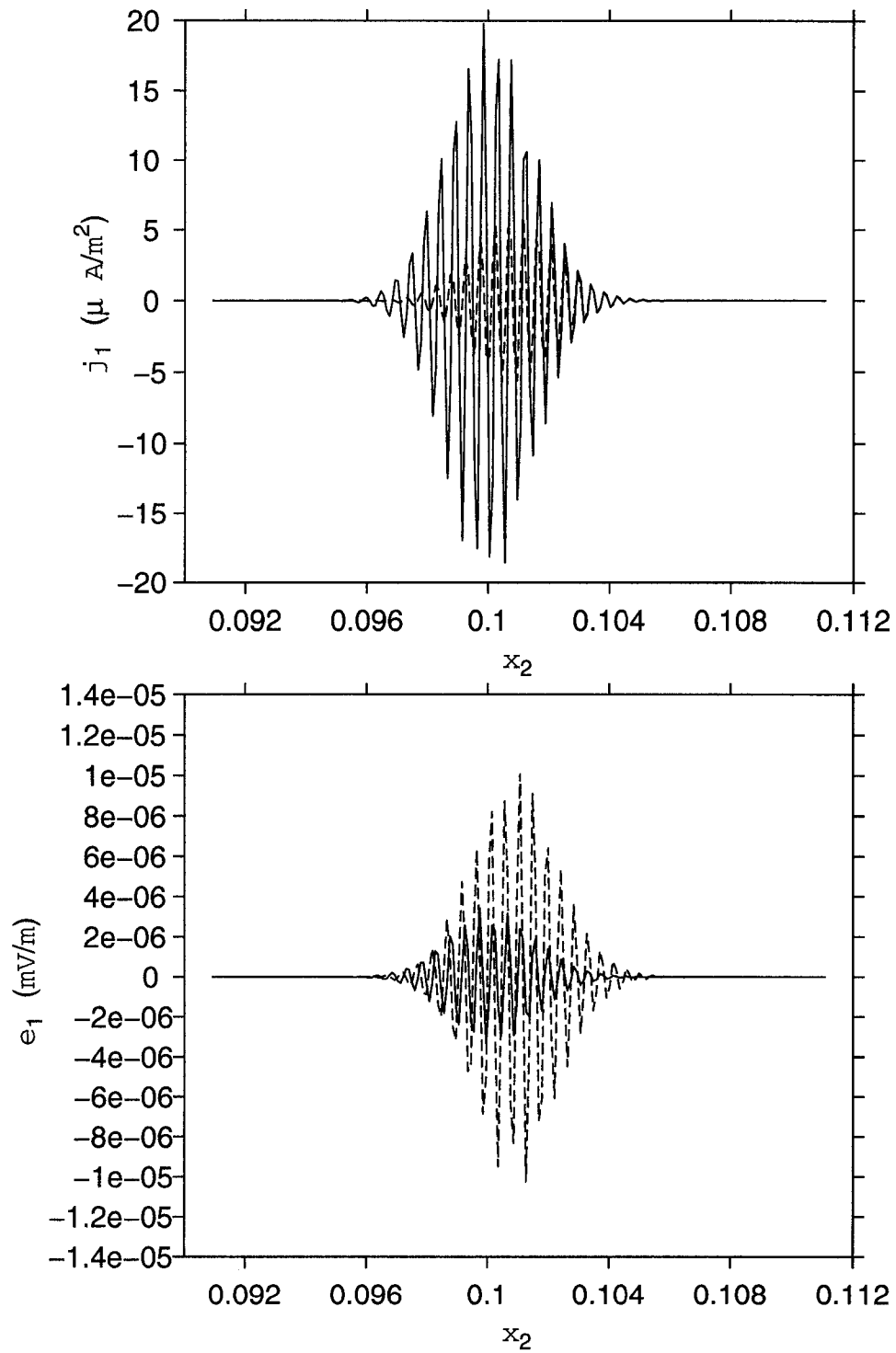
Figure 5.8: Comparison of ionospheric slice of the parallel current density (top) and parallel electric field (bottom) at t=60 T_A for density profile (a) (solid line) and density profile (b) (dashed line).

87
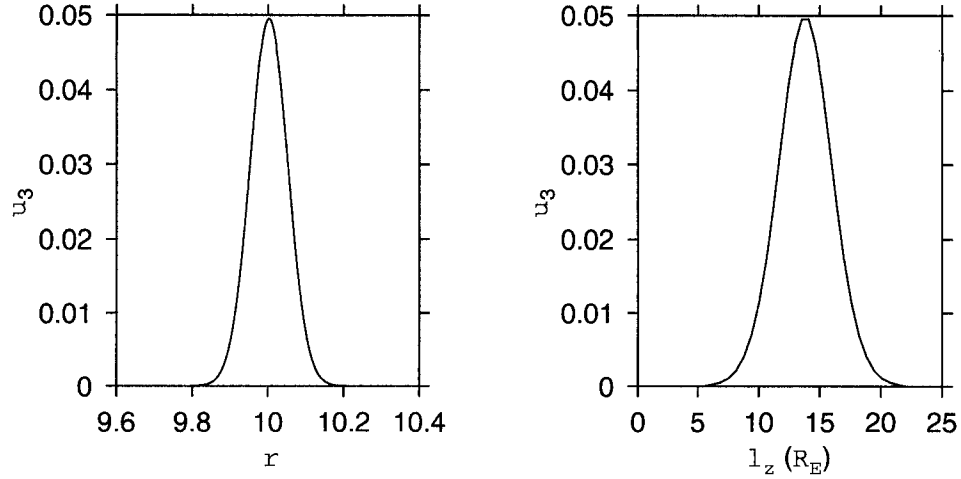
Figure 5.9: Initial Shear Alfvén wave profile. Left: Radial profile. Right: Field Aligned profile.

filtering is not applied across the ionospheric boundary). Therefore to date with the dipolar model, only radial filters have been applied (both frequency and lag domain). These are not used in any of simulations presented here as their effect is minimal. The source of most of the noise is from the field aligned direction as is evident from the fact that increasing the field aligned particle number does the most to clean up the simulations. The issue of proper filtering within the dipolar code needs to be addressed more completely, but the problem has been fairly well compensated for by increasing the particle number.

5.3.3 Initial Profile

Unlike the fluid model simulations, we did not choose a proper eigenmode for the density and magnetic field profiles, but instead just specified a two dimensional Gaussian of the form

$$u_3(x_2, x_1, t_o) = A exp(-\frac{(\frac{\pi}{2} - \theta(x_{2r}, x_1))^2}{d_1^2}) exp(-\frac{(\frac{1}{x_2} - \frac{1}{x_{2r}})^2}{2d_2^2}) \qquad (5.8)$$

where A is the Shear Alfvén wave amplitude set to 34.5 km/s, $d_1 = 0.3$, $d_2 = 0.05/L$ and x_{2r} is the resonance position. The resulting profile is shown in figure (5.9) where the field aligned profile is taken along x_{2r}.

5.3.4 Maxwellian and Pitch Angle Distribution

The Maxwellian distribution function is chosen with the same algorithm as outlined for the box model. However, the velocity in this case is the total velocity v, rather than just the parallel component v_1. In order to reduce boundary noise, the velocity values are multiplied by a radial shape function so that they are set to zero close to the boundaries. The hypergaussian function given by

88
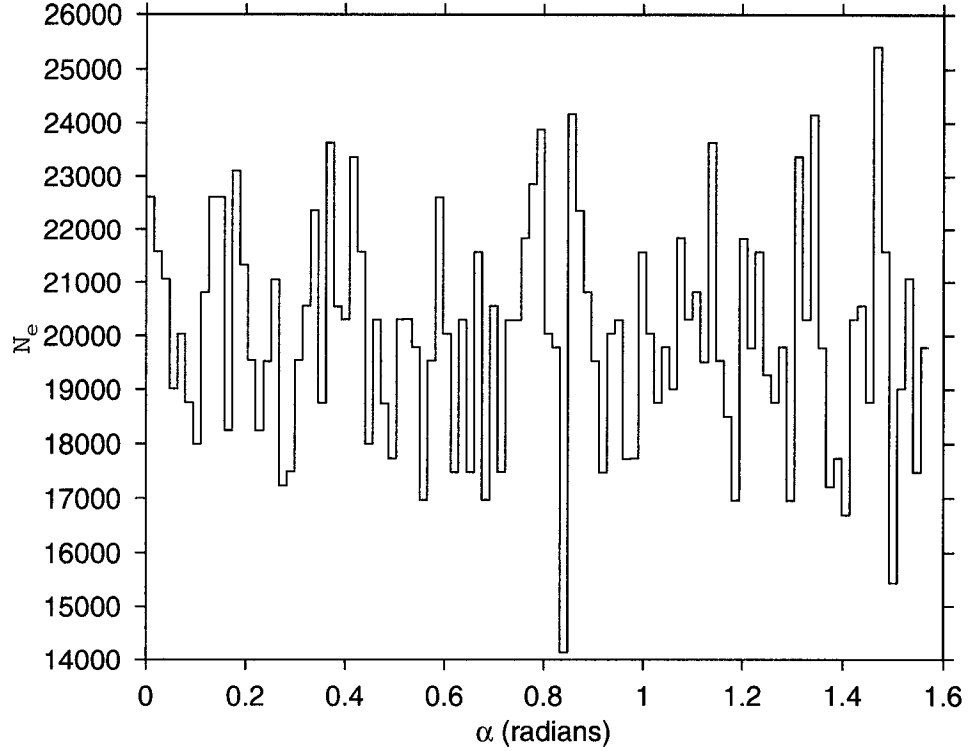
Figure 5.10: Initial pitch angle distribution for the case $T_e = 1.0$ with $n_p = 2 \times 10^6$. (N_e = number of simulation electrons).

$$v_i = v_i exp\left(\frac{(r_{oi} - r_{or})^{18}}{1 \times 10^{-11}}\right) \qquad (5.9)$$

is used where r_{oi} is the r_o value of the field line the ith electron is attached to.

Using a random number generator, pitch angles between 0 and 90 degrees are assigned to each simulation electron in the distribution. This is a meant to be a constant density distribution as a function of pitch angle, but the finite number of simulation electrons used yields some variation around the mean. The pitch angle distribution for the case of $T_e = 1.0$ with $n_p = 2 \times 10^6$ is illustrated in figure (5.10). The results of this simulation will be presented in the next section.

Using its respective pitch angle, the parallel and perpendicular, $v_\perp$, velocities are then calculated for each simulation electron. The latter values, along with the local magnetic field at the particles initial position are then used in the determination of the magnetic moment, μ_m. A distribution function of the magnetic moment using the previously displayed pitch angle distribution is displayed in figure (5.11). Also shown is the result for an initial $T_e = 10$ eV initial electron distribution function using 5×10^6 simulation electrons.

89
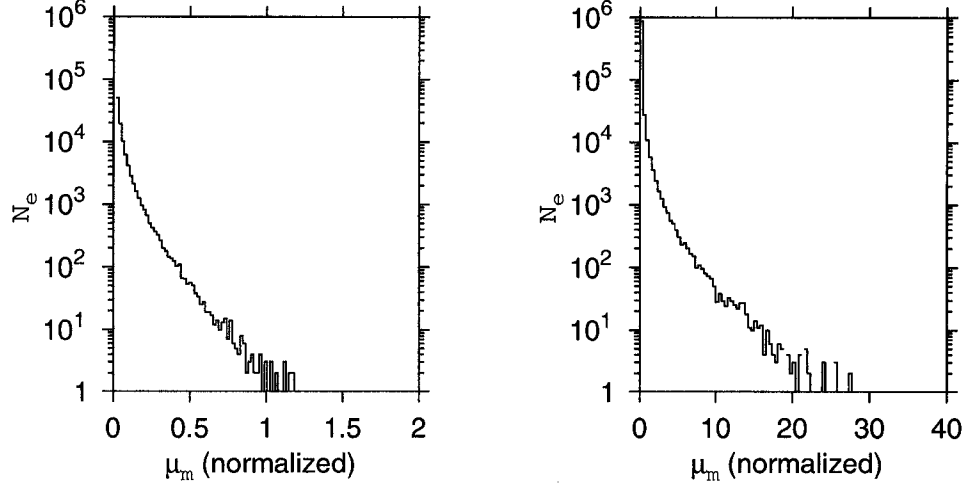
Figure 5.11: Left: Initial magnetic moment distribution for the case $T_e = 1.0$ with $n_p = 2 \times 10^6$. Right: Same, but for $T_e = 10.0$ and $n_p = 5 \times 10^6$.

5.4 Comparison of Test Particle Model and Hybrid Model in the cold plasma limit

In this section will be presented simulations with the hybrid model for $n_{eq} = 0.1 \ cm^{-3}$ and two initial Maxwellian distribution functions with average energies $T_e = 1$ eV and $T_e = 10$ eV where the thermal velocity is related to T_e by $v_{th} = \sqrt{\frac{2T_e}{m_e}}$. The ionospheres are at $5R_E$ and the equatorial radial boundaries are at 9.7 R_E and 10.3 R_E. Profiles along the $L = 10$ field line of the density, ambient magnetic field, Alfvén velocity and inertial length profiles are illustrated in figure (5.12).

For both of these simulations we used 128 grid points in the x_2 direction and 32 in the x_1 direction along with a time step of 0.0067 seconds. Figure (5.13) illustrates the equatorial amplitude of u_3 as a function of time for a fluid model run. The fact that a mode with a period of about 80 s dominates indicates that the 2 D Gaussian profile used, is close enough to the fundamental eigenfunction so that this single mode dominates.

Figures (5.14) and (5.16) illustrate the comparison of the Ampere's law current density and the electron current density for the test particle model and hybrid model respectively. The slices are taken along the southern ionospheric boundary inner grid cell. Unlike the box model and cylindrical model cases there is a significant divergence between the two current densities in the test particle case. This is due to the presence of the magnetic mirror force. Initially, the influence of the electric field is minimal and the magnetic mirror force dominates acting against the electron motion toward the ionospheres. This appears as a net positive displacement in current for the northern ionosphere and a net negative displacement at the southern ionosphere (as seen in figure (5.14)). As the electric field has more time to act on the electrons, the electron current density becomes more random and centered around zero. Time slices of this parallel electric field for the test particle model

90
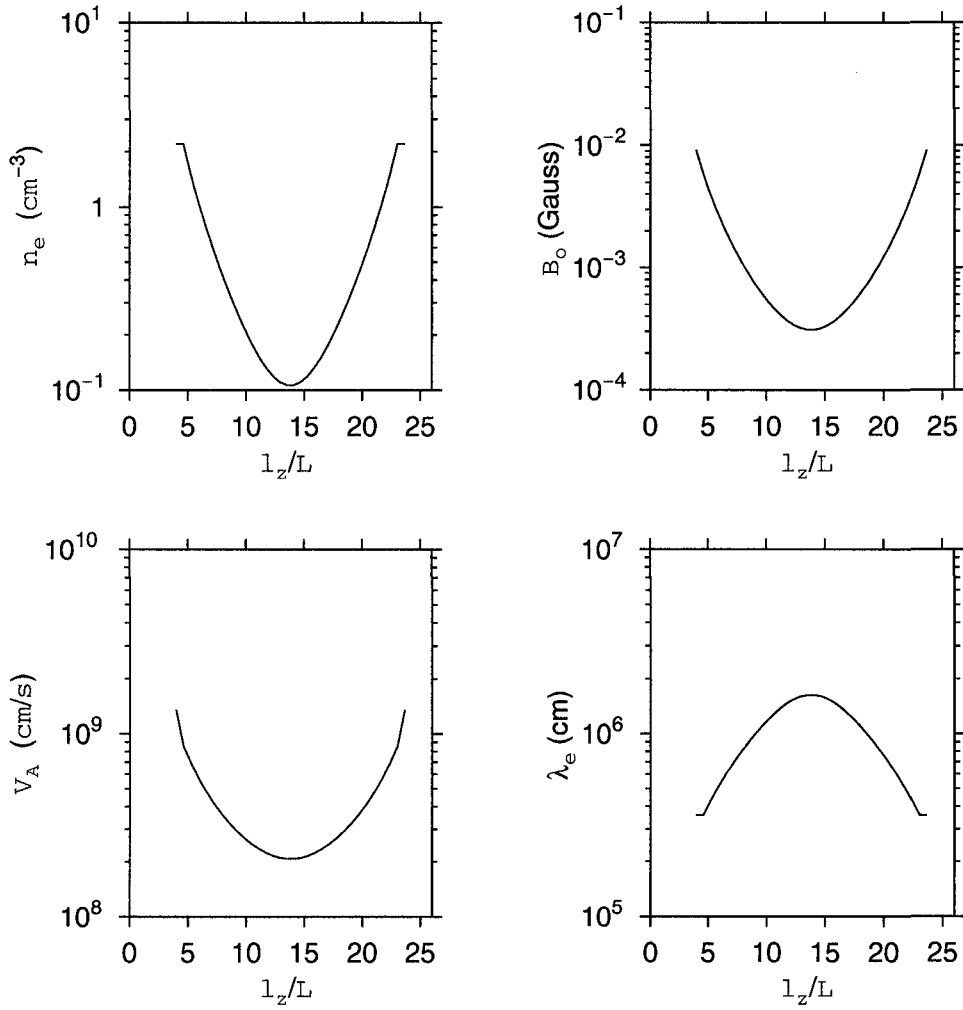
Figure 5.12: Plasma parameters in the hybrid model corresponding to $n_{eq} = 0.1 cm^{-3}$

91

are displayed in figure (5.15). The magnitude of the field stays the same order of magnitude through the full length of the run.

The evolution of the distribution function as a function of time for the hybrid model case is illustrated in figure (5.17). As is evident, the distribution function undergoes an initial quick adjustment as the hybrid system converges. However after that, there is little adjustment through 9 oscillation periods. The heating is less than observed in the box model or cylindrical model cases and it is assumed that the balance between the electric field and mirror force restricts the heating that would otherwise occur if the mirror force were not present. The distribution function for the hybrid and test particle runs are contrasted in figure (5.18) at t=400 seconds. The width in both cases is qualitatively equal with the major difference being that the test particle distribution has a internal structure associated with it. This is smoothed out in the case of the hybrid model distribution.

In order to investigate the effect of increasing the electron distribution temperature, an additional simulation was done with $T_e = 10$ eV using 5 million simulation electrons. In this case as well, the fluid fields stay very close to the cold plasma MHD results and so are not displayed here. The evolution of the distribution function is shown in figure (5.19). As is evident in this case as well, there is little effect of wave-particle interactions and the distribution function is not significantly modified. Higher temperatures would no doubt somewhat enhance the effects of the pressure and magnetic moment terms in the equation for the parallel electric field. However no additional simulations were done for these model parameters and higher T_e for two reasons. The first is the time required, as large increases in particle number would be needed to maintain resolution with temperature increases. Secondly, the results of Rankin et al. (1999) suggest that significant increases in the parallel electric field will only be found at altitudes of 2-3 R_E and they used a $T_e = 100$ eV initial Maxwellian. The focus of the research has therefore been to test the model with lower altitude ionospheres and initial results in this direction will be summarized in the next section.

5.4.1 Single Particle Dynamics

The comparisons between the test particle simulations and hybrid simulations introduced in the last section can be further highlighted by looking at single particle dynamics. Figure (5.20) illustrates the trajectories of test electrons with 1, 5 and 10 eV energies released at the equator at $r = 10$ R_E with and without the resonance electric field. There is very little divergence between the two cases except for the 5 eV case where the electron is undergoing a resonant interaction with the electric field. The period of the electron motion is approximately twice that of the resonance. Therefore, in the test particle limit for most electrons, there will not be large divergences in their orbits due to the resonance electric field.

Figure (5.21) illustrates the trajectories of the two same electrons in the test particle
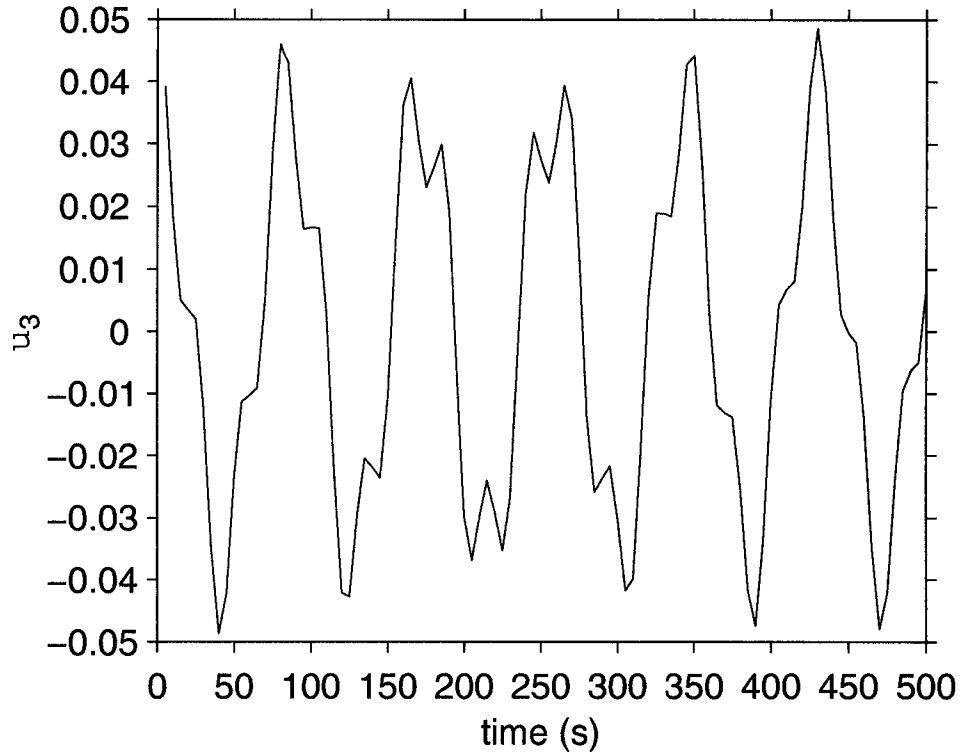
Figure 5.13: Comparison of equatorial amplitude of u_3 at x_{2r} as a function of time for the fluid model with $n_{eq} = 0.1 \ cm^{-3}$.

and hybrid models respectively. It is clear that in the test particle limit, the electrons seem to be moving with pretty much the same orbits as they would have under the influence of the dipolar magnetic field alone. In the hybrid case however, the orbits are drastically altered under the influence of the coupling. As in the box model simulations, these results were not significantly altered with the exclusion of both the pressure and magnetic moment components of the electric field and so the orbits of the motion are most significantly affected by the local electric field imposed in the enforcement of quasineutrality. The peculiar motion of the second electron is explained by the fact that it reaches the ionosphere and is re-injected at the first guard cell with the same energy.

5.5 Comparison of simulations with Ionospheres at 5 and 3 R_E

Thus far, simulations with the hybrid code have been limited to having ionospheres at 3 R_E above the earth due to boundary issues that will be highlighted later. In this section is presented a simulation using this boundary for an initial 1 eV electron distribution function and the results will be contrasted with the $5R_E$ case summarized previously. The initial Shear Alfvén wave perturbation is the same in both cases.

Figure (5.22) illustrates u_3 at the equator and the current, pressure and μ_m moments of

93
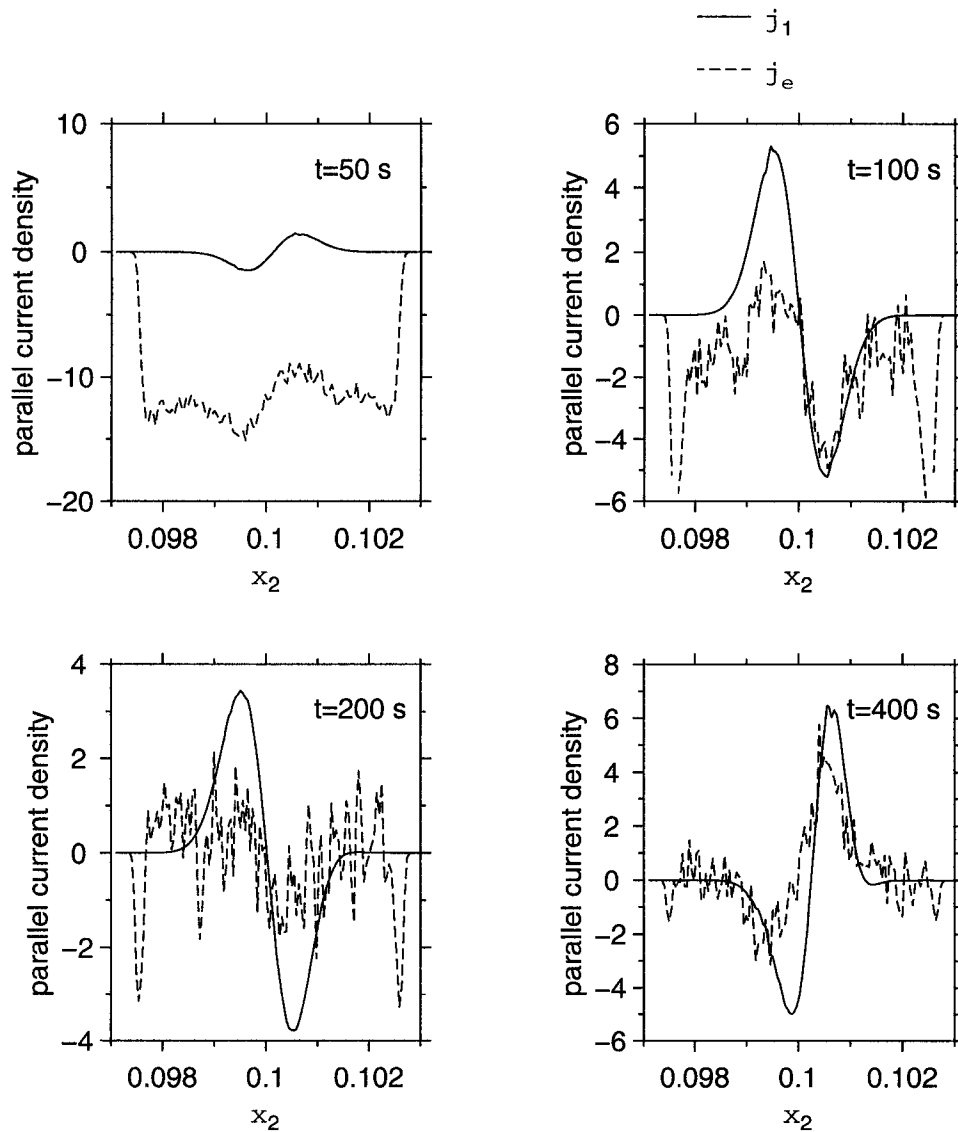
Figure 5.14: Comparison of the perpendicular profile of Ampere's law current, j_1 (solid line) and electron current j_e (dashed line) for the test particle model with $T_e=1$ eV initial Maxwellian distribution function. Southern ionospheric slice.

94
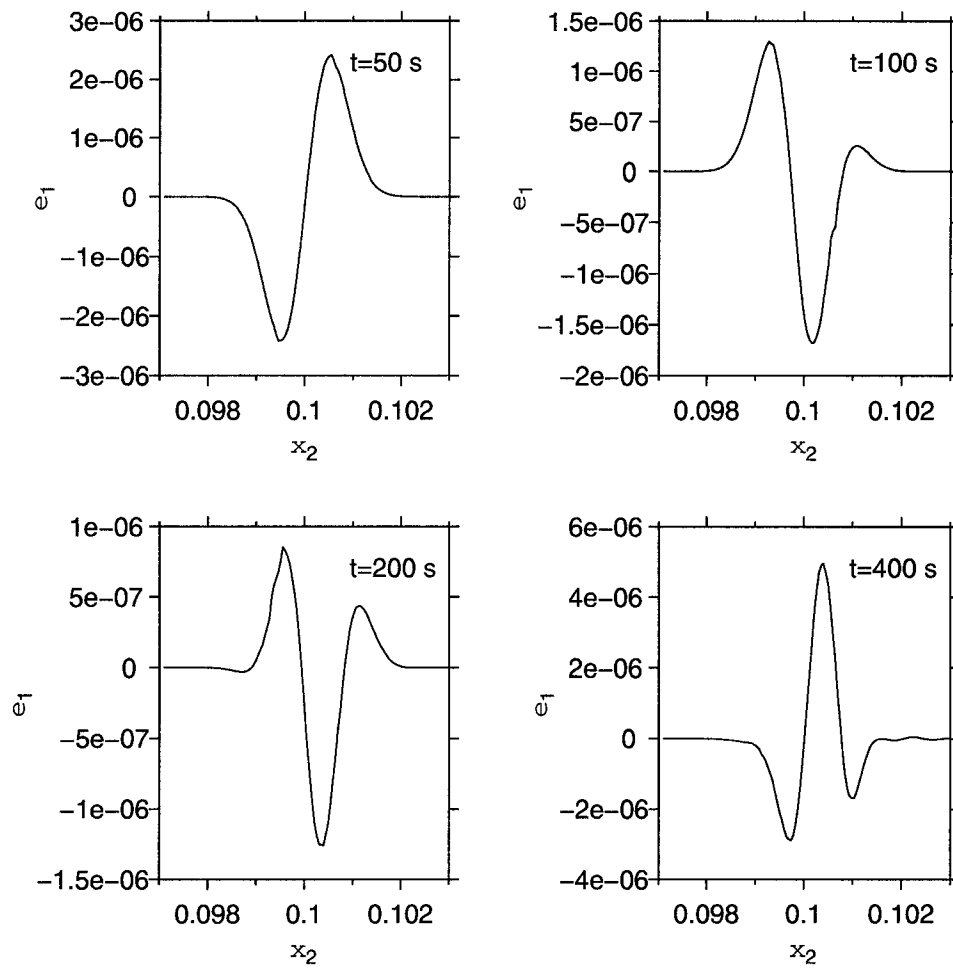
Figure 5.15: Perpendicular profile of the parallel electric field for the test particle model. Southern ionospheric slices.

95
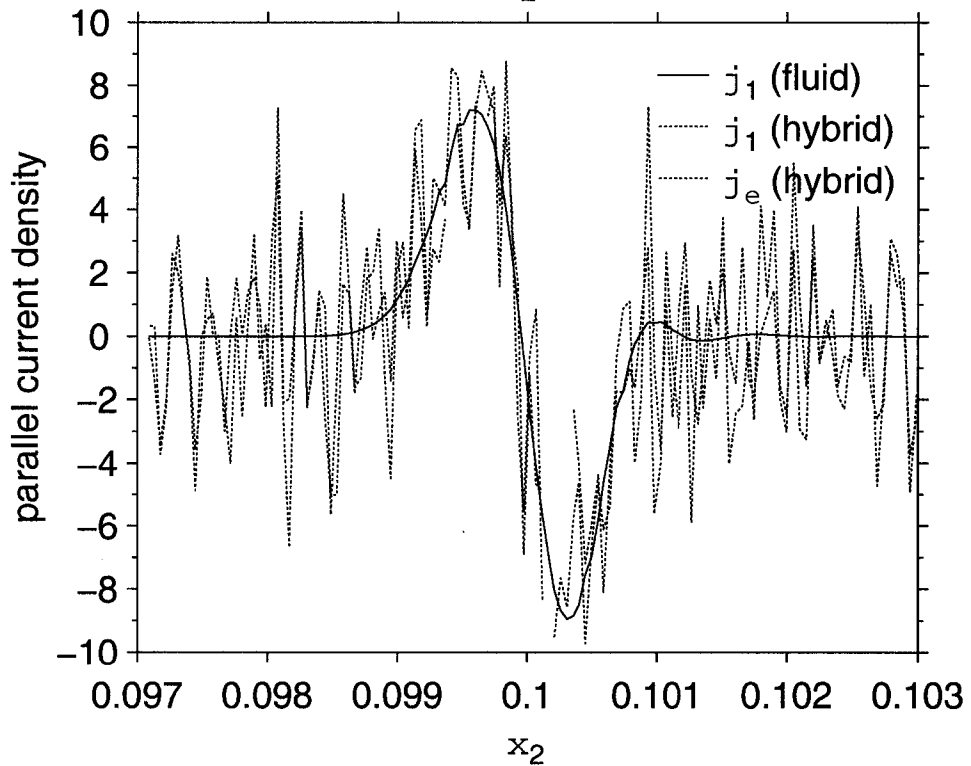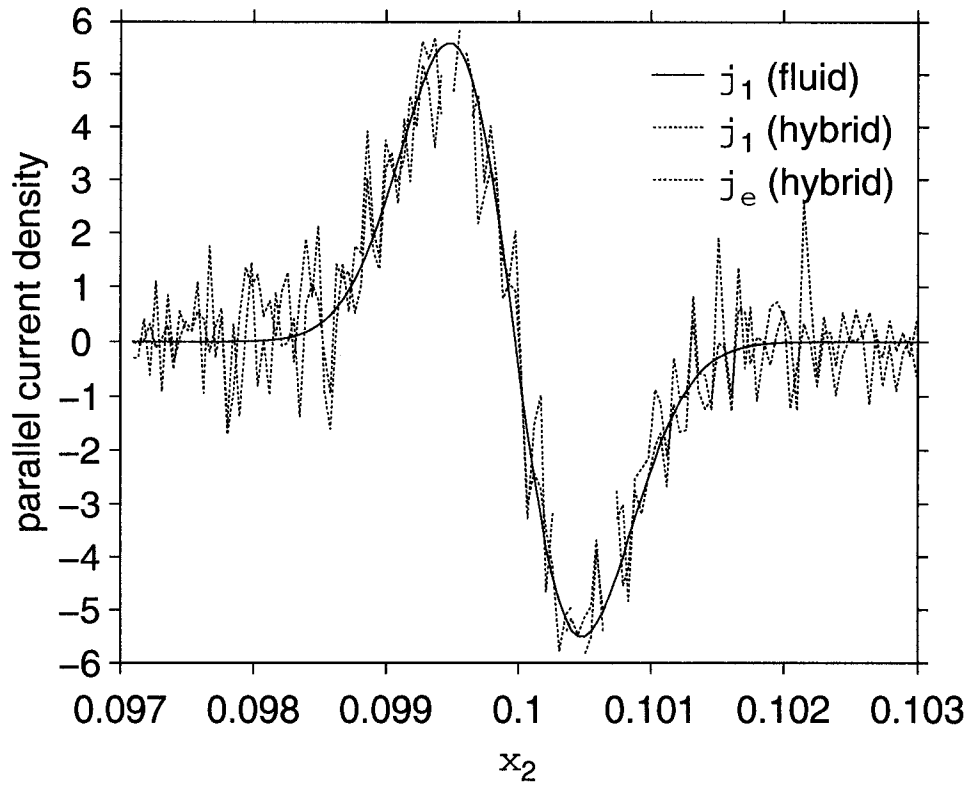
Figure 5.16: Perpendicular profile of Ampere's law current, j_1 (solid line) and electron current j_e (dashed line) for the hybrid model with T_e=1 eV initial Maxwellian distribution function. Top: t=20 s. Bottom: t=450 s.

96
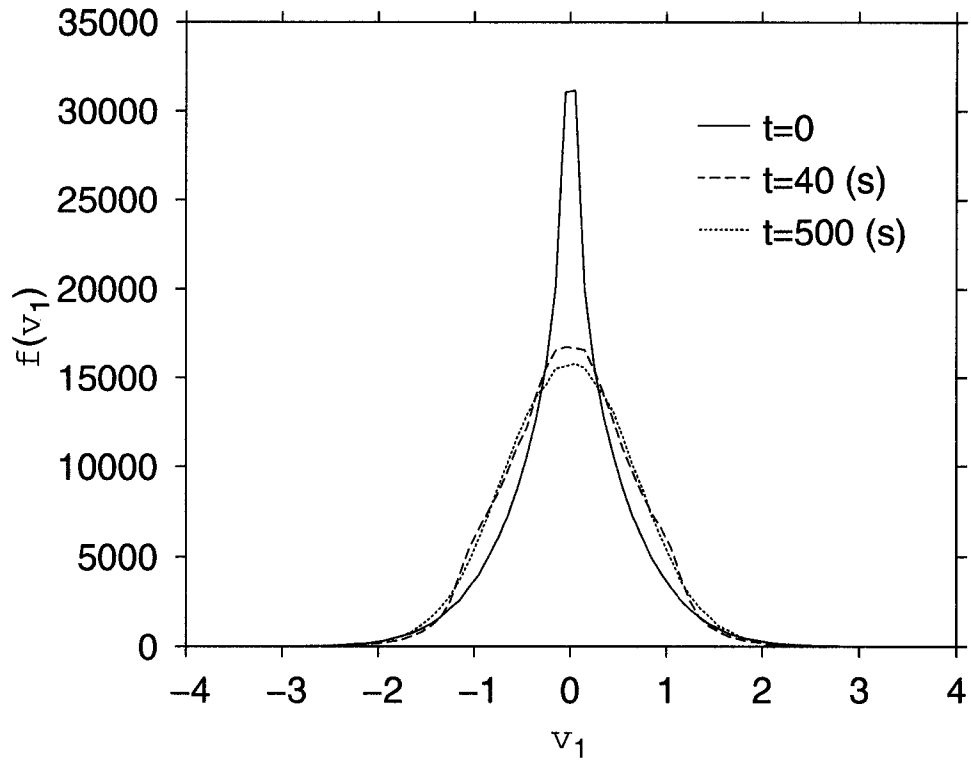
Figure 5.17: Evolution of the distribution function for the case of T_e=1.0 eV.
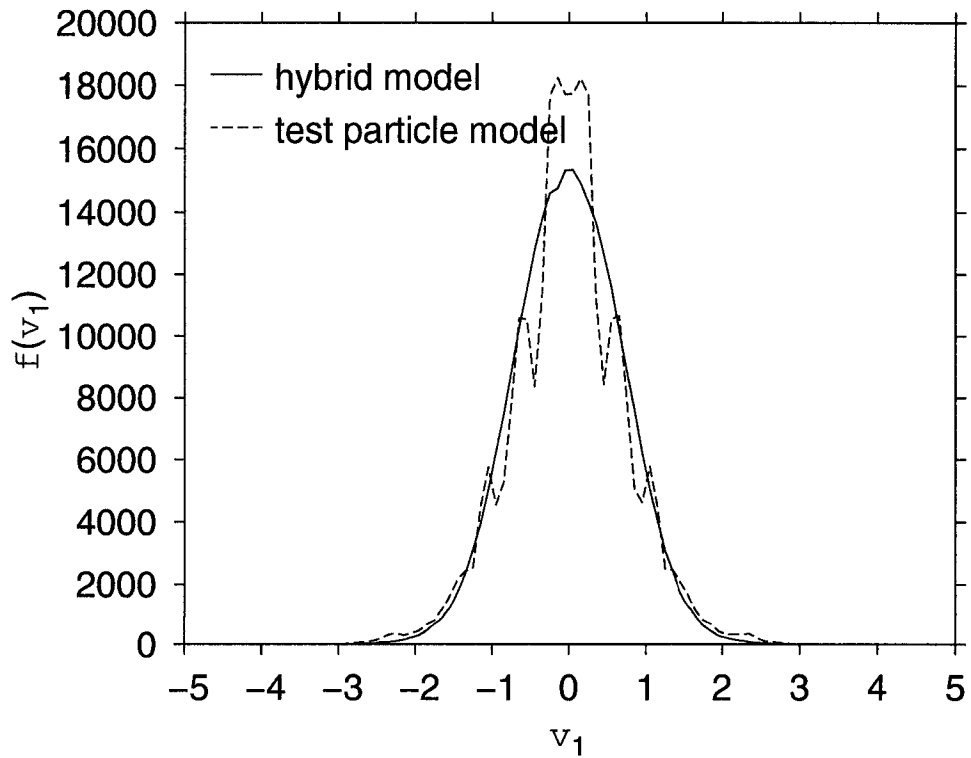
Figure 5.18: Contrast of distributions functions from the hybrid (solid line) and test particle models (dashed line) for T_e=1.0 eV at t=400 s.

97
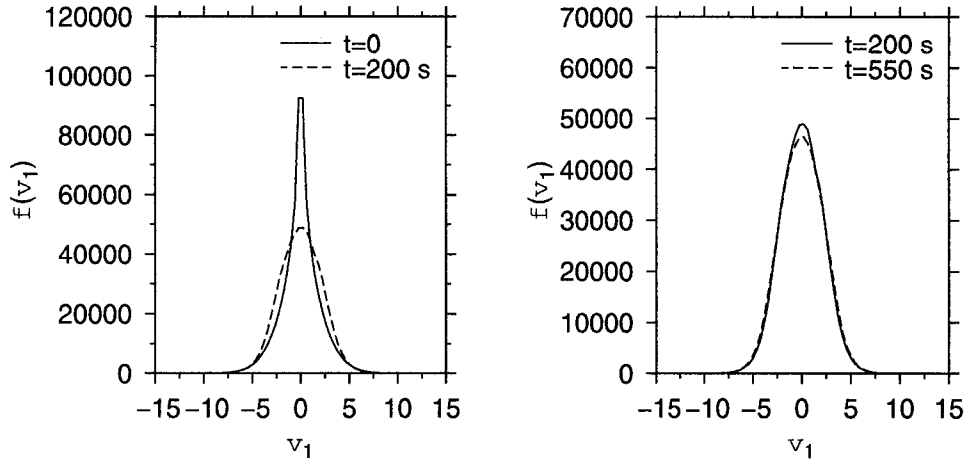
Figure 5.19: Evolution of the distribution function for the case of $T_e = 10.0$ eV.
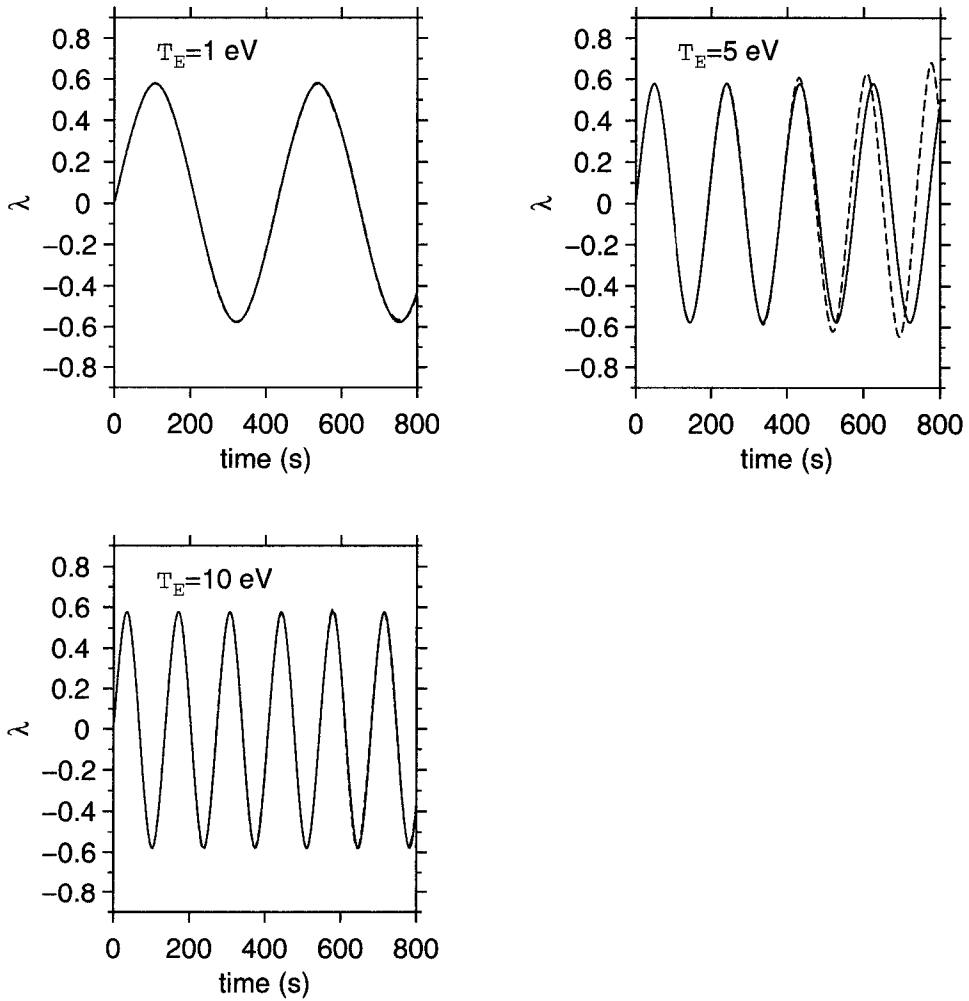
Figure 5.20: Trajectories of electrons of indicated energies with (solid line) and without resonance electric field (dashed line). All electrons are released at the equator of the L=10 magnetic field line with equatorial pitch angles of $\frac{\pi}{6}$.

98
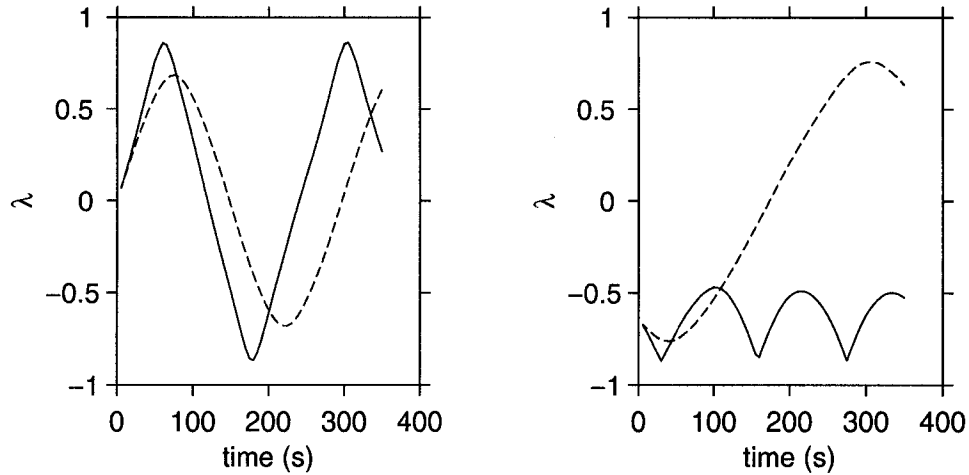
Figure 5.21: Comparison of trajectories for the hybrid model (solid line) and the test particle model (dashed line) for two different initial simulation electrons.

the electron distribution function at their respective ionospheres for both cases. The slightly different frequency for the resonance introduced by moving the ionospheric boundaries to 3 R_E is most clearly evident in the top frame for u_3. As would be expected, the increased curvature significantly enhances the current and pressure moments in this case as well. The initial μ_M moment of the electron distribution function is lower in this case because the increased magnetic field strength lowers the average magnetic moment value for the distribution, but the gradual increase of the value over time is suggestive of redistribution of electrons with larger magnetic moments towards the ionospheric region over time. In addition, over time, the ionospheric value of the pressure moment is increasing in the 3 R_E case.

Figure (5.23) illustrates the distribution function in the $3R_E$ case and there appears to have been some slight resonant heating of the electrons over time. This (along with the increase of the pressure and μ_M moments) may or may not be physical. The model can experience numerical heating in certain cases as will be highlighted in section 5.7. Further verification simulations need to be conducted to elucidate the trends noted here.

In order to put perspective on the length of these runs, it is worth noting that the simulation with $r_{ionophere} = 3\ R_E$, using 6 million simulation electrons and a time step of 0.0025 seconds, took about 10 days using 24 processors on an SGI Origin 2000. The grid used had 128 points in the x_2 direction and 64 points in the x_1 direction.

5.6 Inertial Alfvén wave and thermal plasma limits

Thus far, even though the simulations have been in the cold plasma limit, the electron inertial scale lengths have been too small for the resonance to narrow too in a reasonable amount of time. A much enhanced inertial length can be achieved by relocating the reso-

99
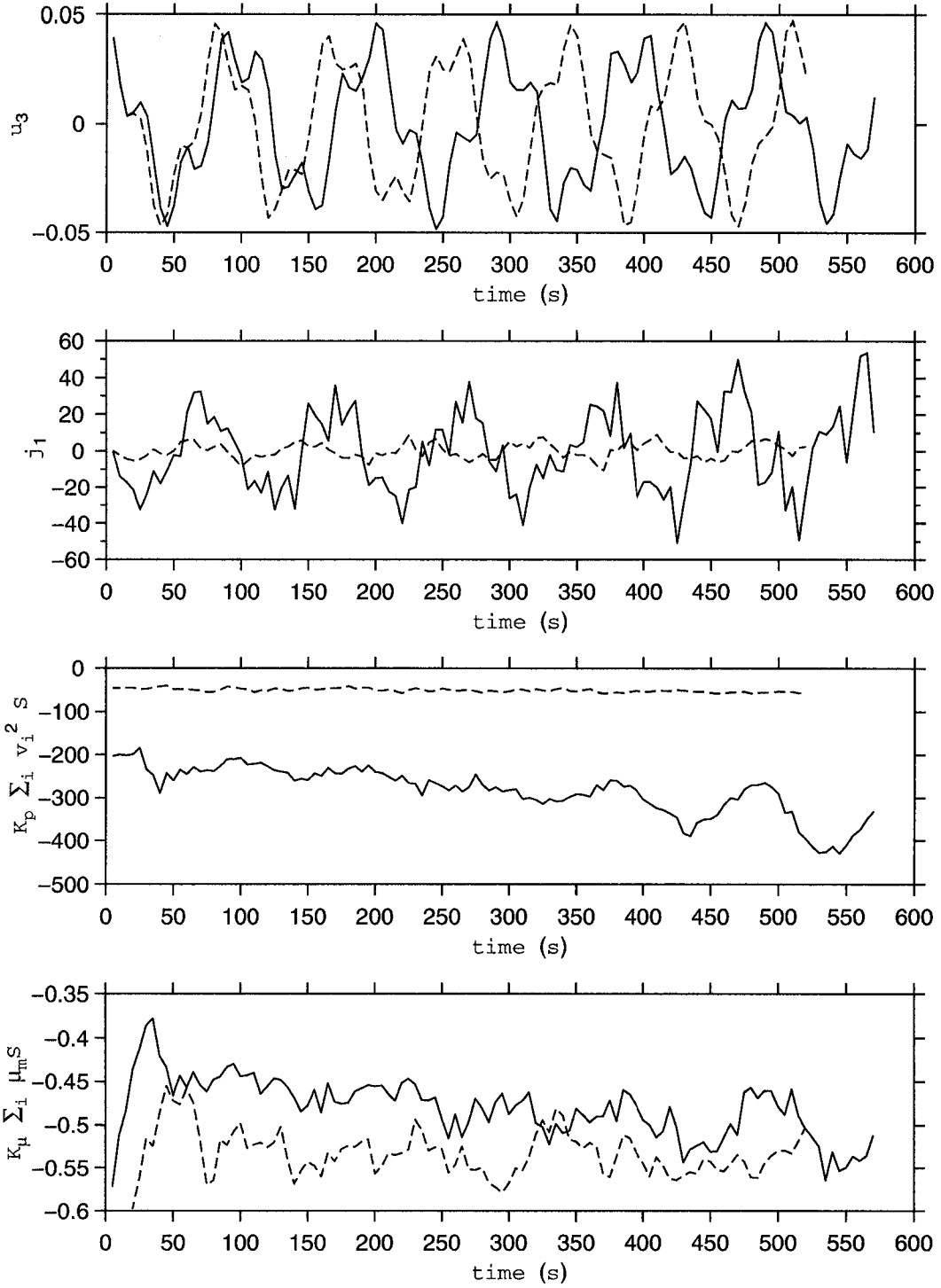
Figure 5.22: Four parameters as a function of time for the $T_e = 1.0$ eV simulations with ionospheres at 3 R_E (solid line) and 5 R_E (dashed line). Parameters plotted (from top to bottom) are the equatorial fluid velocity, u_3 and southern ionospheric values of the parallel current, j_1, pressure moment, $K_p \sum_i v_i^2 S$ and μ_M moment, $K_p \sum_i \mu_M S$ of the electron distribution function. K_p and K_μ are the normalization constants for each term (see section 5.8 equations).

100
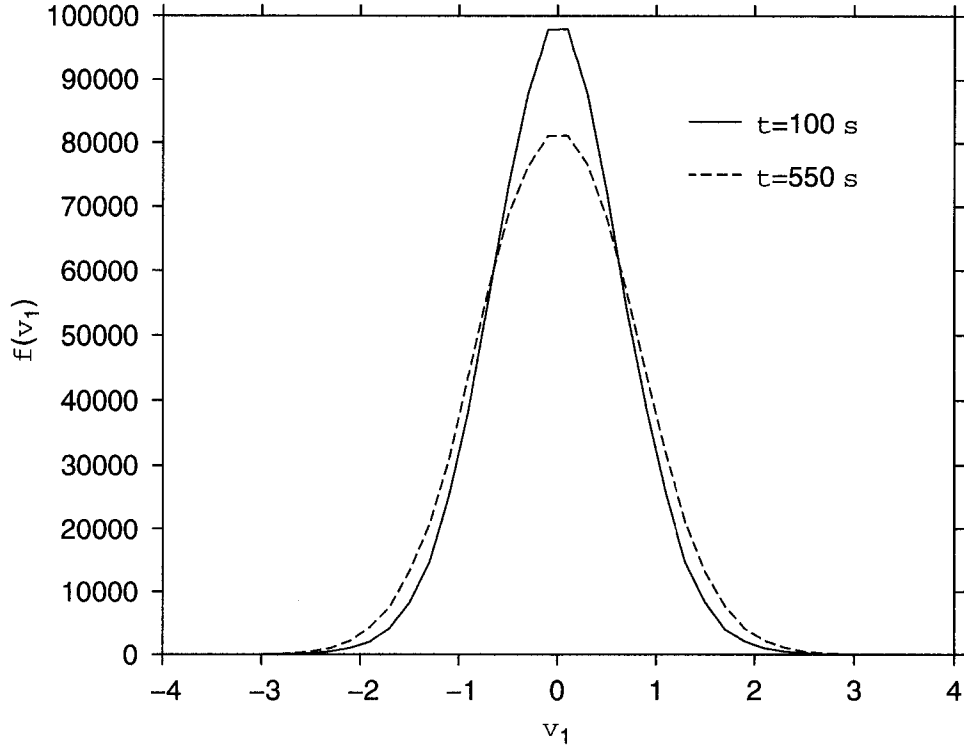
Figure 5.23: Evolution of distribution function for the simulation with $T_e = 1.0$ eV and $r_{ionosphere} = 3$ R_E.

nance closer to the earth as well as dropping the equatorial density. This has been done here to illustrate the formation of a inertial SAW in the cold plasma limit as well as the divergence between the MHD and the hybrid model for thermal plasmas ($v_{th} \approx V_A$).

For the simulations to follow, the resonance has been relocated at 6 R_E and the equatorial number density has been dropped to 0.05 cm^{-3}. The resulting radial Alfvén speed and electron inertial length at the equator are displayed in figure (5.24). Two simulations were then conducted for initial Maxwellian distributions functions with $T_e = 10$ eV and $T_e = 70$ eV (see figure 5.25). Comparison of this figure with (5.24) illustrates that these distribution functions represent approximately $v_{th} \ll V_A$ and $v_{th} \approx V_A$ respectively in the equatorial plane. Significantly larger temperatures can be considered here relative to the last sections because the field line is much shorter and consequently fewer simulation electrons are needed to adequately cover the simulation region. The ionospheres are located at 3 R_E.

The equatorial Shear Alfvén velocity profile at $t = 96$ seconds for the 10 eV case is illustrated in figure (5.26) along with the cold plasma MHD results. The formation of an inertial SAW is clearly visible propagating in the direction of increasing Alfvén wave speed and the hybrid and MHD models are in very good agreement. In the $T_e = 70$ eV case, on the other hand, (figure 5.27) there is an evident divergence from the cold plasma MHD. No longer is there any propagation in the direction of increasing Alfvén wave speed in the

101
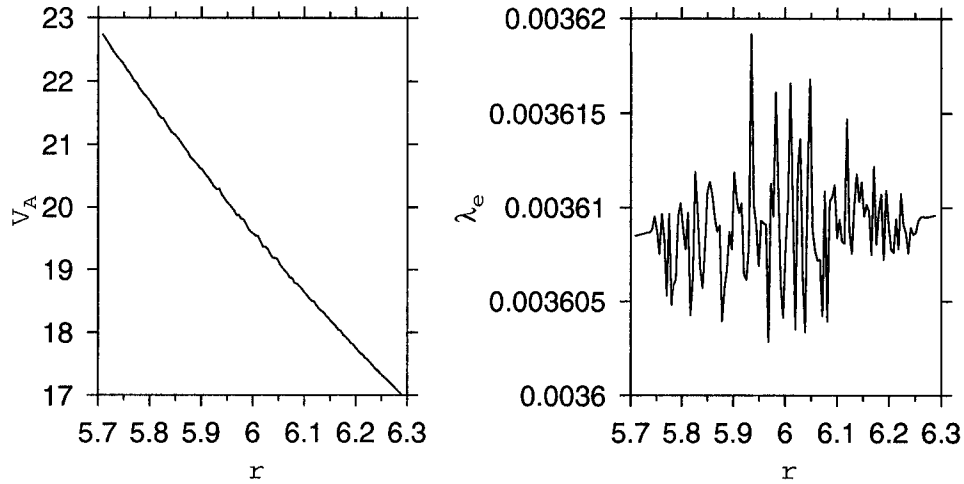
Figure 5.24: Radial Alfvén velocity and electron inertial length profiles (in nondimensional units) at the equator for $r_r = 6\ R_E$ and $n_{eq} = 0.05\ cm^{-3}$

hybrid case as would be expected for a thermal plasma. Propagation in the other direction of a kinetic Alfvén wave would be expected in the $v_{th} \gg V_A$ limit.

These results are consistent with the box model results with the exception that there is no measurable damping as compared to the MHD case and the distribution functions are unmodified due to Landau trapping. This is because the distribution functions are simply too cold. In the case of the changing field aligned Alfvén wave profile, the phase velocity of the SAW is a function of the integrated Alfvén wave speed along the field line, rather than the local value of V_A. Taking the approximate frequency of this resonance at about 7 seconds and the length of the field line (10.2 R_E), the ratio $\frac{\omega}{k_\parallel}$ for a fundamental mode FLR is 26.9 in nondimensional units. This is approximate since the initial Gaussian profile is only close to a fundamental mode eigenfunction. However, it is close enough for comparison and examination of figure (5.25) illustrates that even the $T_e = 70\ eV$ distribution is too cold to experience Landau damping effects. The strength of this potential damping has yet to be examined.

5.7 Boundary Issues

As indicated earlier, the model can experience artificial numerical heating of the electron distribution function. This is clearly evident in a couple of simulations conducted for an initial electron distribution function with $T_e = 4\ eV$ and an equatorial number density of $n_{eq} = 1.0\ cm^{-3}$ using first 2×10^6 and then 6×10^6 simulation electrons. There is fairly dramatic heating in the former case (top panel) but very little in modification in the latter (bottom panel). This is most probably related to fluctuations that develop at the ionospheric boundaries when there are an insufficient number of particles to adequately smooth out the particle distribution function moments. These fluctuations can then introduce gradients

102
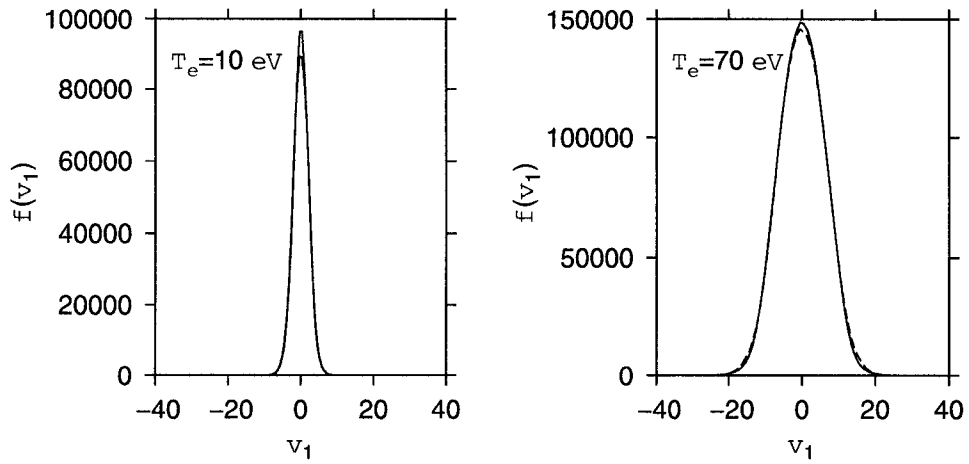
Figure 5.25: Distribution functions at $t = 24$ seconds (solid line) and $t = 96$ seconds (dashed line) for the inertial SAW example (left) and the kinetic Alfvén wave example (right).
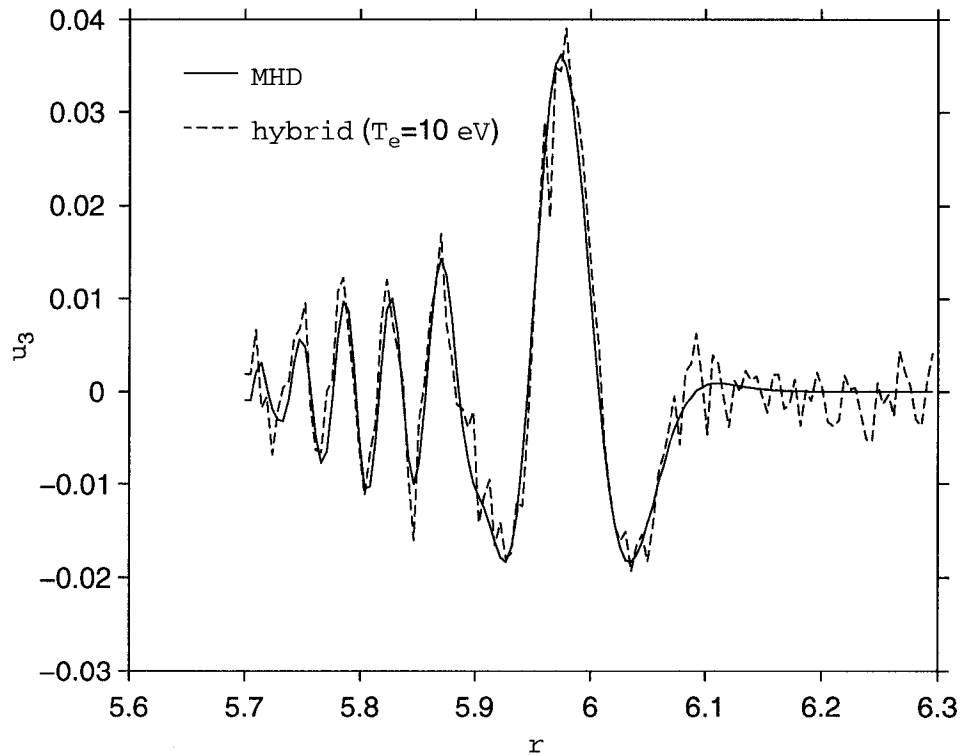
Figure 5.26: Comparison of the equatorial Shear velocity at $t = 96$ seconds (check time) for the cold plasma MHD model (solid line) and the hybrid model for $T_e = 10$ eV.

103
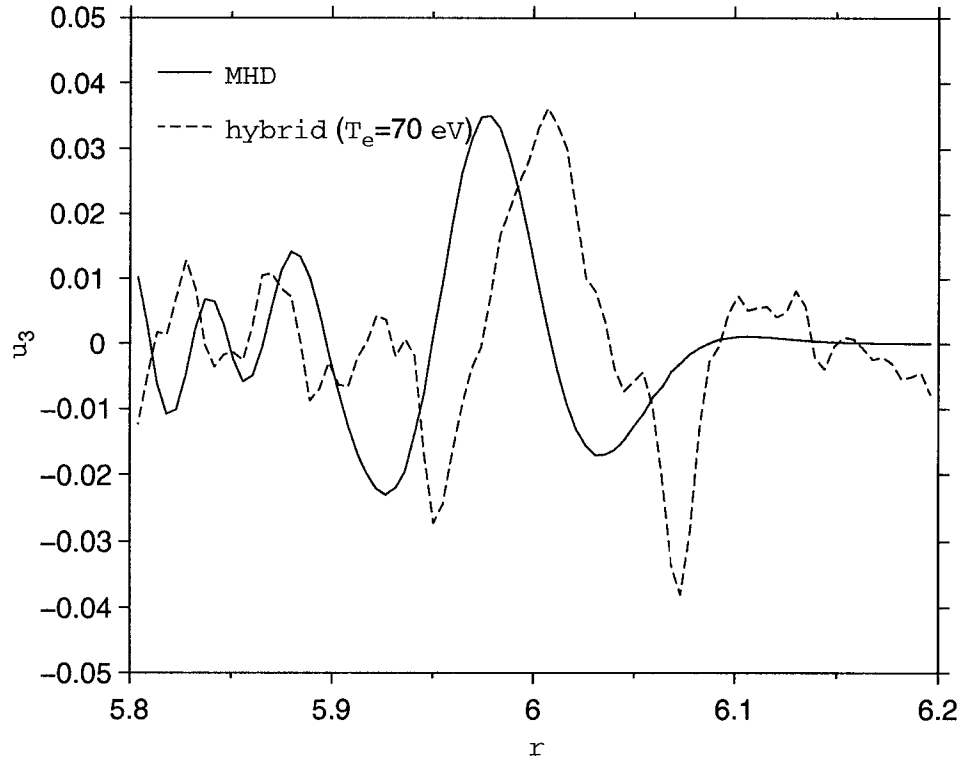
Figure 5.27: Comparison of the equatorial Shear velocity at $t = 100$ seconds (check time) for the cold plasma MHD model (solid line) and the hybrid model for $T_e = 70$ eV.

into the parallel electric field calculations and numerically enhance the results which in turn heats the particles, creating more noise and a sort of feedback loop results. This artificial enhancement in the pressure moment in the $n_p = 2 \times 10^6$ case relative to the $n_p = 6 \times 10^6$ case is evident in figure (5.29). Given enough time, the result of the numerical enhancement of the parallel electric field is to accelerate all the electrons into the ionospheric regions, evacuating the rest of the simulation grid and causing the simulation to crash. Therefore, increasing particle number is a fundamental test in interpreting any results from the model. The model seems most sensitive to this when higher equatorial densities are used and thus the $n_{eq} = 1.0$ cm^{-3} case was used to highlight this issue. As well, the effect is stronger with ionospheric boundaries closer to the earth and so this has been the main obstacle in trying to conduct simulations with ionospheres below $3R_E$. For example, initial simulations with the ionospheres at $2R_E$ using 7 million simulation electrons illustrated significant heating very early in the evolution of the system.

5.8 Parallel Electric Fields in the constant parallel density case

In Chapter 4 for the box model results, it was illustrated how difficult it is to clearly see the parallel electric field. This is more so the case in the dipolar model which is intrinsically

104
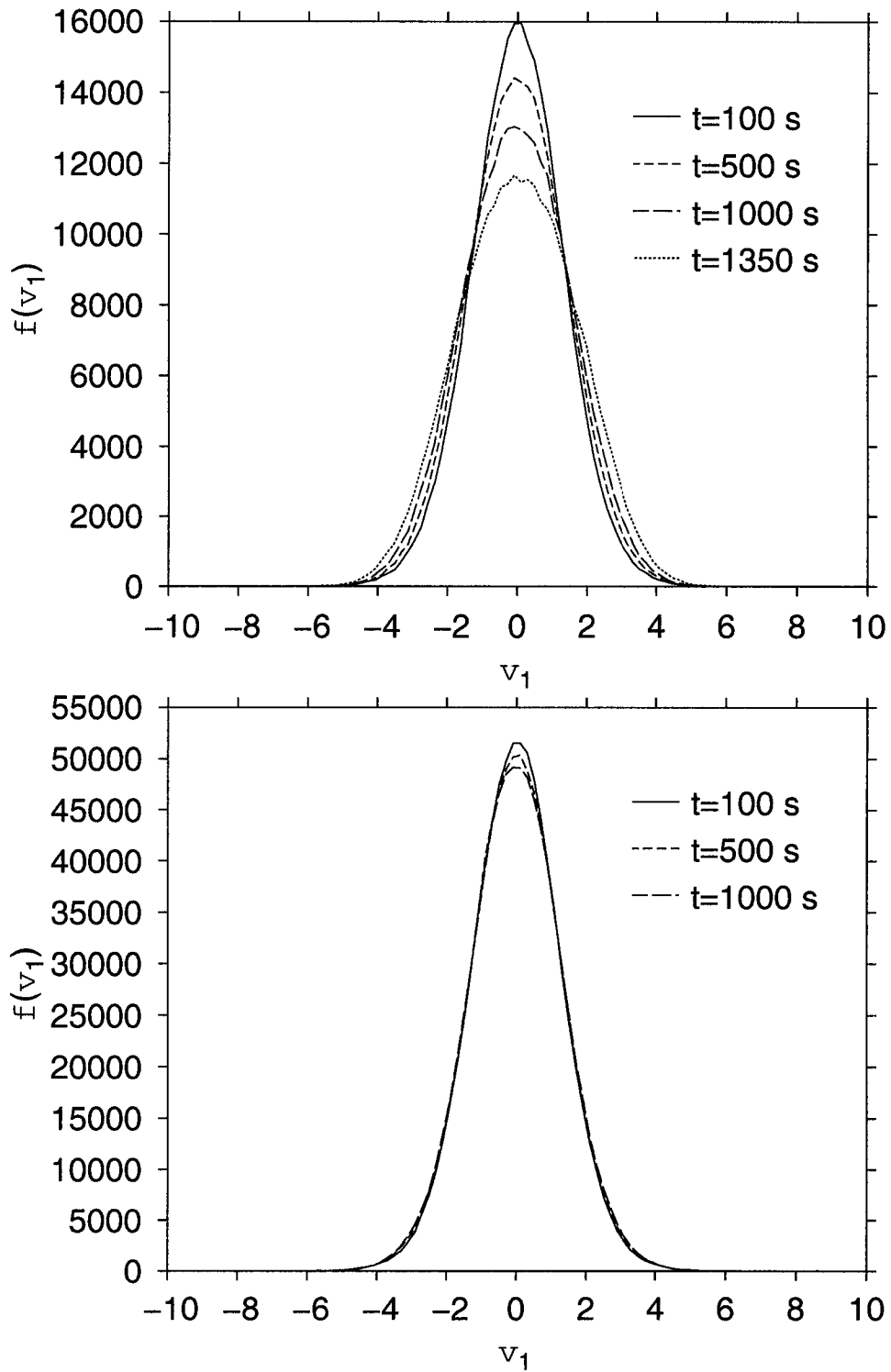
Figure 5.28: Distribution function evolution for the hybrid model with T_e=4.0 eV and $n_e = 1.0 \ cm^{-3}$ using 2 million particles (top) and 6 million particles (bottom).

105
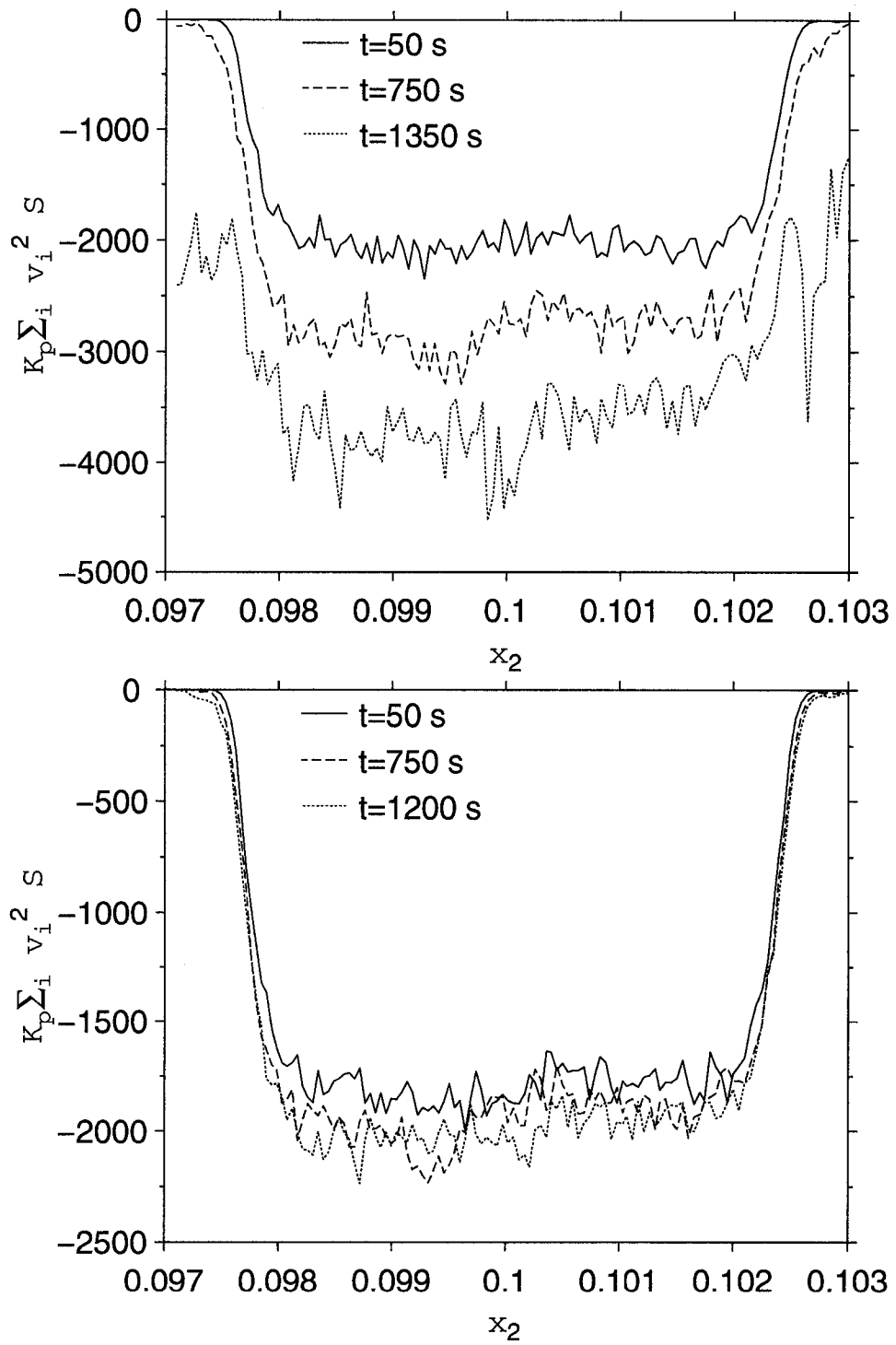
Figure 5.29: Evolution of the pressure moment, $K_p \sum_i v_i^2 S$ as a function as a function of x_2 (at southern ionosphere) for the hybrid model with $T_e = 4$ eV using 2 million particles (top) and 6 millions particles (bottom).

106

noisier because of the approximation used in the particle interpolation as well as the present lack of filtering in the model. In addition, the spatial integration done to obtain E_{2c} directly in the dipolar model, introduces a significant amount of noise and may indeed be the largest contributer.

As with the box model case though, the parallel electric field can be seen for very cold distributions. In this section the MHD result for E_1 is contrasted to the hybrid model results for several such distributions. As well, a comparison of the magnitudes of the source terms in the expression for E_1 is made. This will be done for a constant field aligned density distribution since the electric fields are significantly enhanced over the density profile considered thus far. The constant density case was not originally used, because along with the enhanced electric field, there are large density fluctuations in the ionospheric regions that get larger with time and lower altitude. The density depressions that form get large enough to violate the linear approximation that the code is based on. With regards to the electrons, this linear approximation comes via the fact that the Alfvén velocity and electron inertial length profiles are fixed at $t = 0$ from the initial electron distribution and then are not modified. With large fluctuations in the electron density this approximation is unreasonable and therefore long term simulations with a constant density profile are unrealistic with the model in its present configuration. As is, the evolution of the simulations is to create larger and larger density depressions at the ionospheres which eventually causes the program to crash when the electron number density drops to zero.

Since the equation for the parallel electric field is being referenced in this section, it is useful to rewrite it here. In nondimensional form, it is given by

$$
\begin{aligned}
\frac{1}{h_2 h_3}\frac{\partial}{\partial x_2}\left(\frac{h_3}{h_1 h_2}\left(\frac{\partial G}{\partial x_2}\right)\right) - \frac{G}{h_1 \lambda_e^2} \; = \; & \frac{1}{h_2 h_3}\frac{\partial}{\partial x_2}\left(\frac{h_3}{h_1 h_2}\frac{\partial}{\partial x_1}(h_2 E_2)\right) \\
& + \frac{1}{h_2 h_3}\frac{\partial}{\partial x_2}\left(\frac{h_3}{h_1 h_2}\frac{\partial}{\partial x_1}(h_2 E_{2c})\right) \\
& + \frac{K_\mu}{h_1}\frac{\partial B_o}{\partial x_1}\sum \mu_m S(\vec{x}, \vec{x}_i) \\
& + \frac{K_p}{h_1}\frac{\partial}{\partial x_1}\sum_i v_i^2 S(\vec{x}, \vec{x}_i)
\end{aligned}
$$

where as indicated in Chapter 3, $G = h_1 E_1$ and E_{2c} is the field resulting to enforce quasineutrality. The new variables, K_μ and K_p are the normalization constants for the magnetic moment and pressure terms respectively. Although they are treated separately in the program, these two variables are in fact numerically equal and are given by

$$
K_\mu = K_p = e\mu_o L \frac{v_N}{B_N}\frac{\rho_N}{m_p} \tag{5.10}
$$

where L is the normalization length and the N subscript denotes the normalization constant for the relevant variable. For simplicity of notation, the scaling factors evident in equation (3.65) have been omitted and the moments are assumed to already be scaled.

107

Before looking at the individual components though, figure (5.30) illustrates the radial profile of E_1 close to the southern ionosphere for the cold plasma MHD code and the hybrid model runs with three different cold initial electron distribution functions ($T_E = 0.001, 0.1$ and $1.0 \; eV$) at $t = 13$ seconds. In all cases, the resulting field is very close to the MHD case within the limit of the numerical noise. The increase in this noise with temperature is also evident. Figure (5.31) illustrates the electron density profile at the same position. Relatively large density fluctuations are already evident at this early time in the evolution of the system. For all the simulations, the parameters are the same as in the last section so the equatorial position of the resonance is still at 6 R_E and the ionopheres at an altitude of 3 R_E. The constant electron number density is 0.05 cm^{-3} and 4 million simulation electrons were used in each case. The period of this system is approximately 7 seconds.

Now, in order to illustrate how the different terms contribute to the final value of E_1, figure (5.32) presents the values of each of the four terms on the right hand side of equation (5.10) along the same radial slice at $t = 6$ seconds. To avoid complexity of notation, the terms are identified simply by referencing the relevant principal component (i.e. E_2 ,E_{2c}, μ_M or pressure-$\sum_i v_i^2 S$). Only the $T_e = 0.001$ eV and $T_e = 0.1 \; eV$ cases are illustrated in the top two panels because the $T_e = 1.0$ eV case was too noisy for the E_2 and E_{2c} fields. In all cases the results have been filtered (after the simulation) with the same digital filter as used in the box model. This is also true of the E_1 and n_e plots already presented. The results were presented at $t = 6$ seconds because the E_{2c} term becomes noisier and consequently more difficult to visualize at later times.

As is evident, the largest component is from the E_2 term and the correction field E_{2c} is relatively small, but can be of similar order of magnitude at times. It also seems to have similar dependence in the two temperature cases, but the noise increases with temperature most significantly in this term as compared to any other. The signal in the $T_E = 1.0$ eV case is completely drowned in noise and so it seems evident that most of the noise that gets transferred to E_1 is coming via the term for E_{2c}. The pressure term is close behind in magnitude but is not sufficiently large enough to effect the evolution. The shape of the profiles is sensitive to temperature, but it is not always the case that the $T_E = 1.0$ eV result is smallest. Finally, the value of the μ_M term is virtually insignificant for the present parameters but it does increase relatively dramatically as the temperature of the distribution increases. Therefore as expected, the contribution from the mirroring term grows with temperature. The increased curvature at lower altitudes will also add to this since the term incorporates the parallel gradient of the magnetic field.

In the $T_e = 1.0$ eV case, the simulation was continued and the result for the parallel electric field is displayed in figure (5.33) along with the MHD result at $t = 30$ seconds where they are still in good agreement in the inertial SAW limit. Additional simulations with T_e up to 3 eV have illustrated no significant divergence from the MHD result.

In order to further illustrate that these results are self consistent, it is possible to appeal

108
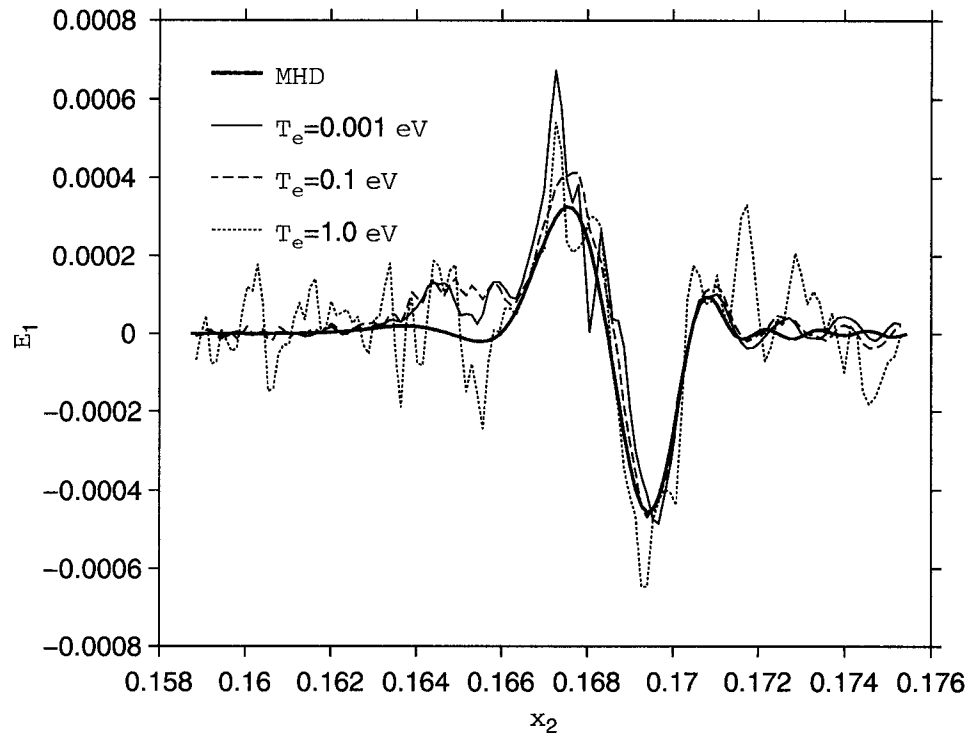
Figure 5.30: Radial profile of E_1 close to the southern ionosphere ($x_1 = -0.0573$) for the MHD model and the hybrid model with three different initial electron distribution functions at $t = 13$ seconds. A constant field aligned density profile was used with $n_{eq} = 0.1 \ cm^{-3}$.
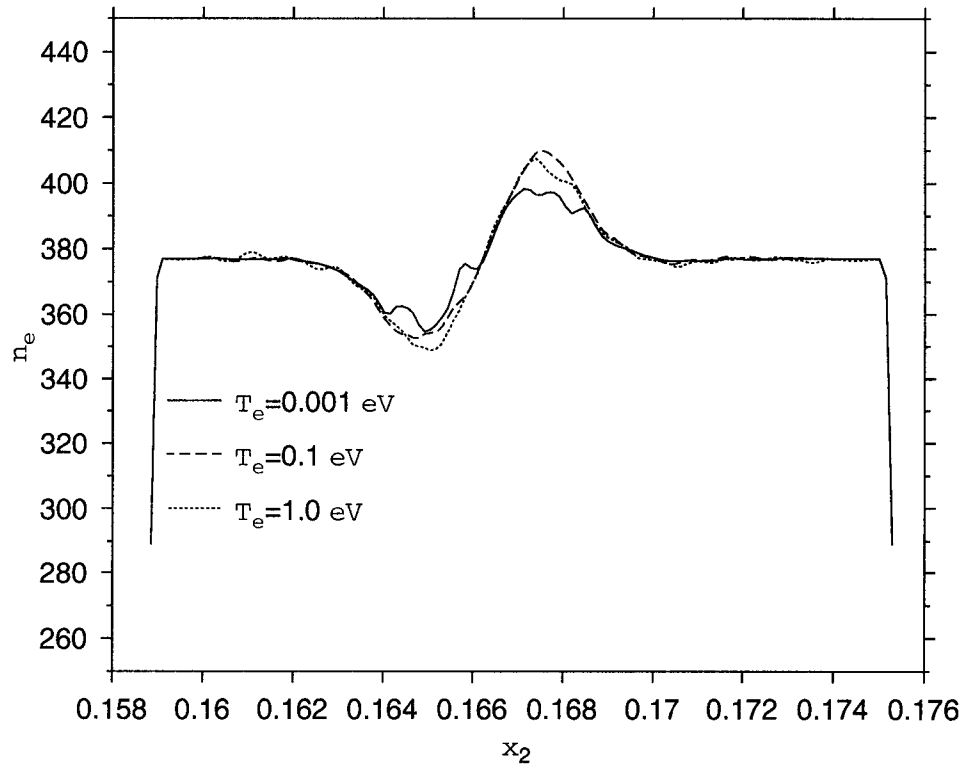
Figure 5.31: Radial profile of n_e close to the southern ionosphere ($x_1 = -0.0573$) for the MHD model and the hybrid model with three different initial electron distribution functions at $t = 13$ seconds.

109
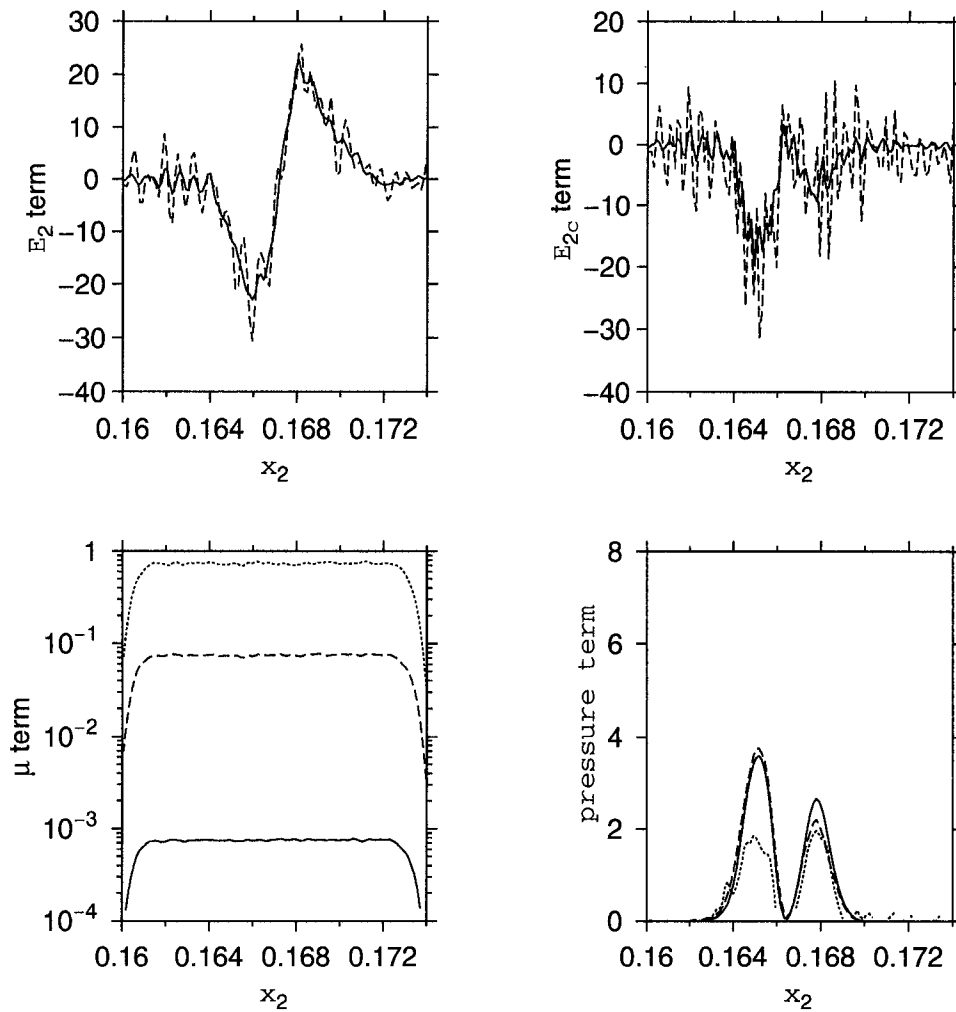
Figure 5.32: Radial profiles of the components of the equation for E_1 close to the southern ionosphere ($x_1 = -0.0573$) at $t = 6.0$ seconds for $T_e = 0.001$ eV (solid line), $T_e = 0.1$ eV (dashed line) and $T_e = 1.0$ eV (dotted line). This last case is not displayed in the top two panels as it was too noisy.

110
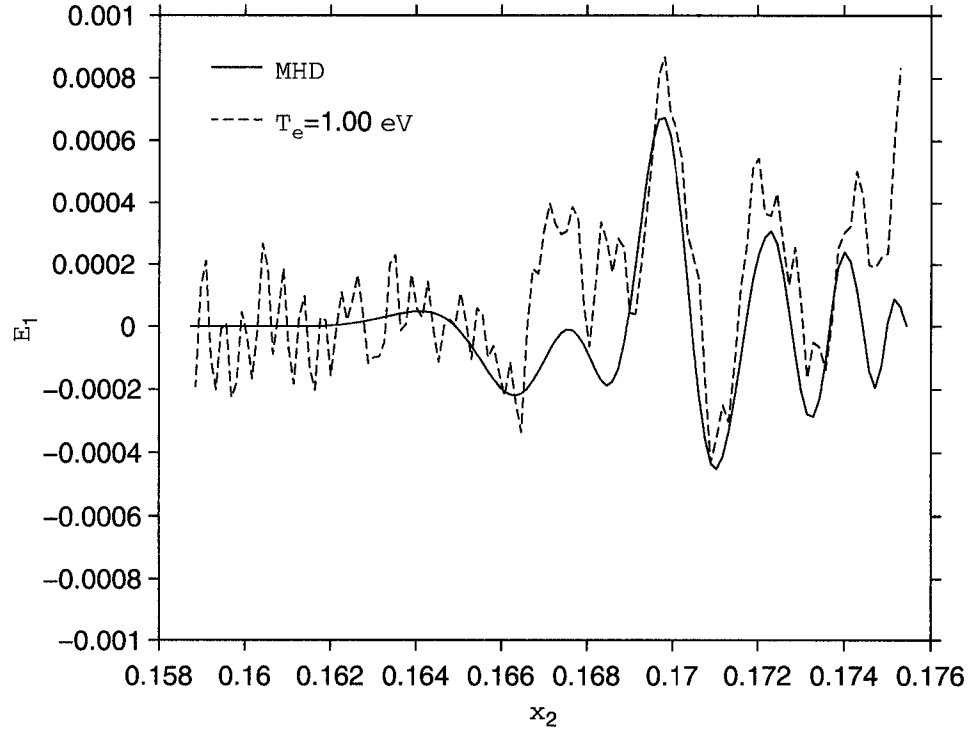
Figure 5.33: Radial profile for E_1 close to the southern ionosphere ($x_1 = -0.0573$) for the MHD model and the hybrid with $T_e = 1.0$ eV at $t = 30$ seconds.

to a simple argument to see what particle energies are needed to carry this current. As stated in Chapter 3, the current density is given by $|j_1| = |ne\overline{v_\parallel}|$. Therefore by taking the parallel current density from the simulation and using the value of $n = 0.05cm^{-3}$ it is trivial to calculate the average electron energy needed to support the j_1 as a function of position along the field line. This is presented in figure (5.34) where the top panel displays the current slice along the field line (southern ionosphere) and the bottom panel illustrates the corresponding calculated average electron energy. As is clearly evident, very low electron energies on the order of $0.1 - 1$ eV are needed to support the ionospheric parallel current density and much less for higher altitudes. Therefore it is not surprising that significant electric fields are not observed to accelerate the electrons to sufficient velocity. As well, it is worth noting that the maximum values of j_1 noted in any of the hybrid simulations considered in this chapter are on the order of 10^{-2} $\mu A/m^2$.

As a comparison, the same calculation was done for ionospheres at an altitude of 1 R_E. The results are displayed in figure (5.35) and it is clearly evident that electron energies of hundreds of eV are needed to support parallel currents on the order of $10^{-1} - 1$ $\mu A/m^2$. Although this situation is unrealistic as density increases along the field line, very low densities can be found in ionospheric density cavities and and consequently the calculation is relevant. Observations (and other simulations) tend to produce field aligned current densities on orders up to a few tens of $\mu A/m^2$ which, in the presence of low enough densities,

111

may need keV electrons to support the current. Extending the code to work in the $\mu A/m^2$ range will be the main focus of future research.
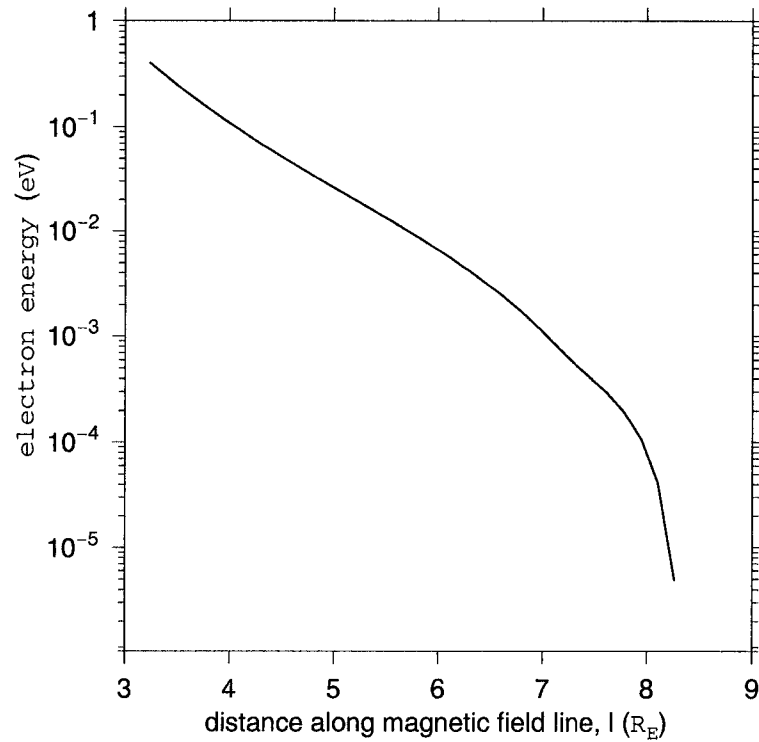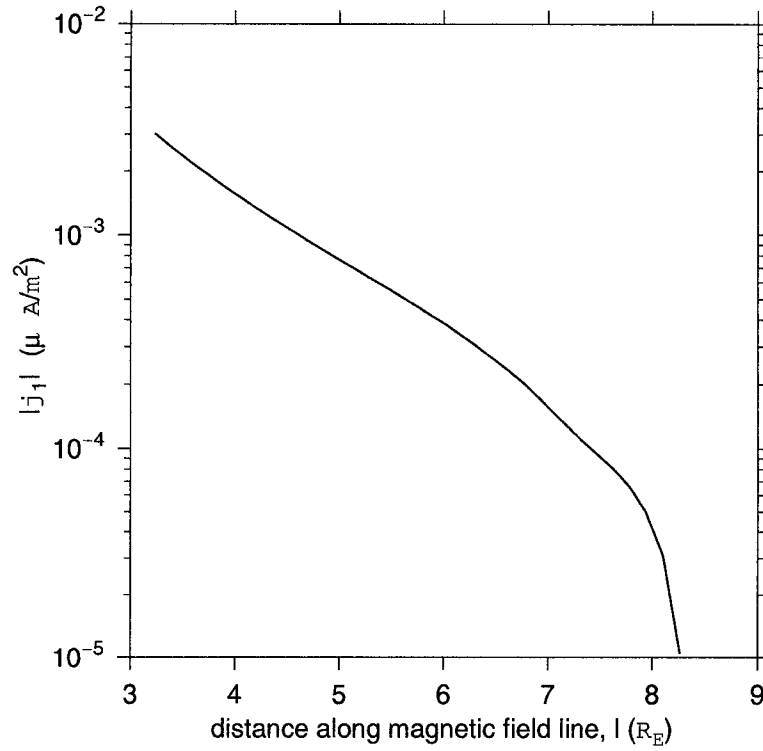
Figure 5.34: Average electron energies needed to support the current density j_1 in the top panel for a constant electron number density profile of 0.05 cm^{-3}. Calculation based on the definition $|j_1| = |ne\bar{v}|$. Current density profile is for the MHD simulation at $t = 1$ s along $x_2 = 0.165$ field line with $r_{ionosphere} = 3\ R_E$.

113
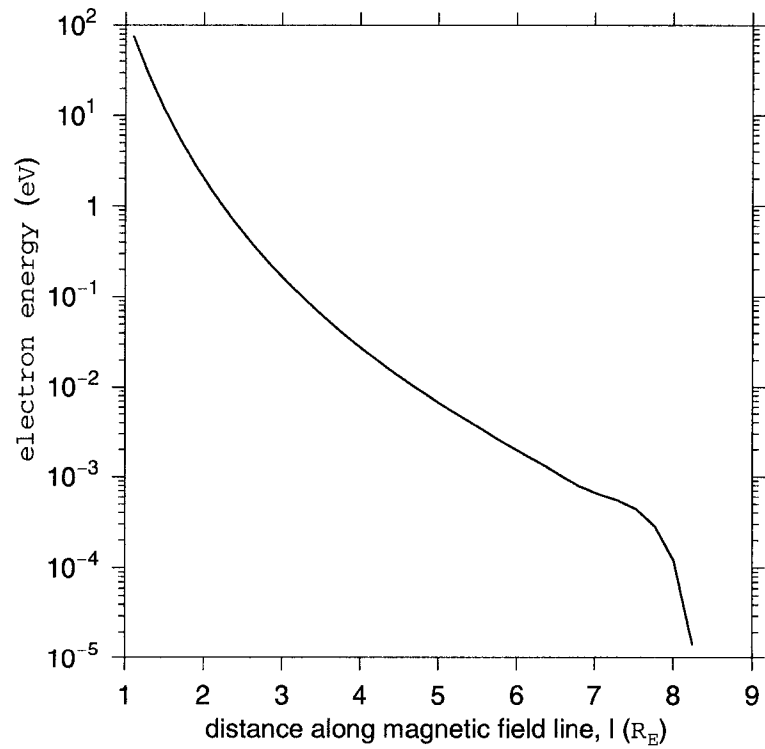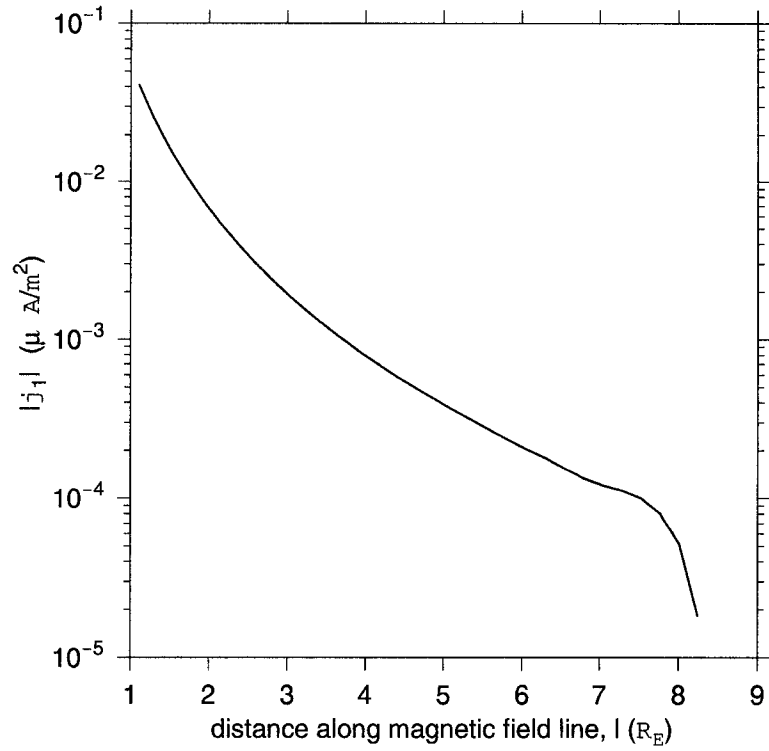
Figure 5.35: Average electron energies needed to support the current density j_1 in the top panel for a constant electron number density profile of 0.05 cm^{-3}. Calculation based on the definition $|j_1| = |ne\bar{v}|$. Current density profile is for the MHD simulation at $t = 1$ s along $x_2 = 0.165$ field line with $r_{ionosphere} = 1$ R_E.

114

5.9 Summary

In this chapter, the results of both the 2D cold plasma MHD model and hybrid model in dipolar coordinates were illustrated. In both cases, the perfectly conducting boundary conditions were used at the ionospheres. In the case of the cold plasma MHD model, the following was illustrated.

- In the $\lambda_e = 0$ case, the model results were in good agreement with a nonlinear MHD simulation in the cold plasma and low temperature limit. The only significant difference was an expected frequency shift in the nonlinear case.

- For the case of $\lambda_e = 0$ the formation of an inertial SAW propagating in the direction of increasing Alfvén wave speed was illustrated. The parallel electric field magnitude was consistent with other simulation results in that it was several orders of magnitude below the observed mV/m range. This again confirms the failure of MHD theory to properly account for the observed parallel electric field.

For the hybrid model simulations, the following results were obtained.

- The hybrid model agreed very well with the cold plasma MHD results in the cold plasma limit including the formation of an inertial SAW.

- In the thermal plasma case, the hybrid model diverged from the cold plasma MHD case as would be expected. Landau trapping effects were not noted as the distribution function was still too narrow.

- The parallel electric field agrees with MHD results for cold plasmas at altitudes above 3 R_E along the magnetic field line. For all density profiles considered, the maximum ionospheric current density is on the order of 10^{-2} $\mu V/m^2$ and populations of cold electrons are sufficient to carry the needed current. This agrees with an order of magnitude calculation based on the definition of $|j_{||}| = |ne\overline{v_{||}}|$ and is consistent with the work of Rankin et al. (1999).

Therefore, although there are significant problems to be addressed in the dipolar code in terms of resolving the parallel electric field and handling the boundaries in a more robust way, the method has been illustrated to be sound. The results are consistent with the cold plasma MHD when $v_{th} \ll V_A$ and diverge as would be expected in the thermal plasma limit. Given time, the approach should prove a useful tool in helping to study how wave-particle interactions affect parallel electric field generation in FLRs.

5.10 Erratum

Subsequent to the defence of this thesis, it was noted by the author that the normalization constants, K_μ and K_p, were given the incorrect sign stemming from an error incorporating

115

the negative sign within the charge variable "e". Both quantities should in fact be positive. Due to the small magnitude of the pressure and magnetic moment contributions to the parallel electric field, it is not believed that this error significantly effects the results of this chapter. As a check, the simulations used within figure (5.32) were redone with the corrected program and the results are shown in figure (5.36). They are quantitatively similar to those in the original figure with the exception of the sign in the bottom two panels. Also, the E_{2c} term is smaller and less noisy. It is uncertain as to why the magnitude is reduced, but it may be partially numerical and partially a response to the change in sign of the other terms. The net effect on the resulting parallel electric field is negligible however as is evident in figure (5.37) where there is no sigficant divergence from the MHD field. Therefore the final interpretation is the same. The reduced noise is due to the fact that although the same number of particles were used in this simulation, the radial simulation range was somewhat reduced giving better resolution.

Due to the time constraints for the submission of the thesis, it was not possible to redue all the simulations to their full extent, but initial trials show that the only major effect is to change the sign on the pressure and magnetic moment terms. The simulations remained otherwise unmodified. Therefore, within the chapter this would manifest itself most significantly as a change in sign in the bottom two panels of figure (5.22) and the same for the both panels of figure (5.29).
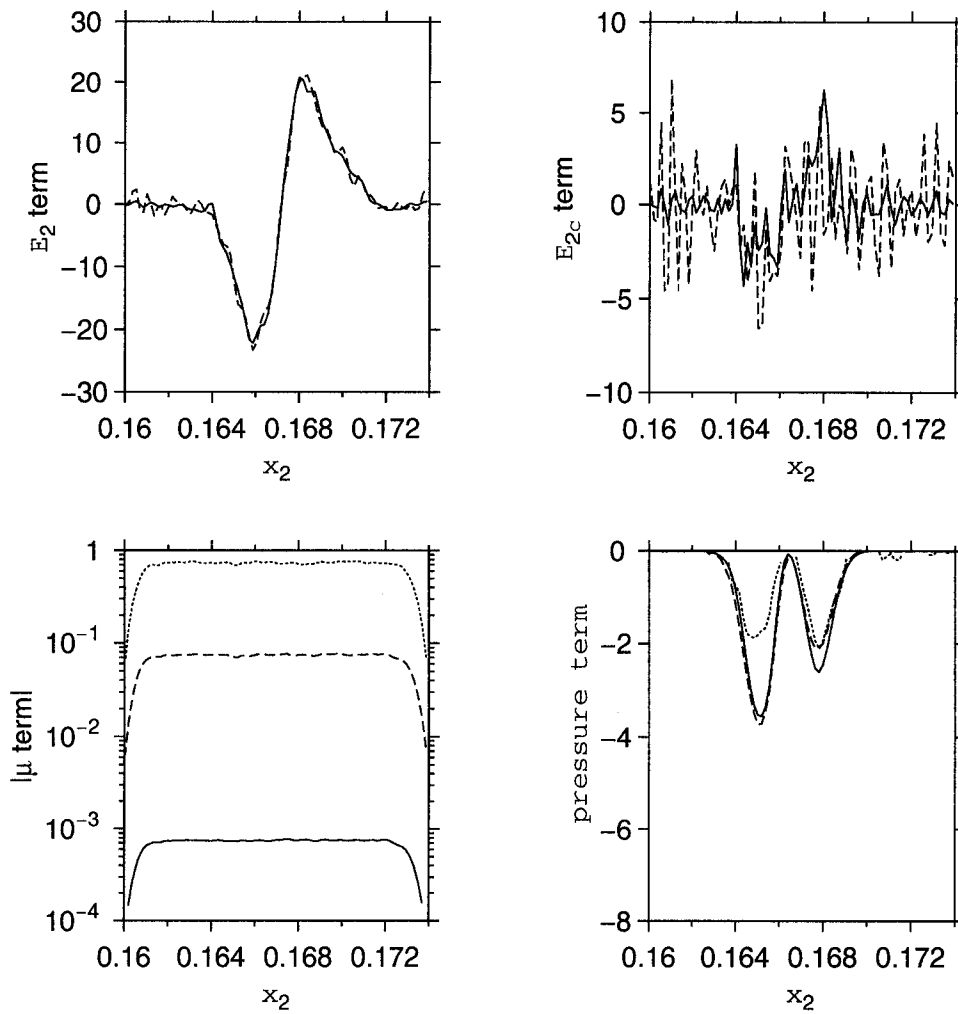
Figure 5.36: Radial profiles of the components of the equation for E_1 close to the southern ionosphere ($x_1 = -0.0573$) at $t = 6.0$ seconds for $T_e = 0.001$ eV (solid line), $T_e = 0.1$ eV (dashed line) and $T_e = 1.0$ eV (dotted line). This last case is not displayed in the top two panels as it was too noisy. Calculation done with corrected program.

117
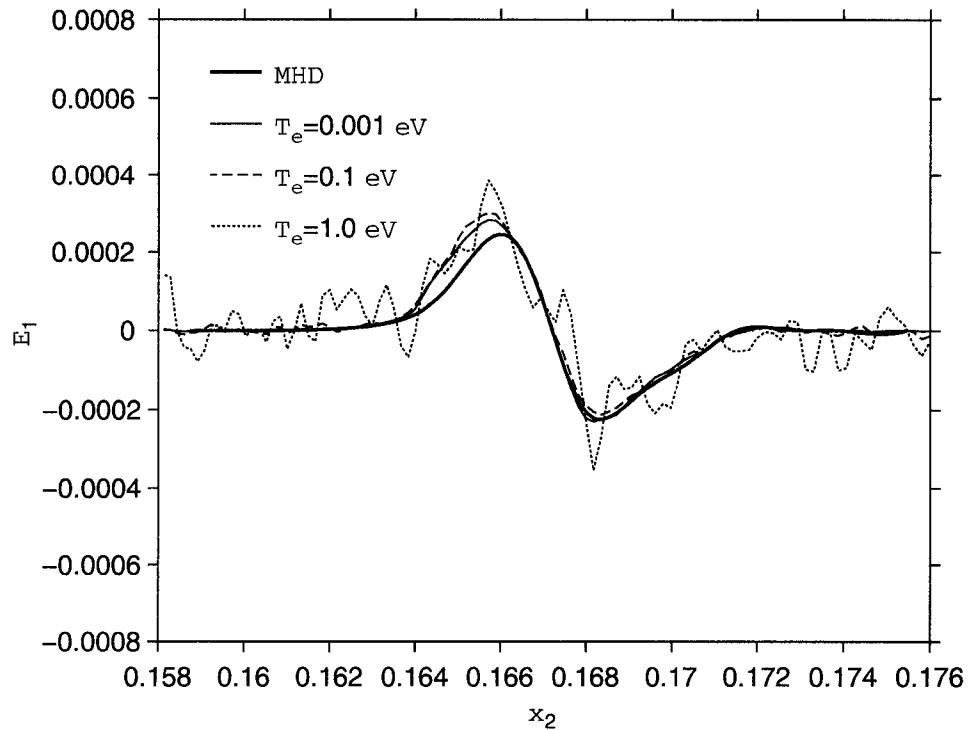
Figure 5.37: Radial profile of E_1 close to the southern ionosphere ($x_1 = -0.0573$) for the MHD model and the hybrid model with three different initial electron distribution functions at $t = 6$ seconds. A constant field aligned density profile was used with $n_{eq} = 0.1$ cm^{-3}. Calculated with the corrected program.

Chapter 6

Conclusions

In this work we have developed a self consistent hybrid MHD-kinetic model for studying wave-particle interactions in FLRs, but the model is applicable to any system with Shear Alfvén waves as long as the minimum scale length is above the ion gyroradius. The model consists of the cold plasma MHD equations and the guiding center equations for the electron dynamics and it has been successfully developed and illustrated to work in both cartesian and dipolar coordinate systems.

In the first part of the thesis, the model was developed in a box geometry with a constant ambient magnetic field for both periodic and perfectly conducting boundary conditions. The plasma density and Alfvén velocity were constant in the field aligned direction with gradients in the radial direction. For cold initial electron distribution functions, $v_{th} \ll V_A$, the hybrid model results were shown to be in good agreement with the cold plasma fluid code. For warmer distributions, $v_{th} \geq V_A$ there was significant Landau damping of the standing Shear Alfvén wave system. The damping rate was shown to be in good agreement with that predicted by the analytical dispersion relation developed from the cold plasma equations and electron drift kinetic equation.

As discussed in the opening chapter, the converging magnetic field inherent in the dipolar geometry is fundamental in the study of wave-particle interactions in FLRs and so the last part of the thesis was devoted to developing the model in this geometry. Before presenting results for the hybrid model, comparisons were made in the cold plasma fluid limit with the nonlinear resistive MHD code (Voronkov et al., 1998) as a check that the code was working properly. It was further illustrated that the nonlinear frequency shift does not introduce significant differences in the phase mixing evolution of the resonance when looked at from the point of view of the number of periods.

For the dipolar hybrid model case, simulations were restricted to having the ionospheres at an altitude of 3 R_E due to noise issues at these boundaries which introduce numerical heating of the electron distribution function. Within this limit though and using cold initial electron distribution functions, good agreement was again shown with the cold plasma MHD results for both constant and changing field aligned density profiles. This included the

formation of an inertial SAW. In the thermal plasma case $v_{th} \approx V_A$, divergence between the hybrid and MHD systems was again illustrated. No Landau damping effects were noted in this case however, because the distribution functions considered are still too cold.

Due to statistical noise issues, clear observations of the parallel electric field have thus far been limited to the cold plasma regime where they have been consistent with the MHD results. Large enhancements due to wave-particle interactions would have been visible though, but none have been seen and neither has there been any significant changes to the initial electron distribution functions. This result is not surprising since the simulations have been restricted to regions above 3 R_E and the current densities evident here are only on the order of 10^{-2} $\mu A/m^2$ for most reasonable parameters. Electrons with energies in the eV range or less are sufficient to carry this current and so no significant modification of the electron distribution function is required. On the other hand, the fluid calculations have illustrated that field aligned current densities up to 1-10 $\mu A/m^2$ are evident at altitudes around 1-2 R_E (both in simulations and observations) and depending on the densities, electron energies up to the keV range may be needed to support this current. This combined with the fact that mirror force and pressure effects increase with temperature and curvature implies that wave-particle interactions should become more evident when stable simulations at lower altitudes are done. This suggestion is consistent with the results of Rankin et al. (1999) in that the significant jumps in the parallel electric field usually occurred in the range 2-3 R_E above the ionosphere (even in the absence of ionospheric density cavities).

In conclusion, a new method for modeling of wave-particle interactions between electrons and SAWs has been introduced and shown to work properly in both box and dipolar geometries. Therefore the main goal of the thesis has been achieved. Thus far, no concrete comparisons can be made between this work and the nonlocal conductivity model (Rankin et al., 1999; Tikhonchuk et al., 2000) except that the lack of significant enhancements in $E_{||}$ below 3 R_E is consistent with these results. The main focus of the research from this point then is to conduct simulations with ionospheres in the 1-2 R_E range. Stability issues with the ionospheric boundaries below 3 R_E have been highlighted, but it is possible that these effects can be compensated for by increasing particle number and reducing the time step. Further work in progress to introduce a stable filtering algorithm to the model will also go a long way to resolve this. Therefore, the model stands in a good position to help elucidate the significance of wave-particle interactions to enhancing the parallel electric field in the limit of perfectly conducting ionospheres. In addition it may be possible to adapt the model to the fact that the ionospheres are not perfectly conducting by reintroducing boundary electrons in a way more self consistent with observed upward flowing electron distribution functions. This is desired as recent works have highlighted the significance of finite ionospheric conductivity in enhancing the parallel electric field (i.e. Samson et al., 1996).

Bibliography

[1] T.M. Antonsen and B. Lane. Kinetic equations for low frequency instabilities in inhomogeneous plasmas. *Phys. Fluids*, 23:1205, 1980.

[2] Wolfgang Baumjohann and Rudolph A. Treumann. *Basic Space Plasma Physics*. Imperial College Press, 1996.

[3] C.K. Birdsall and A.B. Langdon. *Plasma Physics Via Computer Simulation*. Adam Hilger, 1991.

[4] Joseph E. Borovsky. Auroral arc thickness as predicted by various theories. *Journal of Geophysical Research*, 98:6101, 1993.

[5] J. Busnardo-Neto, P.L. Pritchet, A.T. Lin, and J.M. Dawson. A self-consistent magnetostatic particle code for numerical simulation of plasmas. *Journal of Computational Physics*, 23:300, 1977.

[6] C.W. Carlson, R.F. Pfaff, and J.G. Watzin. The Fast Auroral SnapshoT (FAST) mission. *Geophysical Research Letters*, 25:2013, 1998.

[7] L. Chen and A. Hasegawa. A theory of long-period magnetic pulsations 1. Steady state excitation of field line resonance. *Journal of Geophysical Research*, 79:1024, 1974.

[8] T.E. Eastman, B. Popielawska, and L.A. Frank. Three-dimensional plasma observations near the outer magnetospheric boundary. *Journal of Geophysical Research*, 90:9519, 1985.

[9] F.R. Fenrich, J.C. Samson, G. Sofko, and R.A. Greenwald. ULF high- and low-m field line resonances observed with the Super Dual Auroral Radar Network. *Journal of Geophysical Research*, 100:21,535, 1995.

[10] P. Frycz, R. Rankin, J.C. Samson, and V.T. Tikhonchuk. Nonlinear field line resonances: Dispersive effects. *Physics of Plasmas*, 5:3565, 1998.

[11] V. Génot, P. Louarn, and F. Mottez. Electron acceleration by Alfvén waves in density cavities. *Journal of Geophysical Research*, 105:27,611, 2000.

[12] C.K. Goertz. Kinetic Alfvén waves on auroral field lines. *Planetary Space Science*, 32:1387, 1984.

[13] C.K. Goertz and R.W. Boswell. Magnetosphere-ionosphere coupling. *Journal of Geophysical Research*, 84:7239, 1979.

[14] Harvey Gould and Jan Tobochnik. *An Introduction to Computer Simulation Methods: Application to Physical Systems*. Addison-Wesley Publishing Company, 1996.

[15] D.A. Hamlin, R. Karplus, R.C. Vik, and K.M. Watson. Mirror and azimuthal drift frequencies for geomagnetically trapped particles. *Journal of Geophysical Research*, 66:1, 1961.

[16] Akira Hasegawa. Particle acceleration by MHD surface wave and formation of aurora. *Journal of Geophysical Research*, 81:5083, 1976.

[17] C.-H. Hui and C.E. Seyler. Electron acceleration by Alfvén waves in the magnetosphere. *Journal of Geophysical Research*, 97:3953, 1992.

[18] B. Inhester. Numerical modeling of hydrodynamic wave coupling in the magnetosphere. *Journal of Geophysical Research*, 92:4751, 1987.

[19] T. Karlsson and G.T. Marklund. A statistical study of intense low-altitude electric fields observed by Freja. *Geophysical Research Letters*, 23:1005, 1996.

[20] C.A. Kletzing. Electron acceleration by kinetic Alfvén waves. *Journal of Geophysical Research*, 99:11,095, 1994.

[21] David J. Knudsen. Spatial modulation of electron energy and density by nonlinear stationary inertial Alfvén waves. *Journal of Geophysical Research*, 101:10,761, 1996.

[22] W. Lotko, A.V. Streltsov, and C.W. Carlson. Discrete auroral arc, electrostatic shock and suprathermal electrons powered by dispersive, anonamously resistive field line resonance. *Journal of Geophysical Research*, 25:4449, 1998.

[23] Dwight R. Nicholson. *Introduction to Plasma Theory*. John Wiley & Sons, Inc., 1983.

[24] H. Okuda, W.W. Lee, and C.Z. Cheng. Electrostatic and magnetostatic particle simulation models in three dimensions. *Computer Physics Communications*, 17:233, 1979.

[25] George K. Parks. *Physics of Space Plasmas, An Introduction*. Addison-Wesley Publishing Company, Redwood City, 1991.

[26] Henry R. Radoski. A note on oscillating field lines. *Journal of Geophysical Research*, 72:418, 1967.

[27] R. Rankin, B.G. Harrold, J.C. Samson, and P. Frycz. The nonlinear evolution of field line resonances in the Earth's magnetosphere. *Journal of Geophysical Research*, 98:5839, 1993a.

[28] R. Rankin, J.C. Samson, and P. Frycz. Simulations of driven field line resonances in the Earth's magnetosphere. *Journal of Geophysical Research*, 98:21341, 1993b.

[29] R. Rankin, J.C. Samson, and V.T. Tikhonchuk. Parallel electric fields in dispersive shear Alfvén waves in the dipolar magnetosphere. *Geophysical Research Letters*, 26:3601, 1999.

[30] R. Rankin and V.T. Tikhonchuk. Numerical simulations and simplified models of nonlinear electron inertial Alfvén waves. *Journal of Geophysical Research*, 103:20,419, 1998.

[31] Graham J. Rickard and Andrew N. Wright. Alfvén resonance excitation and fast wave propagations in magnetospheric waveguides. *Journal of Geophysical Research*, 99:13,455, 1994.

[32] J.C. Samson, L.L. Cogger, and Q. Pao. Observations of field line resonances, auroral arcs, and auroral vortex structures. *Journal of Geophysical Research*, 101:17373, 1996.

[33] J.C. Samson, B.G. Harrold, J.M. Ruohoniemi, R.A. Greenwald, and A.D.M Walker. Field line resonances associated with MHD waveguides in the magnetosphere. *Geophysical Research Letters*, 19:441, 1992b.

[34] J.C. Samson, T.J. Hughes, F. Creutzberg, D.D. Wallis, R.A. Greenwald, and J.M. Ruohoniemi. Observations of a detached, discrete arc in association with field line resonances. *Journal of Geophysical Research*, 96:15,683, 1991.

[35] J.C. Samson, D.D Wallis, T.J. Hughes, F. Creutzberg, J.M. Ruohoniemi, and R.A. Greenwald. Substorm intensifications and field line resonances in the nightside magnetosphere. *Journal of Geophysical Research*, 97:8495, 1992a.

[36] D.J. Southwood. Some features of field line resonances in the magnetosphere. *Planetary Space Science*, 22:483, 1974.

[37] A.V. Streltsov and W. Lotko. Dispersive, nonradiative field line resonances in a dipolar magnetic field geometry. *Journal of Geophysical Research*, 102:27,121, 1997.

[38] A.V. Streltsov and W. Lotko. Small-scale, "electrostatic" auroral structures and Alfvén waves. *Journal of Geophysical Research*, 104:4411, 1999.

[39] B.J. Thompson and R.L. Lysak. Electron acceleration by inertial Alfvén waves. *Journal of Geophysical Research*, 101:5359, 1996.

[40] V.T. Tikhonchuk and R. Rankin. Electron kinetic effects in standing shear Alfvén waves in the dipolar magnetosphere. *Physics of Plasmas*, 7:2630, 2000.

[41] Igor Voronkov. *Shear Alfvén Waves and Shear Flow Instabilities in the Earth's Magnetosphere*. PhD thesis, University of Alberta, 1998.

[42] A.D.M Walker, J.M Ruohoniemi, K.B. Baker, and R.A. Greenwald. Spatial and temporal behavior of ULF pulsations observed by the goose bay HF radar. *Journal of Geophysical Research*, 97:12187, 1992.

[43] C.Q. Wei, J.C. Samson, R. Rankin, and P. Prycz. Electron inertial effects on geomagnetic field line resonances. *Journal of Geophysical Research*, 99:11,265, 1994.

[44] D. Winske and K.B. Quest. Electromagnetic ion beam instabilities: Comparison of one- and two-dimensional simulations. *Journal of Geophysical Research*, 91:8789, 1986.

[45] Andrew N. Wright. Dispersion and wave coupling in inhomogeneous MHD waveguides. *Journal of Geophysical Research*, 99:159, 1994.

[46] B.-L. Xu, J.C. Samson, W.W. Liu, F. Creutzberg, and T.J. Hughes. Observations of optical aurora modulated by resonant Alfvén waves. *Journal of Geophysical Research*, 98:11531, 1993.

Appendix A

Kinetic Dispersion Relation

Using the cold plasma equations and defining a dependence of $e^{i(k_x x + k_y y + k_z z) - i\omega t}$ it is straight forward to derive a dispersion relation for the periodic system as

$$\omega^2 = k_z^2 V_A^2 (1 + \frac{ik_x^2}{\omega \mu_o \sigma_z})^{-1} \tag{A.1}$$

where it has been assumed that $k_y = 0$ and an Ohms Law $E_z = j_z / \sigma_z$ has been used to relate the the field aligned electric field and current. In order to determine the field aligned conductivity σ_z, we start with the general drift kinetic equation (Baumjohann et al., (1996))

$$\frac{\partial f_d}{\partial t} + \nabla_{\vec{r}_g} \cdot (\vec{v}_d f_d) + \frac{\partial}{\partial v_{\parallel}} (\frac{F_{\parallel}}{m} f_d) = 0 \tag{A.2}$$

where

$$\vec{v}_d = \frac{v_{\parallel} \vec{B}}{B} + \vec{v}_E + \frac{\vec{F} \times \vec{B}}{B^2} \tag{A.3}$$

$$\vec{v}_E = \frac{\vec{E} \times \vec{B}}{B^2} \tag{A.4}$$

$$F_{\parallel} = -\mu \nabla_{\parallel} B + q E_{\parallel} \tag{A.5}$$

$$F_{\perp} = -\mu \nabla_{\perp} B - m v_{\parallel}^2 \frac{\vec{R}_c}{R_c^2} - m \frac{dv_E}{dt} \tag{A.6}$$

$\vec{r}_g$ is the guiding center position, $\vec{v}_d$ is the guiding center velocity and $\vec{F}$ is the force applied to the particles. For electrons, the $\vec{E} \times \vec{B}$ and polarization drifts are negligible. This, along with the lack of curvature simplifies the full drift kinetic equation to

$$\frac{\partial f_d}{\partial t} + \frac{\partial}{\partial z} (v_z f_d) + \frac{\partial}{\partial v_z} (\frac{q E_z}{m_e} f_d) = 0 \tag{A.7}$$

where we have replaced the '$\parallel$' notation with z. Linearizing such that $f_d = f_o + f_1$, where f_o and f_1 are the equilibrium and perturbed distributions respectively and keeping only first order terms, the kinetic dispersion relation becomes

$$\frac{\partial f_1}{\partial t} + v_z \frac{\partial f_1}{\partial z} - \frac{e E_z}{m_e} \frac{\partial f_o}{\partial v_z} = 0 \tag{A.8}$$

where the fact that v_z and z are independent variables has been used as well. This kinetic equation is the same as that used for low frequency phenomena (Tichkonchuk et. al, 2000;

124

Antonsen and Lane, 1980). Assuming the dependence $e^{ik_z z - i\omega t}$, the electron kinetic equation can be solved for the perturbed distribution

$$f_1 = \frac{-ieE_z \frac{\partial f_o}{\partial v_z}}{k_z m (v_z - \frac{\omega}{k_z})}.$$ (A.9)

The current is related to the perturbed distribution via

$$j_z = -e \int d^3 v v_z f_1.$$

Performing the integration using a Maxwellian distribution for f_o,

$$f_o = n(\frac{m}{2\pi k_B T})^{1/2} e^{-mv_z^2 / 2k_B T} \delta(v_x) \delta(v_y)$$ (A.10)

yields the following expression relating the field aligned current and electric field

$$j_z = \frac{-ie^2 n\omega}{k_z^2 k_B T}(1 + \epsilon Z(\epsilon)) E_z$$ (A.11)

where $\epsilon = \frac{\omega}{k_z}\sqrt{\frac{m}{2k_B T}}$ and Z is the plasma dispersion function defined by

$$Z(\epsilon) = \frac{1}{\sqrt{\pi}} \int_{-\infty}^{\infty} \frac{dx e^{-x^2}}{x - \epsilon}.$$ (A.12)

Comparing (A.11) with the Ohm's law $J_z = \sigma_z E_z$, the corresponding expression for the field aligned conductivity is given by

$$\sigma_z = \frac{-ie^2 n\omega}{k_z^2 k_B T}(1 + \epsilon Z(\epsilon))$$ (A.13)

and substituting this into expression (A.1) the complete kinetic dispersion relation is then

$$\omega^2 = k_z^2 V_A^2 (1 + \frac{ik_x^2}{\omega\mu_o \frac{-ie^2 n\omega}{k_z^2 k_B T}(1 + \epsilon Z(\epsilon))})^{-1}.$$ (A.14)

In the cold plasma case (when $V_A \gg V_{th}$), the plasma dispersion function can be expanded as

$$Z(\epsilon) = -\frac{1}{\epsilon} - \frac{1}{2\epsilon^2} - \frac{1}{4\epsilon^3}.$$ (A.15)

Using this expression (with only the first two terms) in the kinetic dispersion relation allows the simplification of the dispersion relation to that of the familiar inertial SAW

$$\omega^2 = \frac{k_z^2 V_A}{1 + k_x^2 \lambda_e^2}.$$ (A.16)

In the warm plasma limit ($V_A \ll v_{th}$), the asymptotic expansion of the plasma dispersion function is given by

$$Z(\epsilon) = -2\epsilon(1 - \frac{2}{3}\epsilon^2)$$ (A.17)

and the conductivity becomes

$$\sigma_z = \frac{-ie^2 n\omega}{k_z^2 k_B T}(1 - 2\epsilon^2 + \frac{4}{3}\epsilon^3).$$ (A.18)

125

Since $\epsilon^2 \ll 1$, the conductivity can be simplified to

$$\sigma_z = \frac{-ie^2 n\omega}{k_z^2 k_B T} \tag{A.19}$$

the dispersion relation becomes

$$\omega^2 = k_z^2 V_A^2 (1 + \frac{1}{2} k_x^2 \rho_s^2) \tag{A.20}$$

where $\rho_s = \frac{\lambda_e v_{th}}{V_A}$. This warm electron dispersion relation generally appears with an additional term due to ion gyroradius effects (see Lysak and Lotko, 1996). The absence of this term emphasizes that for this model to be valid, the minimum scale lengths should be larger than typical ion gyroradii. In addition, the factor of $\frac{1}{2}$ originates from the choice of $v_{th} = \sqrt{\frac{2k_B T}{m_e}}$ rather than $v_{th} = \sqrt{\frac{k_B T}{m_e}}$ which makes this equation appear slightly different than is typically written.

As an aside, it is fairly straightforward to illustrate the derivation of the simplified generalized ohms law. Starting with the simplified drift kinetic equation,

$$(\frac{\partial}{\partial t} + v_z \frac{\partial}{\partial z}) f_1 = \frac{eE_z}{m_e} \frac{\partial f_o}{\partial v_z}$$

and assuming v_z is not a function of t and z, integration over velocity yields

$$\frac{\partial j}{\partial t} - e\frac{\partial}{\partial z} \int_{-\infty}^{\infty} dv_z v_z^2 f_o = \frac{e^2 n_e}{m_e} E_z$$

where $n_e = \int_{-\infty}^{\infty} dv_z f_o$ and $j = -e \int_{-\infty}^{\infty} dv_z v_z f_1$. As there is no bulk fluid flow in the z direction, the electron pressure is given by

$$P_e = m_e \int_{-\infty}^{\infty} dv_z v_z^2 f_1$$

and therefore we have

$$\frac{\partial j}{\partial t} - \frac{e}{m_e} \frac{\partial}{\partial z} P_e = \frac{e^2 n_e}{m_e} E_z.$$

Rearranging and using the definition for electron inertial length $\lambda_e = m_e/(\mu_o n_e e^2)$ yields the familiar generalized ohm's law

$$E_z = \mu_o \lambda_e^2 \frac{\partial j_z}{\partial t} - \frac{1}{n_e e} \frac{\partial P_e}{\partial z}.$$

126